A gradient-enhanced large-deformation continuum damage model for fibre-reinforced materials

Tobias Waffenschmidt , César Polindara , Andreas Menzel , Sergio Blanco

Keywords:
Gradient-enhanced damage
Large deformations
Finite element method
Anisotropic biological tissues
Abaqus UEL
Arc-length method

A B S T R A C T

A non-local gradient-based damage formulation within a geometrically non-linear setting is presented. The hyperelastic constitutive response at local material point level is governed by a strain energy which is additively composed of an isotropic matrix and of an anisotropic fibre-reinforced material, respectively. The inelastic constitutive response is governed by a scalar $[1-d]$-type damage formulation, where only the anisotropic elastic part is assumed to be affected by the damage. Following the concept in Dimitrijević and Hackl [28], the local free energy function is enhanced by a gradient-term. This term essentially contains the gradient of the non-local damage variable which, itself, is introduced as an additional independent variable. In order to guarantee the equivalence between the local and non-local damage variable, a penalisation term is incorporated within the free energy function. Based on the principle of minimum total potential energy, a coupled system of Euler–Lagrange equations, i.e., the balance of linear momentum and the balance of the non-local damage field, is obtained and solved in weak form. The resulting coupled, highly non-linear system of equations is symmetric and can conveniently be solved by a standard incremental-iterative Newton–Raphson-type solution scheme. Several three-dimensional displacement- and force-driven boundary value problems—partially motivated by biomechanical application—highlight the mesh-objective characteristics and constitutive properties of the model and illustratively underline the capabilities of the formulation proposed.

1. Introduction

The understanding and physical description of damage and failure effects in materials presents a major challenge in various engineering-related disciplines. Failure processes in ductile steels, for instance, are characterised by a complex interaction of plastic deformation and damage effects. These phenomena originate from the motion and accumulation of dislocations which interact and result in micro-cracks and micro-voids and finally lead to a necking-like reduction of effective area and possibly to ultimate failure of the material. Damage processes in concrete are typically initiated at the interface between stiff grains and the ambient cement matrix, result in a coalescence and propagation of micro-cracks and finally lead to a global stiffness loss accompanied by localised degradation patterns. To give a particular example with regard to the present contribution, damage processes in anisotropic soft biological tissues are closely related to the progressive failure of fibres embedded in the ambient bulk or matrix material. An exemplary qualitative simulation result based on the constitutive

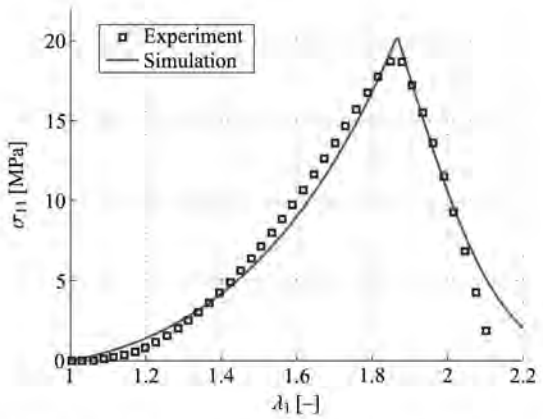

Fig. 1. Qualitative simulation based on the constitutive model proposed in Section 3 and experimental stress-stretch data of a fascia tissue specimen under uniaxial isochoric tension, cf. Martins et al. [58]. Material parameters are chosen as $\mu_e = 0.01$ kPa, $\kappa_e = 499.0$ kPa, $k_1 = 0.55$ kPa, $k_2 = 0.01$, $\kappa_d = 3.5$ kPa, $\eta_d = 0.6$ kPa^{-1}.

model subsequently proposed in this contribution, together with experimental stress-stretch data from Martins et al. [58], is provided in Fig. 1. The results refer to the mechanical response of a fascia tissue specimen under uniaxial isochoric tension. Arteries, for instance, can be considered as a composite of an isotropic ground substance of elastin fibres and a highly anisotropic network of cross-linked collagen fibrils. Mechanical loading beyond the physiological loading range, e.g., caused by a surgical intervention such as balloon angioplasty, can significantly reduce the elastic properties of the artery. Physically related to Mullins-type effects, these phenomena can be attributed to the continuous degradation of particular collagen fibres and to the corresponding overstretch of neighbouring cross-links leading to pronounced softening.

Based on the classical work by Kachanov et al. [43] who interpreted the damage effect as a consequence of an area reduction of the stress-bearing region, material degradation can be modelled by means of standard continuum damage formulations, i.e., in a local sense. Up to now, a large variety of models exist where we refer the reader to classic monographs and textbooks as, e.g., Kachanov [43], Kachanov [44], Krajcinovic and Lemaitre [46], Lemaitre and Chaboche [51], Lemaitre [50] or Krajcinovic [45], to name only a few. However, the assumption of a purely *local* continuum damage may, as a major drawback, imply a loss of well-posedness, such as loss of ellipticity, of the underlying boundary value problem. With regard to related numerical methods such as the finite element method, this results in a significant mesh-dependence of the solutions, in other words in a vanishing localised damage zone upon mesh refinement, and hence physically meaningless—or at least questionable—simulations.

In order to regularise the problem, and thereby to circumvent the aforementioned deficiencies, several approaches have been proposed in the literature as, for instance, viscous regularisation, or the concept of generalised *non-local* continua such as micromorphic continua, see the monograph on non-local continuum field theories by Eringen et al. [31], the articles by Aifantis et al. [7,8] or the contributions in Eringen [30] and Rogula [81]. Here, intrinsic or rather internal length scales are introduced into the continuum formulation. A non-local continuum formulation can generally be established by either introducing an integral- or a gradient-type equation.

Non-local *integral* models are inherently associated with a global averaging procedure which complicates the linearisation of the equations and from the computational point of view, are far more expensive than related gradient-type models. With regard to continuum damage formulations, non-local integral models are advocated by Pijaudier-Cabot and Bažant [73] and Bažant [16] and extensively studied by Jirásek [42] or Bažant and Ožbolt [18] and Bažant and Di Luzio [17], the latter referring to microplane models.

As a convenient alternative, Lasry and Belytschko [49], Mühlhaus and Aifantis [64], Polizzotto et al. [74] suggested non-local *gradient* models. Here, the non-locality is incorporated by means of an additional gradient-based Euler–Lagrange equation, to be fulfilled in a weak sense, accompanied by a non-local quantity taking the interpretation of an additional independent variable. Non-local gradient-based continuum damage formulations were first discussed in de Vree et al. [94], Peerlings et al. [71] and de Borst and Pamin [21]; see also the comparison by Pamin [69] or the coupled damage-plasticity approach by Svedberg and Runesson [91].

A large variety of gradient-extended damage formulations exists for the geometrical *linear* case, see e.g., the contributions by Kuhl and Ramm [47] and Kuhl et al. [48] for anisotropic gradient damage or the article by Liebe et al. [55] for isotropic gradient damage. However, there is a comparatively small number of contributions for the geometrical *non-linear* case. The article by Steinmann [90] can be considered as a starting point wherein the non-local strain energy density is introduced as an additional primary variable. This approach was used in Liebe and Steinmann [54], and similarly with application to softening-plasticity in Liebe et al. [53], and compared to an alternative model which takes the damage field as an independent variable. Both approaches used a global active-set-search to account for the Kuhn–Tucker conditions. Recently, Wcisło et al. [97] proposed a gradient-enhanced large-strain damage-plasticity model where gradient averaging is applied to the deformation measure which determines the damage evolution. Following the concept by Frémond and Nedjar [33], the article by Nedjar [68] considered a damage-related formalism based on the principle of virtual power where the power of the internal

forces depends, in addition to the strain rates, on the damage rate itself as well as on the gradient of the damage rate. The series of papers by Abu Al-Rub and Voyiadjis [6] and Voyiadjis and Abu Al-Rub [93], proposed a non-local gradient-enhanced plastic-damage model coupled to visco-inelasticity where 'explicit and implicit microstructural length scales' are introduced by means of viscosity and gradient localisation limiters.

As mentioned above, damage processes in biomaterials such as arteries are of major significance with regard to surgical treatments. In recent years, the mechanics of damage and failure in soft biological tissue has extensively been studied from the experimental and modelling point of view. A multitude of damage and failure formulations has been published, such as the article by Calvo et al. [22], the contribution by Volokh [92], or the recent publication by Balzani et al. [13], amongst others. However, to the authors' knowledge, almost all of these works consider damage as a purely local phenomenon without robust regularisation techniques involved, which, in view of finite element applications, may result in highly mesh-dependent and physically questionable simulations. A visco-type regularisation-approach is adopted in, e.g., Peña et al. [72]. So far, a fully non-local gradient-extended damage formulation allowing for large deformations with special regard to biological tissues has not yet been established for anisotropic biological tissues.

In this contribution, we apply a non-local gradient-based damage formulation within a geometrically non-linear setting. Following the concept in Dimitrijević and Hackl [28], we enhance the local free energy function by a gradient-term. This term essentially contains the referential gradient of the non-local damage variable which itself is introduced as an additional independent variable. In order to guarantee the equivalence between the local and non-local damage variable, a penalisation term is incorporated within the free energy function. Basically, this approach is in line with the systematic construction of micromorphic gradient-type dissipative solids proposed by Forest [32], and can be considered as a special application case of the multi-field incremental variational framework for gradient-extended dissipative solids discussed by Miehe [67].

This work presents a geometrically *non-linear* framework allowing for large deformations. Based on the principle of minimum total potential energy, a coupled system of Euler–Lagrange equations, i.e., the balance of linear momentum and the balance corresponding to the non-local damage field contributions, is obtained which will be solved in weak form. As a key aspect of the model proposed in this contribution, the hyperelastic constitutive response at local material point level is governed by a highly non-linear strain energy, additively composed of an isotropic contribution of the matrix material and of an anisotropic contribution related to the fibre-reinforcement. The inelastic constitutive response is governed by a scalar [1–d]-type damage formulation, where only the anisotropic elastic part is assumed to be affected by the damage evolution. The resulting coupled, highly non-linear system of equations is symmetric and can conveniently be solved by a standard incremental-iterative Newton–Raphson-type solution scheme. Essential numerical aspects of the algorithmic setting of the (non-)local inelastic constitutive relations and the coupled finite element approach are presented in detail. Furthermore, an outline on the computer-implementation is provided with a focus on the commercial finite-element-software Abaqus. Several three-dimensional displacement and force-driven boundary value problems, solved with the finite element method, highlight the mesh-objective characteristics and constitutive properties of the model and illustratively underline the capabilities of the formulation proposed.

The theoretical outline as discussed in Sections 2 and 3 constitutes a combination of the small-strain-based gradient enhanced continuum damage formulation proposed by Dimitrijević and Hackl [28] on the one hand, and the local scalar [1–d]-damage formulation used, for instance, in Liebe et al. [55] on the other. The difference in the *local* damage formulations used in these articles relies on the usage of the damage *variable*. Dimitrijević and Hackl [28] introduced an internal variable $d \in (0, \infty)$, which in Liebe et al. [55] is denoted as κ. Liebe et al. [55] derived the driving force according to the damage variable $d \in [0, 1)$ as $Y = -\partial_d \Psi$. Dimitrijević and Hackl [28] introduced the driving force according to the internal variable as $q = -\partial_d \Psi$ but $d \in (0, \infty)$. These two formulations consequently do *not* coincide even if they seem to be identical at first glance. As a further conceptual difference, Dimitrijević and Hackl [28] introduced the damage *condition* as $\phi - r_1 \leqslant 0$ with $r_1 = \text{const}$ whereas Liebe et al. [55] used $\phi - \kappa \leqslant 0$. As a notable consequence, the (local) damage formulation used by Dimitrijević and Hackl [28] may not work appropriately in connection with the exponential constitutive relation used later on in the present work. This is caused by the effect that the exponential contribution due to the fibre-related anisotropic part of the free energy 'over-compensates' the damage contribution, resulting in an increase of the local stress vs. stretch response at a formally almost fully degraded material state. We therefore adopt the classic scalar [1–d]-damage formulation in the following. For the general case of *anisotropic* damage, tensorial variables would also have to be taken into account; see, e.g., Menzel and Steinmann [61] and Menzel et al. [59] for local anisotropic damage approaches at large strains or the contributions by Kuhl and Ramm [47,48] with regard to gradient-enhanced anisotropic damage models at small strains.

The present approach offers several advantages over other gradient-enhanced damage formulations proposed in the literature. As a major benefit, due to its conceptual simplicity, the present formulation can be solved by standard Newton–Raphson-type solution procedures without any need for advanced and computationally expensive solution methods such as a global active-set-search as applied by Liebe et al. [55]. The present gradient-enhanced damage approach proves to be robust, even at high levels of degradation, and allows the straightforward incorporation of practically any suitable scalar-valued damage formulation, ensuring the damage function to decrease faster with deformation than the respective (undamaged) stress measure would increase with deformation.

This paper is organised as follows: In Section 2, we briefly summarise relevant kinematic relations for the geometrically non-linear case and establish generic balance equations of the coupled boundary value problem in weak and strong form on the basis of the principle of minimum total potential energy. Next, in Section 3, we specify the underlying constitutive equations, containing the isotropic and anisotropic non-linear elastic and gradient-enhanced free energies, as well as the continuum damage formulation in its continuous format and corresponding algorithmic setting. In Section 4, we discretise the

governing weak forms by means of the finite-element method resulting in a coupled non-linear system of equations which can be solved appropriately with incremental-iterative Newton–Raphson-type solution procedures. Last, in Section 5, we apply the proposed model to representative three-dimensional homogeneous and inhomogeneous deformation problems. In order to illustrate the basic constitutive characteristic of the formulation, we first investigate a homogeneous model problem under uniaxial tension. Secondly, to emphasise the regularisation properties of the model due to the gradient-enhancement strategy, we consider a displacement-driven anisotropic plate with a hole. Thirdly, to show the capabilities of the approach with regard to biomechanics-related problems, we study a force-driven example by means of an anisotropic artery-like tube subjected to internal pressure. We conclude with a summary, future perspectives and final remarks in Section 6.

2. Gradient enhancement of a continuum damage formulation

This section summarises essential kinematic relations and derives the governing coupled balance equations of the boundary value problem on the basis of the principle of minimum total potential energy. Especially the corresponding variational and strong forms are elaborated both in referential and spatial description, where the latter provides the basis for the finite-element discretisation described in Section 4.

2.1. Basic kinematics

Let $\boldsymbol{x} = \boldsymbol{\varphi}(\boldsymbol{X}, t)$ describe the deformation of the body, which transforms referential placements $\boldsymbol{X} \in \mathcal{B}_0$ to their spatial counterparts $\boldsymbol{x} \in \mathcal{B}_t$. Based on this, the deformation gradient is defined as

$$\boldsymbol{F} = \nabla_{\boldsymbol{X}} \boldsymbol{\varphi} \tag{1}$$

which transforms infinitesimal referential line elements $\mathrm{d}\boldsymbol{X}$ onto their spatial counterparts $\mathrm{d}\boldsymbol{x}$. Furthermore, let $\mathrm{d}V$ and $\mathrm{d}v$ denote an infinitesimal volume element in referential and spatial setting. Accordingly, the Jacobian

$$J = \frac{\mathrm{d}v}{\mathrm{d}V} = \det(\boldsymbol{F}) > 0 \tag{2}$$

is the ratio of the deformed to the undeformed volume. Finally, let $\mathrm{d}\boldsymbol{A} = \boldsymbol{N}\,\mathrm{d}A$ and $\mathrm{d}\boldsymbol{a} = \boldsymbol{n}\,\mathrm{d}a$ define the reference and spatial area normals. Then, Nanson's formula

$$\boldsymbol{n}\,\mathrm{d}a = \mathrm{cof}(\boldsymbol{F}) \cdot \boldsymbol{N}\,\mathrm{d}A \tag{3}$$

describes the transformation of infinitesimal area elements between the reference and the spatial configuration with the cofactor of $\boldsymbol{F}$ defined as $\mathrm{cof}(\boldsymbol{F}) = J\boldsymbol{F}^{-\mathrm{t}}$. Furthermore, the right and left Cauchy-Green deformation tensors

$$\boldsymbol{C} = \boldsymbol{F}^{\mathrm{t}} \cdot \boldsymbol{F} \quad \text{and} \quad \boldsymbol{b} = \boldsymbol{F} \cdot \boldsymbol{F}^{\mathrm{t}} \tag{4}$$

are introduced.

Fibre-reinforcement of the material is considered by assuming two families of fibres to be embedded in the continuum. Their orientation is characterised by referential unit vectors $\boldsymbol{a}_{0i}$, $i = 1, 2$ with $\|\boldsymbol{a}_{0i}\| = 1$. The deformation $\boldsymbol{\varphi}(\boldsymbol{X}, t)$ locally transforms the fibre into its current configuration, where the vector $\boldsymbol{a}_i = \boldsymbol{F} \cdot \boldsymbol{a}_{0i}$ defines the spatial orientation with $\|\boldsymbol{a}_i\| > 0$ denoting the stretch in the direction of the particular fibre.

2.2. General gradient-enhanced format of the free energy function

As a starting point, we assume the existence of a local free energy function Ψ^{loc} defined per unit reference volume

$$\Psi^{\mathrm{loc}}(\boldsymbol{F}, \boldsymbol{A}_i, \kappa) = \Psi^{\mathrm{iso}}(\boldsymbol{F}) + f_{\mathrm{d}}(\kappa)\, \Psi^{\mathrm{ani}}(\boldsymbol{F}, \boldsymbol{A}_i) \tag{5}$$

that accounts for anisotropic non-linear elastic material response under the influence of scalar damage. Basically, the effective free energy function of the hypothetical undamaged material is composed additively of an isotropic contribution Ψ^{iso}, representing the ground substance, i.e., the matrix material, and an anisotropic contribution Ψ^{ani} associated with the embedded fibres. It is assumed that only the anisotropic part is subjected to damage, whereas the isotropic matrix material remains elastic. In Eq. (5), $\kappa \in [0, \infty)$ is a scalar internal damage variable, characterising a material stiffness loss of the fibres, while $f_{\mathrm{d}}(\kappa) = 1 - d$ represents an appropriate damage function that is at least twice differentiable and satisfies

$$f_{\mathrm{d}}(\kappa) : \mathbb{R}^{+} \to (0, 1] \mid \left\{ f_{\mathrm{d}}(0) = 1,\ \lim_{\kappa \to \infty} f_{\mathrm{d}}(\kappa) \to 0 \right\}. \tag{6}$$

These conditions assure purely elastic behaviour of the undamaged material and complete loss of the related material stiffness in the limiting case $\kappa \to \infty$.

Furthermore, a set of symmetric second-order tensors

$$\boldsymbol{A}_i = \boldsymbol{a}_{0i} \otimes \boldsymbol{a}_{0i}, \quad i = 1, 2 \tag{7}$$

is introduced in Ψ^{ani} to describe the anisotropic and hyperelastic stress response of the fibre-reinforced material.

Following the approach by Dimitrijević and Hackl [28], who considered an analogous framework for the geometrically linear case, a gradient-enhanced non-local free energy function Ψ^{nloc} is introduced as

$$\Psi^{\text{nloc}}(\phi, \nabla_{\boldsymbol{X}}\phi, \kappa; \boldsymbol{F}) = \Psi^{\text{nloc}}_{\text{grd}}(\nabla_{\boldsymbol{X}}\phi; \boldsymbol{F}) + \Psi^{\text{nloc}}_{\text{plty}}(\phi, \kappa), \tag{8}$$

where $\Psi^{\text{nloc}}_{\text{grd}}$ contains the referential gradient of the non-local damage field variable ϕ essentially representing the first-order term of a Taylor series expansion of ϕ at a material point. Moreover, the contribution $\Psi^{\text{nloc}}_{\text{plty}}$ incorporates a penalisation term which links the non-local damage variable ϕ to the local damage variable κ. Consequently, we obtain an enhanced free energy function as

$$\begin{aligned}\Psi_{\text{int}}(\boldsymbol{F}, \phi, \nabla_{\boldsymbol{X}}\phi, \boldsymbol{A}_i, \kappa) &= \Psi^{\text{loc}}(\boldsymbol{F}, \boldsymbol{A}_i, \kappa) + \Psi^{\text{nloc}}(\phi, \nabla_{\boldsymbol{X}}\phi, \kappa; \boldsymbol{F}) \\ &= \Psi^{\text{iso}}(\boldsymbol{F}) + f_{\text{d}}(\kappa)\, \Psi^{\text{ani}}(\boldsymbol{F}, \boldsymbol{A}_i) + \Psi^{\text{nloc}}_{\text{grd}}(\nabla_{\boldsymbol{X}}\phi; \boldsymbol{F}) + \Psi^{\text{nloc}}_{\text{plty}}(\phi, \kappa).\end{aligned} \tag{9}$$

Provided that the external load can be derived from a potential, the local external energy function can be specified as $\Psi_{\text{ext}}(\boldsymbol{\varphi})$.

In summary, the total potential energy function is additively composed of the internal and external contribution so that its local form reads

$$\Psi(\boldsymbol{\varphi}, \boldsymbol{F}, \phi, \nabla_{\boldsymbol{X}}\phi, \boldsymbol{A}_i, \kappa) = \Psi_{\text{int}}(\boldsymbol{F}, \phi, \nabla_{\boldsymbol{X}}\phi, \boldsymbol{A}_i, \kappa) + \Psi_{\text{ext}}(\boldsymbol{\varphi}). \tag{10}$$

2.3. Total potential energy

The total potential energy of a system additively combines the internal contribution Π_{int}, reflecting the action of internal forces, and an external contribution $\Pi_{\text{ext}} = \Pi^{\text{vol}}_{\text{ext}} + \Pi^{\text{sur}}_{\text{ext}}$ due to volume and surface forces, i.e.,

$$\Pi(\boldsymbol{\varphi}, \boldsymbol{F}, \phi, \nabla_{\boldsymbol{X}}\phi; \boldsymbol{A}_i, \kappa) = \Pi_{\text{int}} + \Pi_{\text{ext}}. \tag{11}$$

The existence of the strain energy function (9) provided, the internal energy contribution can be written as

$$\Pi_{\text{int}}(\boldsymbol{F}, \phi, \nabla_{\boldsymbol{X}}\phi; \boldsymbol{A}_i, \kappa) = \int_{\mathcal{B}_0} \Psi_{\text{int}}\, \mathrm{d}V. \tag{12}$$

Assuming 'dead' loads, the external contributions take the representation

$$\Pi^{\text{vol}}_{\text{ext}}(\boldsymbol{\varphi}) = \int_{\mathcal{B}_0} \Psi^{\text{vol}}_{\text{ext}}\, \mathrm{d}V = -\int_{\mathcal{B}_0} \bar{\boldsymbol{B}} \cdot \boldsymbol{\varphi}\, \mathrm{d}V, \tag{13}$$

$$\Pi^{\text{sur}}_{\text{ext}}(\boldsymbol{\varphi}) = \int_{\partial\mathcal{B}_0} \Psi^{\text{sur}}_{\text{ext}}\, \mathrm{d}A = -\int_{\partial\mathcal{B}_0} \bar{\boldsymbol{T}} \cdot \boldsymbol{\varphi}\, \mathrm{d}A, \tag{14}$$

where $\bar{\boldsymbol{B}}$ denotes the body force vector per unit reference volume and $\bar{\boldsymbol{T}}$ characterises the traction vector per unit reference surface area.

2.4. Variational form

The boundary problem is governed by the principle of minimum potential energy

$$\min_{\boldsymbol{\varphi}, \phi} \Pi(\boldsymbol{\varphi}, \boldsymbol{F}, \phi, \nabla_{\boldsymbol{X}}\phi; \boldsymbol{A}_i, \kappa), \tag{15}$$

which is specified by requiring the first variation of the total potential energy with respect to $\boldsymbol{\varphi}$ and ϕ to vanish identically, i.e.,

$$\delta_{\boldsymbol{\varphi}}\Pi(\boldsymbol{\varphi}, \boldsymbol{F}, \phi, \nabla_{\boldsymbol{X}}\phi; \boldsymbol{A}_i, \kappa) \doteq \boldsymbol{0} \quad \forall\ \delta\boldsymbol{\varphi}, \tag{16}$$

$$\delta_{\phi}\Pi(\boldsymbol{\varphi}, \boldsymbol{F}, \phi, \nabla_{\boldsymbol{X}}\phi; \boldsymbol{A}_i, \kappa) \doteq 0 \quad \forall\ \delta\phi. \tag{17}$$

In detail, the resulting coupled system of equations in *material* description can be deduced as

$$\int_{\mathcal{B}_0} \boldsymbol{P} : \nabla_{\boldsymbol{X}}\delta\boldsymbol{\varphi}\, \mathrm{d}V - \int_{\mathcal{B}_0} \bar{\boldsymbol{B}} \cdot \delta\boldsymbol{\varphi}\, \mathrm{d}V - \int_{\partial\mathcal{B}_0} \bar{\boldsymbol{T}} \cdot \delta\boldsymbol{\varphi}\, \mathrm{d}A \doteq 0, \tag{18}$$

$$\int_{\mathcal{B}_0} \boldsymbol{Y} \cdot \nabla_{\boldsymbol{X}}\delta\phi\, \mathrm{d}V - \int_{\mathcal{B}_0} Y\, \delta\phi\, \mathrm{d}V \doteq 0, \tag{19}$$

where the Piola stress $\boldsymbol{P}$ and the vectorial damage quantity $\boldsymbol{Y}$ are related to *flux* terms, whereas the body force $\bar{\boldsymbol{B}}$ and the scalar damage quantity Y are associated to *source* terms. They are defined as

$$\boldsymbol{P} = \partial_{\boldsymbol{F}} \Psi, \quad \bar{\boldsymbol{B}} = -\partial_{\boldsymbol{\varphi}} \Psi^{\text{vol}}_{\text{ext}}, \tag{20}$$

$$\boldsymbol{Y} = \partial_{\nabla_{\boldsymbol{X}} \phi} \Psi, \; Y = -\partial_{\phi} \Psi, \tag{21}$$

together with $\bar{\boldsymbol{T}} = -\partial_{\boldsymbol{\varphi}} \Psi^{\text{sur}}_{\text{ext}}$. The corresponding spatial quantities are given by

$$\boldsymbol{\sigma} = \boldsymbol{P} \cdot \text{cof}(\boldsymbol{F}^{-1}), \quad \bar{\boldsymbol{b}} = J^{-1} \bar{\boldsymbol{B}}, \tag{22}$$

$$\boldsymbol{y} = \boldsymbol{Y} \cdot \text{cof}(\boldsymbol{F}^{-1}), \quad y = J^{-1} Y. \tag{23}$$

Applying relation $\nabla_{\boldsymbol{X}} \delta\boldsymbol{\varphi} = \nabla_{\boldsymbol{x}} \delta\boldsymbol{\varphi} \cdot \boldsymbol{F}$ as well as $\nabla_{\boldsymbol{X}} \delta\phi = \nabla_{\boldsymbol{x}} \delta\phi \cdot \boldsymbol{F}$ together with Eqs. (2) and (3) results in the variational forms in *spatial* description,

$$\int_{\mathcal{B}_t} \boldsymbol{\sigma} : \nabla_{\boldsymbol{x}} \delta\boldsymbol{\varphi} \, \mathrm{d}v - \int_{\mathcal{B}_t} \bar{\boldsymbol{b}} \cdot \delta\boldsymbol{\varphi} \, \mathrm{d}v - \int_{\partial\mathcal{B}_t} \bar{\boldsymbol{t}} \cdot \delta\boldsymbol{\varphi} \, \mathrm{d}a \doteq 0, \tag{24}$$

$$\int_{\mathcal{B}_t} \boldsymbol{y} \cdot \nabla_{\boldsymbol{x}} \delta\phi \, \mathrm{d}v - \int_{\mathcal{B}_t} y \, \delta\phi \, \mathrm{d}v \doteq 0. \tag{25}$$

The first terms in Eqs. (18) and (24) represent the internal virtual work $\delta_{\boldsymbol{\varphi}} W_{\text{int}} = \delta_{\boldsymbol{\varphi}} \Pi_{\text{int}}$, while the remaining terms characterise the external virtual work $\delta_{\boldsymbol{\varphi}} W_{\text{ext}} = -\delta_{\boldsymbol{\varphi}} \Pi_{\text{ext}}$. Consequently, Eqs. (18), (24) and (19), (25) can be expressed in compact form as

$$\delta_{\boldsymbol{\varphi}} W = \delta_{\boldsymbol{\varphi}} W_{\text{int}} - \delta_{\boldsymbol{\varphi}} W_{\text{ext}} = \boldsymbol{0} \quad \forall \; \delta\boldsymbol{\varphi}, \tag{26}$$

$$\delta_{\phi} W = \delta_{\phi} W_{\text{int}} - \delta_{\phi} W_{\text{ext}} = 0 \quad \forall \; \delta\phi, \tag{27}$$

where the internal and external contributions are given in spatial form as

$$\delta_{\boldsymbol{\varphi}} W_{\text{int}} = \int_{\mathcal{B}_t} \boldsymbol{\sigma} : \nabla_{\boldsymbol{x}} \delta\boldsymbol{\varphi} \, \mathrm{d}v, \tag{28}$$

$$\delta_{\boldsymbol{\varphi}} W_{\text{ext}} = \int_{\mathcal{B}_t} \bar{\boldsymbol{b}} \cdot \delta\boldsymbol{\varphi} \, \mathrm{d}v + \int_{\partial\mathcal{B}_t} \bar{\boldsymbol{t}} \cdot \delta\boldsymbol{\varphi} \, \mathrm{d}a, \tag{29}$$

$$\delta_{\phi} W_{\text{int}} = \int_{\mathcal{B}_t} \boldsymbol{y} \cdot \nabla_{\boldsymbol{x}} \delta\phi \, \mathrm{d}v, \tag{30}$$

$$\delta_{\phi} W_{\text{ext}} = \int_{\mathcal{B}_t} y \, \delta\phi \, \mathrm{d}v, \tag{31}$$

These relations provide the basis for the finite-element discretisation described in Section 4.

2.5. Strong form — Euler-Lagrange equations

For the sake of completeness, the corresponding local Euler–Lagrange equations in material and spatial description are derived in this subsection. By means of the well-established relations

$$\boldsymbol{P} : \nabla_{\boldsymbol{X}} \delta\boldsymbol{\varphi} = \nabla_{\boldsymbol{X}} \cdot [\delta\boldsymbol{\varphi} \cdot \boldsymbol{P}] - \delta\boldsymbol{\varphi} \cdot [\nabla_{\boldsymbol{X}} \cdot \boldsymbol{P}], \tag{32}$$

$$\boldsymbol{Y} \cdot \nabla_{\boldsymbol{X}} \delta\phi = \nabla_{\boldsymbol{X}} \cdot [\delta\phi \boldsymbol{Y}] - \delta\phi \nabla_{\boldsymbol{X}} \cdot \boldsymbol{Y}, \tag{33}$$

and Gauss's divergence theorem applied to (18) and (19), we obtain the Euler–Lagrange equations in referential form as

$$\nabla_{\boldsymbol{X}} \cdot \boldsymbol{P} + \bar{\boldsymbol{B}} = \boldsymbol{0} \quad \text{in } \mathcal{B}_0, \tag{34}$$

$$\boldsymbol{P} \cdot \boldsymbol{N} = \bar{\boldsymbol{T}} \quad \text{on } \partial\mathcal{B}_0, \tag{35}$$

and

$$\nabla_{\boldsymbol{X}} \cdot \boldsymbol{Y} + Y = 0 \quad \text{in } \mathcal{B}_0, \tag{36}$$

$$\boldsymbol{Y} \cdot \boldsymbol{N} = 0 \quad \text{on } \partial\mathcal{B}_0. \tag{37}$$

Eqs. (34), (35) represent the common quasi-static balance of linear momentum in local form with respect to the reference configuration $\mathcal{B}_0$. Eqs. (36), (37) represent the governing local balance relations associated with the non-local damage field ϕ with respect to the reference configuration $\mathcal{B}_0$. In this regard, it is important to note that—as implied in Eq. (37)—a *natural boundary condition of vanishing flux of the non-local damage variable* across the boundary $\partial\mathcal{B}_0$ is assumed, as applied for instance by de Borst and Pamin [21], Peerlings et al. [70], Simone et al. [88] amongst others.

Using analogous arguments, the Euler–Lagrange equations in spatial description can be provided. Using the relations

$$\boldsymbol{\sigma} : \nabla_{\boldsymbol{x}} \delta\boldsymbol{\varphi} = \nabla_{\boldsymbol{x}} \cdot [\delta\boldsymbol{\varphi} \cdot \boldsymbol{\sigma}] - \delta\boldsymbol{\varphi} \cdot [\nabla_{\boldsymbol{x}} \cdot \boldsymbol{\sigma}], \tag{38}$$

$$\boldsymbol{y} \cdot \nabla_{\boldsymbol{x}} \delta\phi = \nabla_{\boldsymbol{x}} \cdot [\delta\phi \boldsymbol{y}] - \delta\phi \nabla_{\boldsymbol{x}} \cdot \boldsymbol{y}, \tag{39}$$

and Gauss's divergence theorem applied to (24) and (25), gives the Euler–Lagrange equations in spatial form as

$$\nabla_{\boldsymbol{x}} \cdot \boldsymbol{\sigma} + \bar{\boldsymbol{b}} = \boldsymbol{0} \quad \text{in } \mathcal{B}_t, \tag{40}$$

$$\boldsymbol{\sigma} \cdot \boldsymbol{n} = \bar{\boldsymbol{t}} \quad \text{on } \partial\mathcal{B}_t, \tag{41}$$

and

$$\nabla_{\boldsymbol{x}} \cdot \boldsymbol{y} + y = 0 \quad \text{in } \mathcal{B}_t, \tag{42}$$

$$\boldsymbol{y} \cdot \boldsymbol{n} = 0 \quad \text{on } \partial\mathcal{B}_t. \tag{43}$$

3. Constitutive relations

In this section, we first briefly review the hyperelastic constitutive equations adopted on the basis of an isotropic compressible neo-Hookean relation and an anisotropic contribution, cf. [35]. These relations essentially characterise the *elastic* anisotropic response of the fibre-reinforced materials considered. As a key aspect of this section, the gradient-enhanced, non-local contribution to the free energy function is specified, followed by the formulation of continuum damage and its related algorithmic implementation.

3.1. Hyperelastic part of the free energy function

From Section 2.2, we recall the local free energy density Ψ^{loc}, Eq. (5), to be additively composed of an isotropic part Ψ^{iso}, representing the contribution of an isotropic matrix material, and of an anisotropic part Ψ^{ani}, representing the contributions of the individual families of fibres. In the following, we assume the isotropic part to be specified by a compressible neo-Hookean format

$$\Psi^{\text{iso}} = \frac{\mu_{\text{e}}}{2} [I_1 - 3] - \mu_{\text{e}} \ln(J) + \frac{\lambda_{\text{e}}}{2} [\ln(J)]^2, \tag{44}$$

with $I_1 = \boldsymbol{C} : \boldsymbol{I} = \boldsymbol{I} : \boldsymbol{b}$ denoting the first principal invariant and the second-order identify tensor $\boldsymbol{I}$. The elastic constants are represented by the Lamé-parameters μ_{e} and $\lambda_{\text{e}} = \kappa_{\text{e}} - 2/3\,\mu_{\text{e}}$ in terms of the shear modulus μ_{e} and the bulk modulus κ_{e}. The corresponding Cauchy stress tensor can be derived by means of the constitutive equation for hyperelastic materials, i.e., Eqs. $(20)_1$ and $(22)_1$, and takes the same additive structure as (5), i.e.,

$$\boldsymbol{\sigma} = \boldsymbol{\sigma}^{\text{iso}} + f_{\text{d}}(\kappa)\, \boldsymbol{\sigma}^{\text{ani}}. \tag{45}$$

For the particular strain energy density (44), the isotropic contribution to the Cauchy stresses can be specified as

$$\boldsymbol{\sigma}^{\text{iso}} = \frac{\mu_{\text{e}}}{J} [\boldsymbol{b} - \boldsymbol{I}] + \frac{\lambda_{\text{e}}}{J} \ln(J) \boldsymbol{I}. \tag{46}$$

The anisotropic contribution of the local free energy (5) is based on a modified version of an orthotropic exponential model with two families of fibres, as originally proposed by Holzapfel et al. [37]. This also includes the effect of fibre dispersion, see [35], the review article by Holzapfel and Ogden [39] or Menzel et al. [60]. The free energy adopted is represented by the exponential format

$$\Psi^{\text{ani}} = \frac{k_1}{2\,k_2} \sum_{i=1}^{N} \left[\exp\left(k_2 \langle E_i \rangle^2 \right) - 1 \right], \tag{47}$$

with the strain-like quantity $E_i = \varkappa I_1 + [1 - 3\varkappa] I_{4i} - 1$ and the invariant $I_{4i} = \boldsymbol{C} : \boldsymbol{A}_i = \boldsymbol{C} : [\boldsymbol{a}_{0i} \otimes \boldsymbol{a}_{0i}]$ for $N = 2$ the number of fibre families. The term $\langle E_i \rangle$, where $\langle \bullet \rangle = [|\bullet| + \bullet]/2$ is the Macaulay bracket, reflects the basic assumption that fibres can support tension only. Consequently, the anisotropic strain energy density Ψ^{ani} only contributes if the fibre-related strain is positive, i.e., $E_i > 0$. Fibre dispersion is introduced by means of the parameter $\varkappa \in [0,\, 1/2]$, where $\varkappa = 0$ corresponds to no dispersion, i.e., transverse isotropy, and where $\varkappa = 1/3$ provides an isotropic distribution, whereas $\varkappa = 1/2$ represents an isotropic distribution in the plane perpendicular to $\boldsymbol{a}_{0i}$. The corresponding anisotropic contribution to the Cauchy stress tensor can, for the particular strain energy density (47), be represented as

$$\boldsymbol{\sigma}^{\text{ani}} = 2\,k_1 \sum_{i=1}^{N} \left[E_i \exp\left(k_2 \langle E_i \rangle^2 \right) \boldsymbol{h}_i \right] \tag{48}$$

Table 1
Structural, elastic and damage-related parameters as used in constitutive equations specified in Sections 3.1, 3.2, 3.3.

Type	Symbol	Description	Unit
Structural	$\boldsymbol{a}_{0i}$	Fibre orientation vector	–
	$\varkappa$	Dispersion parameter	–
Elastic	μ_e	Shear modulus	kPa
	κ_e	Bulk modulus	kPa
	k_1	Elastic constant	kPa
	k_2	Elastic constant	–
Regularisation	c_d	Degree of regularisation	$\text{kPa}^{-1}\,\text{mm}^2$
	β_d	Penalty parameter	kPa^{-1}
	γ_d	(Non-)local switch	–
Damage	η_d	Saturation parameter	kPa^{-1}
	κ_0	Damage threshold	kPa

with the generalised structural tensor $\boldsymbol{h}_i = \varkappa \boldsymbol{b} + [1 - 3\varkappa]\, \boldsymbol{a}_i \otimes \boldsymbol{a}_i$. Table 1 summarises the structural and elastic material quantities included in constitutive equations (44)–(48) together with their units. It is important to note that the fibre orientations may be defined arbitrarily, but the present formulation uses only *one* non-local damage variable so that both fibre families undergo identical degradation. This is physically meaningful if both families of fibers possess one and the same stretch history, otherwise a second non-local damage variable may be included in the formulation.

3.2. Gradient-enhanced part of the free energy function

According to Eq. (8), the non-local part of the free energy function is assumed to be additively composed of a gradient-related contribution $\Psi^{\text{nloc}}_{\text{grd}}$ and of a penalty term $\Psi^{\text{nloc}}_{\text{plty}}$. These free energy terms are specified as

$$\Psi^{\text{nloc}}_{\text{grd}}(\nabla_{\boldsymbol{x}}\phi; \boldsymbol{F}) = \frac{c_d}{2}\, \nabla_{\boldsymbol{x}}\phi \cdot \boldsymbol{C}^{-1} \cdot \nabla_{\boldsymbol{x}}\phi = \frac{c_d}{2}\, \nabla_{\boldsymbol{x}}\phi \cdot \nabla_{\boldsymbol{x}}\phi, \tag{49}$$

$$\Psi^{\text{nloc}}_{\text{plty}}(\phi, \kappa) = \frac{\beta_d}{2}\, [\phi - \gamma_d\, \kappa]^2. \tag{50}$$

The energy-related penalty parameter β_d approximately enforces the local damage field κ and the non-local field ϕ to coincide. Furthermore, the gradient parameter c_d controls the quasi-non-local character of the formulation and characterises the degree of gradient regularisation. Finally, a switch-parameter $\gamma_d \in \{0, 1\}$ is introduced to change between the local and non-local gradient-enhanced model: $\gamma_d = 0$ or $c_d = 0$ results in a local model, while $\gamma_d = 1$ and $c_d > 0$ leads to the regularised gradient-enhanced model. For the particular non-local free energy functions (49) and (50), the scalar and vectorial quantities, y and $\boldsymbol{y}$, can be specified by means of relations (21) and (23) as

$$y = -J^{-1} \beta_d\, [\phi - \gamma_d\, \kappa], \tag{51}$$

$$\boldsymbol{y} = J^{-1} c_d \nabla_{\boldsymbol{x}}\phi. \tag{52}$$

The damage-related parameters included in constitutive equations (49) and (50) together with their units are summarised in Table 1.

Remark 3.1. Based on the general format of the variational form for the non-local damage field variable (25) and using relations (51) and (52), the variational form can be formulated as

$$\int_{\mathcal{B}_t} J^{-1} c_d\, \nabla_{\boldsymbol{x}}\phi \cdot \nabla_{\boldsymbol{x}}\delta\phi\, \mathrm{d}v + \int_{\mathcal{B}_t} J^{-1} \beta_d [\phi - \gamma_d\, \kappa] \delta\phi\, \mathrm{d}v \doteq 0. \tag{53}$$

Using the identity $\nabla_{\boldsymbol{x}}\phi \cdot \nabla_{\boldsymbol{x}}\delta\phi = \nabla_{\boldsymbol{x}} \cdot [\nabla_{\boldsymbol{x}}\phi\, \delta\phi] - \delta\phi\, \Delta_{\boldsymbol{x}}\phi$ with the Laplace operator $\Delta_{\boldsymbol{x}}(\bullet) = \nabla_{\boldsymbol{x}} \cdot [\nabla_{\boldsymbol{x}}(\bullet)]$ and Gauss's divergence theorem, the first integral can be expressed as

$$\int_{\mathcal{B}_t} J^{-1} c_d\, \nabla_{\boldsymbol{x}}\phi \cdot \nabla_{\boldsymbol{x}}\delta\phi\, \mathrm{d}v = \int_{\partial\mathcal{B}_t} J^{-1} c_d\, [\delta\phi\, \nabla_{\boldsymbol{x}}\phi] \cdot \boldsymbol{n}\, \mathrm{d}a - \int_{\mathcal{B}_t} J^{-1} c_d\, \delta\phi\, \Delta_{\boldsymbol{x}}\phi\, \mathrm{d}v. \tag{54}$$

Assuming homogeneous Neumann boundary conditions, i.e., $\nabla_{\boldsymbol{x}}\phi \cdot \boldsymbol{n} = 0$ on $\partial\mathcal{B}_t$, the weak form finally takes the representation

$$\int_{\mathcal{B}_t} J^{-1} c_d\, \Delta_{\boldsymbol{x}}\phi\, \delta\phi\, \mathrm{d}v - \int_{\mathcal{B}_t} J^{-1} \beta_d [\phi - \gamma_d\, \kappa] \delta\phi\, \mathrm{d}v \doteq 0. \tag{55}$$

Based on this, the Euler–Lagrange equation for the non-local damage field variable in spatial format results in

$$c_{\mathrm{d}}\,\Delta_{\boldsymbol{x}}\phi - \beta_{\mathrm{d}}\,[\phi - \gamma_{\mathrm{d}}\,\kappa] = 0 \quad \text{in } \mathcal{B}_t, \tag{56}$$

$$\nabla_{\boldsymbol{x}}\phi \cdot \boldsymbol{n} = 0 \quad \text{on } \partial\mathcal{B}_t. \tag{57}$$

Eq. (56) is a second order differential equation governing the evolution of the non-local damage variable ϕ. An illustrative interpretation of this differential equation is provided by Liebe et al. [55], where the term $\Delta_{\boldsymbol{x}}\phi$ is related to the curvature of the damage profile, i.e., that the driving force increases (decreases) in regions with positive (negative) curvature and consequently 'broadens' the damage profile.

Remark 3.2. Alternative to the gradient-related contribution (49) to the free energy function, one could similarly assume the format

$$\Psi^{\mathrm{nloc}}_{\mathrm{grd}}(\nabla_{\boldsymbol{X}}\phi) = \frac{c_{\mathrm{d}}}{2}\,\nabla_{\boldsymbol{X}}\phi \cdot \nabla_{\boldsymbol{X}}\phi = \frac{c_{\mathrm{d}}}{2}\,\nabla_{\boldsymbol{x}}\phi \cdot \boldsymbol{b} \cdot \nabla_{\boldsymbol{x}}\phi. \tag{58}$$

In this context, the reader is referred to Steinmann [90], who considered the non-local strain energy density as an additional primary variable and who investigated four different options for their specification—basically motivated from material and spatial averaging procedures and combinations thereof. The free energy (49), as used in the course of this contribution, results in stress-like quantities (51) and (52) which in spatial form formally coincide with the expressions for the small strain case, apart from the factor J^{-1}. This simplifies the formulation in terms of spatial arguments as compared to the analogous expression based on Eq. (58). As a finite element formulation in terms of spatial arguments is used, Eq. (49) is applied in the following.

3.3. Gradient-enhanced damage model – continuous formulation

In order to obtain the stress-like thermodynamic forces driving the local dissipative damage process, we follow standard thermodynamic arguments; see, e.g., Lemaitre and Chaboche [51], and Dimitrijević [27]. The total temperature-weighted production of entropy $\dot{\mathcal{S}}$ for an isothermal, irreversible damage process is governed by

$$\dot{\mathcal{S}} = \int_{\mathcal{B}_0} \left[\boldsymbol{P} : \dot{\boldsymbol{F}} - \dot{\Psi} \right] \mathrm{d}V \geqslant 0. \tag{59}$$

Differentiation of the general format of the free energy function (9) with respect to time allows us to specify relation (59) as

$$\dot{\mathcal{S}} = \int_{\mathcal{B}_0} \left[[\boldsymbol{P} - \partial_{\boldsymbol{F}}\Psi] : \dot{\boldsymbol{F}} - \partial_{\kappa}\Psi\,\dot{\kappa} - \partial_{\nabla_{\boldsymbol{X}}\phi}\Psi \cdot \nabla_{\boldsymbol{X}}\dot{\phi} - \partial_{\phi}\Psi\,\dot{\phi} \right] \mathrm{d}V \geqslant 0. \tag{60}$$

Taking into account Eq. (19) together with the definitions (21) and the rate form considered here, the last two terms in (60) depending on $\dot{\phi}$ vanish. The Clausius-Planck inequality can be formulated in local form defining the internal dissipation $\mathcal{D}$ as

$$\mathcal{D} = [\boldsymbol{P} - \partial_{\boldsymbol{F}}\Psi] : \dot{\boldsymbol{F}} - \partial_{\kappa}\Psi\,\dot{\kappa} \geqslant 0. \tag{61}$$

By means of the Coleman-Noll procedure, one recovers the Piola stresses as introduced in Eq. (20) based on variational arguments. The reduced dissipation inequality in local form results in

$$\mathcal{D}_{\mathrm{red}} = g\,\dot{\kappa} \geqslant 0 \tag{62}$$

including the thermodynamic force $g \geqslant 0$ conjugate to the damage variable $\kappa \in [0, \infty)$, i.e.,

$$g = -\partial_{\kappa}\Psi = -\partial_{\kappa}\Psi^{\mathrm{loc}} - \partial_{\kappa}\Psi^{\mathrm{nloc}} = g^{\mathrm{loc}} + g^{\mathrm{nloc}}, \tag{63}$$

which ensures thermodynamic consistency, i.e., $\mathcal{D}_{\mathrm{red}} \geqslant 0$, if g and $\dot{\kappa}$ are non-negative.

As indicated in the introduction, the exponential contribution due to the fibre-related anisotropic part of the free energy may 'over-compensate' the damage contribution and result in an increase of the local stress vs. stretch response even for $\kappa \to \infty$. In order to avoid this undesired effect, we adopt the classic scalar $[1\text{–}d]$-damage formulation in the following and introduce the thermodynamic force $q \geqslant 0$ conjugate to the damage variable $d \in [0, 1)$, i.e.,

$$q = -\partial_{d}\Psi = -\partial_{\kappa}\Psi\,\partial_{d}\kappa = g\,\partial_{d}\kappa. \tag{64}$$

The reduced dissipation inequality is satisfied, i.e., $\mathcal{D}_{\mathrm{red}} \geqslant 0$, if $\partial_{d}\kappa > 0$. In this context, note the relation $f_{\mathrm{d}}(\kappa) = 1 - d$ so that $-\partial_{d}(\bullet) = \partial_{f_{\mathrm{d}}}(\bullet)$. The thermodynamic force q takes the interpretation of the effective strain energy of the fibre contributions released per unit current volume, also called 'energy release rate'. It becomes apparent, that the Cauchy stress tensor $\boldsymbol{\sigma}$ maintains its form associated to a standard local free energy function, whereas the energy release rate q is composed of a local and non-local contribution $q^{\mathrm{loc}} = -\partial_{d}\Psi^{\mathrm{loc}}$ and $q^{\mathrm{nloc}} = -\partial_{d}\Psi^{\mathrm{nloc}} = -\partial_{\kappa}\Psi^{\mathrm{nloc}}\partial_{d}\kappa$, respectively. To be specific, we obtain

$$q^{\mathrm{loc}} = \Psi^{\mathrm{ani}} \;\text{ and }\; q^{\mathrm{nloc}} = \beta_{\mathrm{d}}\,\gamma_{\mathrm{d}}\,[\phi - \gamma_{\mathrm{d}}\,\kappa]\,\partial_{d}\kappa. \tag{65}$$

By means of relation (56), the non-local energy release rate can alternatively be expressed as $q^{\mathrm{nloc}} = \gamma_{\mathrm{d}}\,c_{\mathrm{d}}\,\Delta_{\boldsymbol{x}}\phi\,\partial_{d}\kappa$.

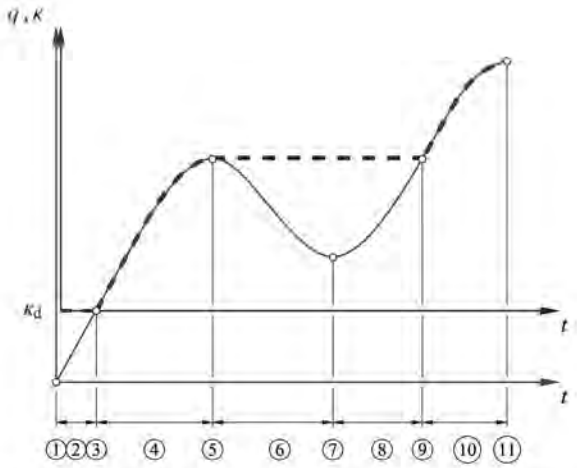

	q	$\dot{q}$	$\dot{\kappa} = \dot{\lambda}$	Remark
①	$< \kappa$	> 0	$= 0$	elastic loading
②	$< \kappa$	> 0	$= 0$	elastic loading
③	$= \kappa$	> 0	$= 0$	elastic loading
④	$= \kappa$	$= \dot{\kappa}$	> 0	damage loading
⑤	$= \kappa$	$= 0$	$= 0$	neutral loading
⑥	$< \kappa$	< 0	$= 0$	elastic unloading
⑦	$< \kappa$	$= 0$	$= 0$	neutral loading
⑧	$< \kappa$	> 0	$= 0$	elastic loading
⑨	$= \kappa$	> 0	$= 0$	elastic loading
⑩	$= \kappa$	$= \dot{\kappa}$	> 0	damage loading
⑪	$= \kappa$	$= \dot{\kappa}$	> 0	damage loading

Fig. 2. Illustration of the Karush–Kuhn–Tucker conditions, i.e., loading–unloading conditions (68) or (69) in combination with the consistency condition $\dot{\lambda}\Phi_{\mathrm{d}} = 0$.

We now adopt a damage condition, at any time of the loading process, as

$$\Phi_{\mathrm{d}} = q - \kappa \leqslant 0 \tag{66}$$

where $\Phi_{\mathrm{d}} < 0$ refers to the purely elastic case and where $\Phi_{\mathrm{d}} = 0$ includes damage evolution. Based on the postulate of maximum dissipation, a constrained optimisation problem involving the Lagrange multiplier $\dot{\lambda}$ can be constructed which results in the following associated representation of the evolution of the damage variable

$$\dot{\kappa} = \dot{\lambda}\,\frac{\partial \Phi_{\mathrm{d}}}{\partial q} = \dot{\lambda} \quad \text{with} \quad \kappa|_{t=0} = \kappa_{\mathrm{d}}. \tag{67}$$

Initiation as well as termination of damage are assumed to be governed by the Karush–Kuhn–Tucker complementary conditions

$$\dot{\lambda} \geqslant 0, \quad \Phi_{\mathrm{d}} \leqslant 0, \quad \dot{\lambda}\,\Phi_{\mathrm{d}} = 0, \tag{68}$$

which, equivalently but more illustratively, can be reformulated as

$$\begin{cases} \Phi_{\mathrm{d}} < 0 & \text{elastic} \\ \Phi_{\mathrm{d}} = 0 \quad \text{and} \quad \begin{cases} \dot{\lambda} < 0 & \text{elastic unloading} \\ \dot{\lambda} = 0 & \text{neutral loading} \\ \dot{\lambda} > 0 & \text{damage loading} \end{cases} \end{cases} \tag{69}$$

see Simo and Hughes [87] and Fig. 2 for a graphical representation.

For the damage function $f_{\mathrm{d}}(\kappa)$, we adopt a simple exponential-type law

$$f_{\mathrm{d}}(\kappa) = 1 - d = \exp(\eta_{\mathrm{d}}\,[\kappa_{\mathrm{d}} - \kappa]), \tag{70}$$

with $\eta_{\mathrm{d}} > 0$ so that $\partial_d \kappa = [\eta_{\mathrm{d}} f_{\mathrm{d}}(\kappa)]^{-1} > 0$. We use an initial damage threshold κ_{d}, which must be exceeded in order to activate damage evolution; in this regard, the initial condition in (67) is of major importance. Furthermore, an exponential saturation parameter η_{d} is included. Note, that for $\kappa_{\mathrm{d}} = 0$ and $\eta_{\mathrm{d}} = 1$, relation (70) reduces to the format $f_{\mathrm{d}}(\kappa) = \exp(-\kappa)$ applied by Dimitrijević and Hackl [28]. The driving force introduced in (64) is, however, different and possesses the property $q^{\mathrm{loc}} = \Psi^{\mathrm{loc}} > 0 \;\forall\, \boldsymbol{F} \neq \boldsymbol{I}$, whereas $g^{\mathrm{loc}} = \eta_{\mathrm{d}} f_{\mathrm{d}}(\kappa)\,\Psi^{\mathrm{loc}} \to 0$ for $\kappa \to \infty$, which turns out to be essential for the energy function Ψ^{loc} chosen later on. Fig. 3 illustrates the characteristics of function (70) for different parameters. It becomes apparent that larger values of η_{d} accelerate the damage process, whereas larger values of κ_{d} lead to a delay of the damage initiation. Note, that for the limiting case $\kappa_{\mathrm{d}} = 0$, damage is initiated from the very beginning of the loading process, whereas no damage evolution is obtained for $\kappa_{\mathrm{d}} \to \infty$.

Remark 3.3. Relation (70) represents a constitutive assumption which is required to be at least twice differentiable and has to satisfy condition (6). In this regard, one could specify alternative formats for the damage function $f_{\mathrm{d}}(\kappa)$ giving more flexibility in calibration and a possibly smoother transition from the undamaged to the damaged state. Two possible damage functions including a maximum damage value d_∞ were suggested by Miehe [66], who introduced

$$f_{\mathrm{d}}^{\circ}(\kappa) = 1 - d_\infty\,[1 - \exp(-\eta_{\mathrm{d}}\,\kappa)], \tag{71}$$

and Leukart and Ramm [52], who adopted an extended format

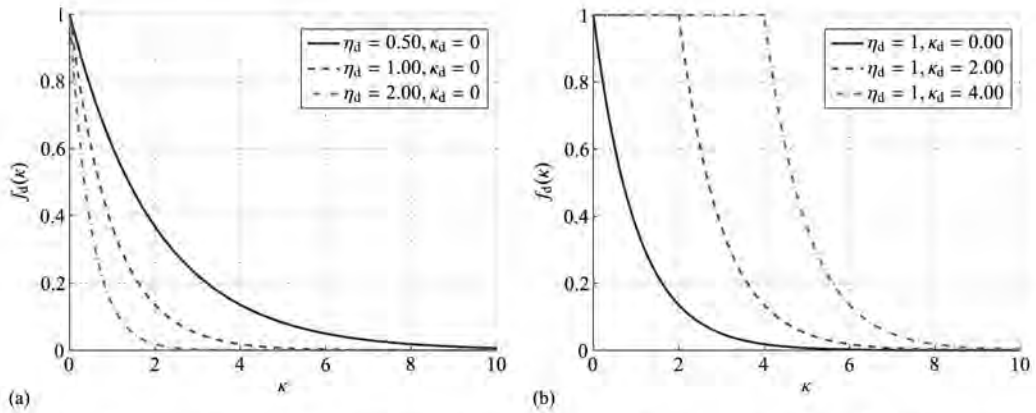

Fig. 3. Exponential damage function $f_d(\kappa)$, see Eq. (70). (a) Different values of the damage saturation parameter η_d. (b) Different values of the damage threshold parameter κ_d where the function $f_d(\kappa) = \exp(-\eta_d\,(\kappa - \kappa_d))$ is plotted for purpose of illustration.

$$f_d^{\star}(\kappa) = \frac{\kappa_d}{\kappa}\,[1 - d_\infty\,[1 - \exp(\eta_d\,[\kappa_d - \kappa])]], \tag{72}$$

incorporating an initial damage threshold κ_d. The format proposed by Sáez et al. [82],

$$f_d^{\Delta}(\kappa) = \frac{1}{1 + \exp(\eta_d[\kappa - \kappa_d])}, \tag{73}$$

however, does not fulfill the basic requirements (6) for all parameter sets $\{\eta_d, \kappa_d\}$, to give an example: $\eta_d = 1, \kappa_d = 1$. Similar observations hold for the tanh-related format

$$f_d^{\bullet}(\kappa) = -\frac{1}{2}[\tanh(\eta_d\,[\kappa - \kappa_d]) - 1]. \tag{74}$$

As an advantage of the gradient-enhanced damage model elaborated in the present work, any damage function satisfying (6) can be adopted.

3.4. Gradient-enhanced damage model — algorithmic setting

Evolution equation (67) represents a non-linear ordinary differential equation, which is integrated numerically in order to obtain the internal damage variable κ at a current time step $n+1$. In this context, we introduce respective intervals in time, $\Delta t = t_{n+1} - t_n \geqslant 0$, and apply an implicit, unconditionally stable Euler backward integration scheme, which yields

$$\kappa_{n+1} = \kappa_n + \gamma_{n+1} \quad \text{with } \kappa|_{t_0} = \kappa_d \tag{75}$$

where $\gamma_{n+1} := \Delta t\,\lambda_{n+1}$ is the incremental Lagrange multiplier at time t_{n+1}. The incremental Karush–Kuhn–Tucker conditions read

$$\gamma_{n+1} \geqslant 0, \quad \Phi_{d\,n+1} \leqslant 0, \quad \gamma_{n+1}\Phi_{d\,n+1} = 0. \tag{76}$$

The stresses are updated according to relations (45) and (51) by

$$\boldsymbol{\sigma}_{n+1} = \boldsymbol{\sigma}_{n+1}^{\text{iso}} + f_d(\kappa_{n+1})\,\boldsymbol{\sigma}_{n+1}^{\text{ani}}; \tag{77}$$

$$y_{n+1} = -J_{n+1}^{-1}\,\beta_d\,[\phi_{n+1} - \gamma_d\,\kappa_{n+1}], \tag{78}$$

with $\kappa_{n+1} = \kappa_n$ for an elastic incremental load step. For an *inelastic* incremental load step, the incremental Lagrange multiplier γ_{n+1} is computed by enforcing the incremental consistency condition such that

$$\Phi_{d\,n+1} = q_{n+1} - \kappa_{n+1} = 0 \tag{79}$$

$$= \Psi_{n+1}^{\text{ani}} + \frac{\beta_d\,\gamma_d}{\eta_d f_d(\kappa_{n+1})}\,[\phi_{n+1} - \gamma_d\,\kappa_{n+1}] - \kappa_{n+1} \tag{80}$$

which depends non-linearly on γ_{n+1}. This non-linear equation can be solved iteratively by employing a Newton–Raphson method. We expand Eq. (79) in a Taylor series at γ_{n+1}^k with k denoting the particular Newton iteration step. Neglecting terms of second and higher order, we obtain

$$\gamma_{n+1}^{k+1} = \gamma_{n+1}^k - \left[\mathrm{d}_\gamma r_{n+1}^k\right]^{-1} r_{n+1}^k \tag{81}$$

where $r_{n+1}^k := \Phi_{d\,n+1}(\kappa_{n+1}^k)$ is the residual in the k-th iteration step. For the particular choice of the damage coefficient function

Table 2
Algorithmic box for the gradient-enhanced damage constitutive model.

0. Given: deformation gradient $\boldsymbol{F}_{n+1}$, non-local damage variable ϕ_{n+1} and gradient $\nabla_{\boldsymbol{x}}\phi_{n+1}$ at time t_{n+1} and internal damage variable κ_n at time t_n
(initialise (non-) local damage field variable as $\kappa|_{t_0} = \phi|_{t_0} = \kappa_{\mathrm{d}}$)

1. Compute isotropic elastic contribution of strain energy $\Psi^{\mathrm{iso}}_{n+1}$, Cauchy stress $\boldsymbol{\sigma}^{\mathrm{iso}}_{n+1}$ and elasticity tensor $\mathbf{e}^{\mathrm{iso}}_{n+1}$

2. Compute anisotropic elastic contribution of strain energy $\Psi^{\mathrm{ani}}_{n+1}$, Cauchy stress $\boldsymbol{\sigma}^{\mathrm{ani}}_{n+1}$ and elasticity tensor $\mathbf{e}^{\mathrm{ani}}_{n+1}$

3. Compute driving force
$q_{n+1} = \Psi^{\mathrm{ani}}_{n+1} + \dfrac{\beta_{\mathrm{d}}\gamma_{\mathrm{d}}}{\eta_{\mathrm{d}} f_{\mathrm{d}}(\kappa_n)}\left[\phi_{n+1} - \gamma_{\mathrm{d}}\kappa_n\right]$
with damage function $f_{\mathrm{d}}(\kappa_n) = \exp(\eta_{\mathrm{d}}[\kappa_{\mathrm{d}} - \kappa_n])$

4. Check damage condition
if $\Phi_{\mathrm{d}\,n+1} = q_{n+1} - \kappa_n \leqslant 0$, set $\kappa_{n+1} = \kappa_n$ and go to 6.
else go to 5.

5. Perform (damped) local Newton–Raphson scheme to compute incremental Lagrange multiplier γ_{n+1} iteratively
(a) compute residual $r^k_{n+1} := \Phi_{\mathrm{d}\,n+1}(\kappa^k_{n+1})$
$r^k_{n+1} = \Psi^{\mathrm{ani}}_{n+1} + \dfrac{\beta_{\mathrm{d}}\gamma_{\mathrm{d}}}{\eta_{\mathrm{d}} f_{\mathrm{d}}(\kappa^k_{n+1})}\left[\phi_{n+1} - \gamma_{\mathrm{d}}\kappa^k_{n+1}\right] - \kappa^k_{n+1}$
(b) check tolerance
if $|r^k_{n+1}| <$ tol go to 6.
else go to 5. (c)
(c) compute tangent of residual
$\mathrm{d}_\gamma r^k_{n+1} = \dfrac{\beta_{\mathrm{d}}\gamma_{\mathrm{d}}}{\eta_{\mathrm{d}} f_{\mathrm{d}}(\kappa^k_{n+1})}\left[\eta_{\mathrm{d}}\left[\phi_{n+1} - \gamma_{\mathrm{d}}\kappa^k_{n+1}\right] - \gamma_{\mathrm{d}}\right] - 1$
(d) compute increment
$\Delta\gamma_{n+1} = -\left[\mathrm{d}_\gamma r^k_{n+1}\right]^{-1} r^k_{n+1}$
(e) update incremental Lagrange multiplier
$\gamma^{k+1}_{n+1} = \gamma^k_{n+1} + \eta\,\Delta\gamma_{n+1}$
with η adjusted iteratively by means of damped Newton scheme (see Table 3)
(f) update internal damage variable
$\kappa^k_{n+1} = \kappa_n + \gamma^{k+1}_{n+1}$
and go to 5. (a)

6. Compute flux and source terms
$\boldsymbol{\sigma}_{n+1} = \boldsymbol{\sigma}^{\mathrm{iso}}_{n+1} + f_{\mathrm{d}}(\kappa_{n+1})\,\boldsymbol{\sigma}^{\mathrm{ani}}_{n+1}$
$\boldsymbol{y}_{n+1} = J^{-1}_{n+1} c_{\mathrm{d}} \nabla_{\boldsymbol{x}}\phi_{n+1}$
$y_{n+1} = -J^{-1}\beta_{\mathrm{d}}\left[\phi_{n+1} - \gamma_{\mathrm{d}}\kappa_{n+1}\right]$

7. Compute tangent moduli, see Appendix A
$\mathbf{e}_{n+1} = \mathbf{e}^{\mathrm{iso}}_{n+1} + f_{\mathrm{d}}\,\mathbf{e}^{\mathrm{ani}}_{n+1} + \eta_{\mathrm{d}} f_{\mathrm{d}}\,\vartheta_{\mathrm{d}} J\,\boldsymbol{\sigma}^{\mathrm{ani}}_{n+1} \otimes \boldsymbol{\sigma}^{\mathrm{ani}}_{n+1}$
$\mathrm{d}\boldsymbol{\sigma}_{n+1}/\mathrm{d}\phi_{n+1} = 2\,\mathrm{d}y_{n+1}/\mathrm{d}\boldsymbol{g}_{n+1} = \beta_{\mathrm{d}}\gamma_{\mathrm{d}}\,\vartheta_{\mathrm{d}}\,\boldsymbol{\sigma}^{\mathrm{ani}}_{n+1}$
$\mathrm{d}y_{n+1}/\mathrm{d}\phi_{n+1} = -J^{-1}\beta_{\mathrm{d}}\left[1 + \beta_{\mathrm{d}}\gamma^2_{\mathrm{d}}\left[\eta_{\mathrm{d}} f_{\mathrm{d}}\right]^{-1}\vartheta_{\mathrm{d}}\right]$
$\mathrm{d}\boldsymbol{y}_{n+1}/\mathrm{d}\nabla_{\boldsymbol{x}}\phi_{n+1} = J^{-1} c_{\mathrm{d}}\,\boldsymbol{I}$
with $\vartheta_{\mathrm{d}} = -1 - \dfrac{\eta_{\mathrm{d}} f_{\mathrm{d}}(\kappa_{n+1})}{\beta_{\mathrm{d}}\gamma_{\mathrm{d}}\left[\gamma_{\mathrm{d}}\left[1 + \eta_{\mathrm{d}}\kappa_{n+1}\right] - \eta_{\mathrm{d}}\phi_{n+1}\right]}$

$$f_{\mathrm{d}}(\kappa_{n+1}) = \exp(\eta_{\mathrm{d}}[\kappa_{\mathrm{d}} - \kappa_{n+1}]), \tag{82}$$

the Jacobian of the Newton–Raphson scheme reads

$$\mathrm{d}_\gamma r^k_{n+1} = \frac{\beta_{\mathrm{d}}\gamma_{\mathrm{d}}}{\eta_{\mathrm{d}} f_{\mathrm{d}}(\kappa_{n+1})}\left[\eta_{\mathrm{d}}\left[\phi_{n+1} - \gamma_{\mathrm{d}}\kappa_{n+1}\right] - \gamma_{\mathrm{d}}\right] - 1. \tag{83}$$

With γ_{n+1} determined, the internal damage variable can be updated iteratively according to (75) while the norm of the residual is larger than a pre-defined tolerance. Finally, the stresses can be calculated according to (77) and (78). The algorithm related to the constitutive model is summarised in Table 2.

Remark 3.4. Setting $\gamma_{\mathrm{d}} = 0$ results in an entirely *local* damage formulation. Additionally providing a sufficiently 'simple' damage function f_{d}, the internal damage variable κ can be updated in closed form by $\kappa_{n+1} = \max\{q_{n+1}, \kappa_n, \kappa_{\mathrm{d}}\}$ without any local iterations, even though the constitutive update is still fully implicit. In this regard, the reader is referred to Gurtin and Francis [36], Simo [86] and Miehe [66] for related local damage formulations or Steinmann [90] and Liebe et al. [55] for gradient-extended damage approaches.

Remark 3.5. Due to the exponential characteristics of the anisotropic contribution of the local free energy, Eq. (47), it may occur that the local Newton–Raphson scheme does not converge for large loading increments, not even for a comparatively

Table 3
Calculation steps for the damped Newton scheme applied for 5.(e) in Table 2.

0. Given: internal damage variable κ_n at time t_n, increment $\Delta\gamma_{n+1}$, Lagrange multipliers $\gamma_{n+1}^{k+1}, \gamma_{n+1}^{k}$ and $\eta = 1$

1. Evaluate
$f_{n+1}^{k} := \Delta\gamma_{n+1}\left[\Phi_{\mathrm{d}n+1}(\kappa_n + \gamma_{n+1}^{k})\right]$

2. Perform local iteration with adjusted damping parameter η
(a) Evaluate
$f_{n+1}^{k+1} := \Delta\gamma_{n+1}\left[\Phi_{\mathrm{d}n+1}(\kappa_n + \gamma_{n+1}^{k+1})\right]$
(b) Check condition
If $|f_{n+1}^{k+1}| < |f_{n+1}^{k}|$ go to 3.
else go to (c)
(c) Adjust damping parameter
$\eta \hookleftarrow \epsilon\eta$ with $\epsilon = 0.5$
(d) Adjust update
$\gamma_{n+1}^{k+1} = \gamma_{n+1}^{k} + \eta\,\Delta\gamma_{n+1}$

3. Continue with 5.(f) of Table 2

high number of iterations. In order to obtain results and to generally improve the convergence rate, we apply a line search method, i.e., a damped Newton–Raphson iteration scheme. Using this technique, the increment $\Delta\gamma_{n+1} = -\left[\mathrm{d}_\gamma r_{n+1}^{k}\right]^{-1} r_{n+1}^{k}$ obtained from Eq. (83) can be interpreted as an optimal direction of advance towards the solution. The magnitude of $\Delta\gamma_{n+1}$ of the iteration step is controlled (damped) by a parameter η according to

$$\gamma_{n+1}^{k+1} = \gamma_{n+1}^{k} + \eta\,\Delta\gamma_{n+1}, \tag{84}$$

where η is adjusted (reduced) within every iteration. Starting with $\eta = 1$, which corresponds to the standard Newton–Raphson method, then η is successively scaled by 0.5, i.e., $\eta \hookleftarrow \epsilon\eta$ with $\epsilon = 0.5$ if the norm of the residual-like quantity $|f_{n+1}^{k+1}|$ is larger than its respective value $|f_{n+1}^{k}|$ in the previous iteration. The algorithm corresponding to the damped Newton scheme as used in this work is summarised in Table 3.

4. Finite element discretisation

This section deals with the spatial discretisation of the underlying coupled system of non-linear equations by means of the finite element method. In particular, a coupled Bubnov-Galerkin-based finite element discretisation approach with respect to the current configuration is performed. Its specification will include a combination of tri-quadratic serendipity interpolation functions with respect to the displacement field, and tri-linear interpolation functions with respect to the non-local damage field variable. As an advantage of the serendipity elements, one and the same eight-point integration scheme can be applied to both types of differently approximated degrees of freedom. The resulting coupled non-linear system of equations can appropriately be solved with an incremental-iterative Newton–Raphson-type solution procedure.

4.1. Discretisation

The domain $\mathcal{B}_0$ is discretised by n_{el} finite elements, so that

$$\mathcal{B}_0 \approx \mathcal{B}_0^{\mathrm{h}} = \bigcup_{e=1}^{n_{\mathrm{el}}} \mathcal{B}_0^{e}, \tag{85}$$

where every finite element $\mathcal{B}_0^e$ is characterised by $n_{\mathrm{en}}^{\varphi}$ placement-nodes and n_{en}^{ϕ} non-local-damage-nodes. According to the isoparametric concept, the field variables $\boldsymbol{\varphi}$, as well as the geometry $\boldsymbol{X}$, are interpolated by the same shape functions N_I, i.e.,

$$\boldsymbol{X} \approx \boldsymbol{X}^{\mathrm{h}} = \sum_{I=1}^{n_{\mathrm{en}}} N_I(\xi)\,\boldsymbol{X}_I, \quad \boldsymbol{\varphi} \approx \boldsymbol{\varphi}^{\mathrm{h}} = \sum_{I=1}^{n_{\mathrm{en}}} N_I(\xi)\,\boldsymbol{\varphi}_I. \tag{86}$$

and transformed to a hexahedral reference element with coordinates $\boldsymbol{\xi} := \{\xi, \eta, \zeta\} \in \bar{\mathcal{B}}$, where $\bar{\mathcal{B}} := \{\boldsymbol{\xi} \in \mathbb{R}^3 \,|\, -1 \leqslant \chi \leqslant +1;\ \chi = \xi, \eta, \zeta\}$ denotes the reference domain, see Fig. 4. In the present context, the number of displacement-nodes and non-local-damage-nodes per element—and consequently the related shape functions—do not necessarily have to coincide, i.e., $n_{\mathrm{en}}^{\varphi} \neq n_{\mathrm{en}}^{\phi}$ and $N_I^{\varphi} \neq N_I^{\phi}$, respectively. Following Dimitrijević [27], we use the denomination *quasi-isoparametric* approximation instead of *isoparametric* approximation, see Fig. 4. The corresponding field variables, i.e., the placement $\boldsymbol{\varphi}$ and the non-local damage variable ϕ as well as their spatial gradients $\nabla_{\boldsymbol{X}}\boldsymbol{\varphi}$ and $\nabla_{\boldsymbol{X}}\phi$, are approximated by means of the product of shape functions $N_I^{\alpha}(\xi)$, $\alpha = \varphi, \phi$ and discrete nodal degrees of freedom $\boldsymbol{\varphi}_I$ and ϕ_I summed over $n_{\mathrm{en}}^{\varphi}$ respectively n_{en}^{ϕ} nodes per element, i.e.,

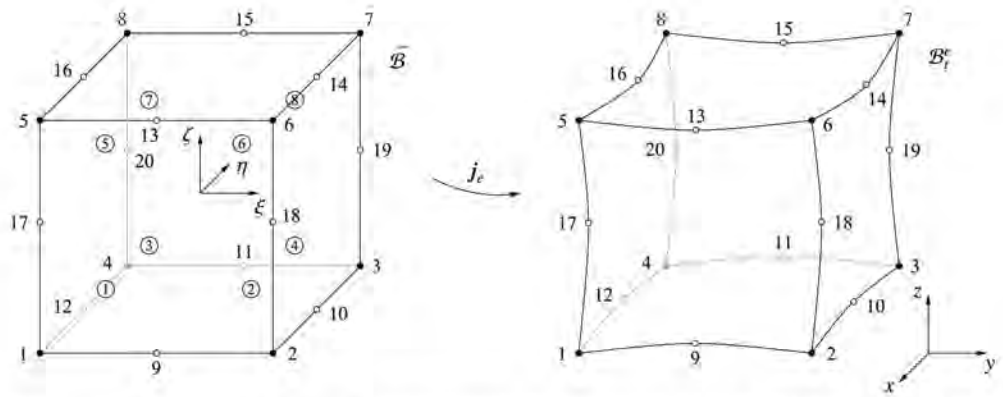

Fig. 4. Quasi-isoparametric 20-node hexahedral element in reference coordinate space $\{\xi, \eta, \zeta\}$ and in physical coordinate space $\{x, y, z\}$. Deformation-related degrees of freedom $\boldsymbol{\varphi}_I$ are referred to all nodes (• and ▫) whereas non-local-damage-related degrees of freedom ϕ_I are referred to the vertex nodes (•) only. The integration points are consecutively numbered by ①–⑧.

$$\boldsymbol{\varphi}^{\mathrm{h}} = \sum_{I=1}^{n_{\mathrm{en}}^{\varphi}} N_I^{\varphi}\, \boldsymbol{\varphi}_I, \qquad \phi^{\mathrm{h}} = \sum_{K=1}^{n_{\mathrm{en}}^{\phi}} N_K^{\phi}\, \phi_K, \tag{87}$$

$$\nabla_{\boldsymbol{x}} \boldsymbol{\varphi}^{\mathrm{h}} = \sum_{I=1}^{n_{\mathrm{en}}^{\varphi}} \boldsymbol{\varphi}_I \otimes \nabla_{\boldsymbol{x}} N_I^{\varphi}, \qquad \nabla_{\boldsymbol{x}} \phi^{\mathrm{h}} = \sum_{K=1}^{n_{\mathrm{en}}^{\phi}} \phi_K \nabla_{\boldsymbol{x}} N_K^{\phi}. \tag{88}$$

According to the Bubnov-Galerkin method, an analogous approximation is applied for the variations of field variables and corresponding gradients as

$$\delta\boldsymbol{\varphi}^{\mathrm{h}} = \sum_{I=1}^{n_{\mathrm{en}}^{\varphi}} N_I^{\varphi}\, \delta\boldsymbol{\varphi}_I, \qquad \delta\phi^{\mathrm{h}} = \sum_{K=1}^{n_{\mathrm{en}}^{\phi}} N_K^{\phi}\, \delta\phi_K, \tag{89}$$

$$\nabla_{\boldsymbol{x}} \delta\boldsymbol{\varphi}^{\mathrm{h}} = \sum_{I=1}^{n_{\mathrm{en}}^{\varphi}} \delta\boldsymbol{\varphi}_I \otimes \nabla_{\boldsymbol{x}} N_I^{\varphi}, \qquad \nabla_{\boldsymbol{x}} \delta\phi^{\mathrm{h}} = \sum_{K=1}^{n_{\mathrm{en}}^{\phi}} \delta\phi_K \nabla_{\boldsymbol{x}} N_K^{\phi}, \tag{90}$$

where the spatial and material gradients of the shape functions N_I can be expressed as

$$\nabla_{\boldsymbol{x}} N_I^{\varphi} = \boldsymbol{j}_e^{-\mathrm{t}} \cdot \nabla_{\xi} N_I^{\varphi} \quad \text{with} \quad \boldsymbol{j}_e = \nabla_{\xi} \boldsymbol{\varphi}^{\mathrm{h}} = \sum_{I=1}^{n_{\mathrm{en}}^{\varphi}} \boldsymbol{\varphi}_I \otimes \nabla_{\xi} N_I^{\varphi}, \tag{91}$$

$$\nabla_{\boldsymbol{X}} N_I^{\varphi} = \boldsymbol{J}_e^{-\mathrm{t}} \cdot \nabla_{\xi} N_I^{\varphi} \quad \text{with} \quad \boldsymbol{J}_e = \nabla_{\xi} \boldsymbol{X}^{\mathrm{h}} = \sum_{I=1}^{n_{\mathrm{en}}^{\varphi}} \boldsymbol{X}_I \otimes \nabla_{\xi} N_I^{\varphi}. \tag{92}$$

Similar relations for the gradients of N_K^{ϕ} follow by analogy with (91), (92). As a consequence, the discrete deformation gradient can be represented in terms of the spatial and material Jacobians of the isoparametric transformation as

$$\boldsymbol{F}^{\mathrm{h}} := \nabla_{\boldsymbol{X}} \boldsymbol{\varphi}^{\mathrm{h}} = \boldsymbol{j}_e \cdot \boldsymbol{J}_e^{-1}. \tag{93}$$

Compatibility provided, the discretised weak form on element level can be written as the difference of the element-specific expressions for the internal and external virtual work related expressions $\delta_{\boldsymbol{\varphi}} W_{\mathrm{int}}^e$ and $\delta_{\boldsymbol{\varphi}} W_{\mathrm{ext}}^e$, so that

$$\delta_{\boldsymbol{\varphi}} W^e = \delta_{\boldsymbol{\varphi}} W_{\mathrm{int}}^e - \delta_{\boldsymbol{\varphi}} W_{\mathrm{ext}}^e = \boldsymbol{0} \quad \forall\ \delta\boldsymbol{\varphi}_I, \tag{94}$$

$$\delta_{\phi} W^e = \delta_{\phi} W_{\mathrm{int}}^e - \delta_{\phi} W_{\mathrm{ext}}^e = 0 \quad \forall\ \delta\phi_K, \tag{95}$$

where the discrete representations take the following forms

$$\delta_{\boldsymbol{\varphi}} W_{\mathrm{int}}^e = \sum_{I=1}^{n_{\mathrm{en}}^{\varphi}} \delta\boldsymbol{\varphi}_I \cdot \boldsymbol{f}_{\mathrm{int}\,I}^{\varphi} \quad \text{with} \quad \boldsymbol{f}_{\mathrm{int}\,I}^{\varphi} = \int_{\mathcal{B}_t^e} \nabla_{\boldsymbol{x}} N_I^{\varphi} \cdot \boldsymbol{\sigma}\, \mathrm{d}v, \tag{96}$$

$$\delta_{\boldsymbol{\varphi}} W^e_{\text{ext}} = \sum_{I=1}^{n^{\varphi}_{\text{en}}} \delta\boldsymbol{\varphi}_I \cdot \boldsymbol{f}^{\varphi}_{\text{ext}\,I} \quad \text{with} \quad \boldsymbol{f}^{\varphi}_{\text{ext}\,I} = \int_{\mathcal{B}^e_t} N^{\varphi}_I \bar{\boldsymbol{b}}\, \mathrm{d}v + \int_{\partial\mathcal{B}^e_t} N^{\varphi}_I \bar{\boldsymbol{t}}\, \mathrm{d}a, \tag{97}$$

$$\delta_{\phi} W^e_{\text{int}} = \sum_{K=1}^{n^{\phi}_{\text{en}}} \delta\phi_K f^{\phi}_{\text{int}\,K} \quad \text{with} \quad f^{\phi}_{\text{int}\,K} = \int_{\mathcal{B}^e_t} \nabla_{\boldsymbol{x}} N^{\phi}_K \cdot \boldsymbol{y}\, \mathrm{d}v, \tag{98}$$

$$\delta_{\phi} W^e_{\text{ext}} = \sum_{K=1}^{n^{\phi}_{\text{en}}} \delta\phi_K f^{\phi}_{\text{ext}\,K} \quad \text{with} \quad f^{\phi}_{\text{ext}\,K} = \int_{\mathcal{B}^e_t} N^{\phi}_K y\, \mathrm{d}v. \tag{99}$$

According to the fundamental lemma of calculus of variations, Eqs. (94) and (95) are equivalent to the equilibrium of internal and external nodal variables in every $I = 1, \ldots, n^{\varphi}_{\text{en}}$ placement-node, respectively $K = 1, \ldots, n^{\phi}_{\text{en}}$ non-local-damage-node of a finite element e. This results in the node-specific residual form of the present coupled problem

$$\boldsymbol{r}^{\varphi}_I = \boldsymbol{f}^{\varphi}_{\text{int}\,I} - \boldsymbol{f}^{\varphi}_{\text{ext}\,I} = \boldsymbol{0} \quad \forall\ I = 1, \ldots, n^{\varphi}_{\text{en}}, \tag{100}$$

$$r^{\phi}_K = f^{\phi}_{\text{int}\,K} - f^{\phi}_{\text{ext}\,K} = 0 \quad \forall\ K = 1, \ldots, n^{\phi}_{\text{en}}. \tag{101}$$

4.2. Linearisation

The governing highly non-linear system of Eqs. (100) and (101) includes coupling between the motion $\boldsymbol{\varphi}$ and the non-local damage field ϕ, which itself is linked to the local damage variable κ by means of the penalty contributions. To solve this non-linear system of equations, we use an incremental-iterative Newton–Raphson scheme. In what follows, we omit the subscript index $n+1$ associated with time t_{n+1} for the sake of readability. A Taylor series expansion around the solution at the current iteration step l—terms of quadratic and higher order being neglected—gives

$$\boldsymbol{r}^{\varphi}_{I\,l+1} = \boldsymbol{r}^{\varphi}_{Il} + \Delta\boldsymbol{r}^{\varphi}_I = \boldsymbol{0}, \tag{102}$$

$$r^{\phi}_{K\,l+1} = r^{\phi}_{Kl} + \Delta r^{\phi}_K = 0, \tag{103}$$

with the node-specific increments of the residuals

$$\Delta\boldsymbol{r}^{\varphi}_I = \sum_{J=1}^{n^{\varphi}_{\text{en}}} \frac{\mathrm{d}\boldsymbol{r}^{\varphi}_I}{\mathrm{d}\boldsymbol{\varphi}_J} \cdot \Delta\boldsymbol{\varphi}_J + \sum_{L=1}^{n^{\phi}_{\text{en}}} \frac{\mathrm{d}\boldsymbol{r}^{\varphi}_I}{\mathrm{d}\phi_L} \Delta\phi_L, \tag{104}$$

$$\Delta r^{\phi}_K = \sum_{J=1}^{n^{\varphi}_{\text{en}}} \frac{\mathrm{d}r^{\phi}_K}{\mathrm{d}\boldsymbol{\varphi}_J} \cdot \Delta\boldsymbol{\varphi}_J + \sum_{L=1}^{n^{\phi}_{\text{en}}} \frac{\mathrm{d}r^{\phi}_K}{\mathrm{d}\phi_L} \Delta\phi_L. \tag{105}$$

Herein, the increments $\Delta\boldsymbol{\varphi}_J = \boldsymbol{\varphi}_{J\,l+1} - \boldsymbol{\varphi}_{Jl}$ and $\Delta\phi_L = \phi_{L\,l+1} - \phi_{Ll}$ represent the difference of the discrete nodal degrees of freedom at iteration-step $l+1$ and l. Assuming 'dead loads', the node-specific sub-matrices of the Jacobian are deduced as

$$\boldsymbol{K}^{\varphi\varphi}_{IJ} = \frac{\mathrm{d}\boldsymbol{r}^{\varphi}_I}{\mathrm{d}\boldsymbol{\varphi}_J} = \int_{\mathcal{B}^e_t} \nabla_{\boldsymbol{x}} N^{\varphi}_I \cdot \mathbf{e} \cdot \nabla_{\boldsymbol{x}} N^{\varphi}_J\, \mathrm{d}v + \int_{\mathcal{B}^e_t} \left[\nabla_{\boldsymbol{x}} N^{\varphi}_I \cdot \boldsymbol{\sigma} \cdot \nabla_{\boldsymbol{x}} N^{\varphi}_J\right] \boldsymbol{I}\, \mathrm{d}v, \tag{106}$$

$$\boldsymbol{K}^{\varphi\phi}_{IL} = \frac{\mathrm{d}\boldsymbol{r}^{\varphi}_I}{\mathrm{d}\phi_L} = \int_{\mathcal{B}^e_t} \nabla_{\boldsymbol{x}} N^{\varphi}_I \cdot \frac{\mathrm{d}\boldsymbol{\sigma}}{\mathrm{d}\phi} N^{\phi}_L\, \mathrm{d}v, \tag{107}$$

$$\boldsymbol{K}^{\phi\varphi}_{KJ} = \frac{\mathrm{d}r^{\phi}_K}{\mathrm{d}\boldsymbol{\varphi}_J} = \int_{\mathcal{B}^e_t} N^{\phi}_K\, 2\, \frac{\mathrm{d}y}{\mathrm{d}\boldsymbol{g}} \cdot \nabla_{\boldsymbol{x}} N^{\varphi}_J\, \mathrm{d}v, \tag{108}$$

$$K^{\phi\phi}_{KL} = \frac{\mathrm{d}r^{\phi}_K}{\mathrm{d}\phi_L} = \int_{\mathcal{B}^e_t} N^{\phi}_K \frac{\mathrm{d}y}{\mathrm{d}\phi} N^{\phi}_L\, \mathrm{d}v + \int_{\mathcal{B}^e_t} \nabla_{\boldsymbol{x}} N^{\phi}_K \cdot \frac{\mathrm{d}\boldsymbol{y}}{\mathrm{d}\nabla_{\boldsymbol{x}}\phi} \cdot \nabla_{\boldsymbol{x}} N^{\phi}_L\, \mathrm{d}v. \tag{109}$$

Furthermore, $\mathbf{e}$, $\mathrm{d}\boldsymbol{\sigma}/\mathrm{d}\phi$, $2\,\mathrm{d}y/\mathrm{d}\boldsymbol{g}$, $\mathrm{d}y/\mathrm{d}\phi$ and $\mathrm{d}\boldsymbol{y}/\mathrm{d}\nabla_{\boldsymbol{x}}\phi$ denote partitions of the consistent tangent-moduli as specified in Appendix A. The resulting system of equations is clearly symmetric—since a variational framework is used—so that $\boldsymbol{K}^{\varphi\phi}_{IL} = \boldsymbol{K}^{\phi\varphi\,\mathrm{T}}_{KJ}$ which conveniently enables the use of symmetric equation solvers.

The node-specific residual (load) vectors $(96)_2$–$(99)_2$ and the stiffness contributions (106)–(109) can be summarised as the element-based residual vector, and stiffness matrix

$$\boldsymbol{r}_e^{\varphi} := [\boldsymbol{r}_I^{\varphi}] \quad \boldsymbol{r}_e^{\phi} := [r_K^{\phi}] \quad \Delta\boldsymbol{\varphi}_e := [\Delta\boldsymbol{\varphi}_I] \quad \Delta\boldsymbol{\phi}_e := [\Delta\phi_K],$$
$$\boldsymbol{K}_e^{\varphi\varphi} := [\boldsymbol{K}_{IJ}^{\varphi\varphi}] \quad \boldsymbol{K}_e^{\varphi\phi} := [\boldsymbol{K}_{IL}^{\varphi\phi}] \quad \boldsymbol{K}_e^{\phi\varphi} := [\boldsymbol{K}_{KJ}^{\phi\varphi}] \quad \boldsymbol{K}_e^{\phi\phi} := [K_{KL}^{\phi\phi}].$$

This results in the following linearised system of equations on element level

$$\begin{bmatrix} \boldsymbol{r}_e^{\varphi} \\ \boldsymbol{r}_e^{\phi} \end{bmatrix} + \begin{bmatrix} \boldsymbol{K}_e^{\varphi\varphi} & \boldsymbol{K}_e^{\varphi\phi} \\ \boldsymbol{K}_e^{\phi\varphi} & \boldsymbol{K}_e^{\phi\phi} \end{bmatrix} \cdot \begin{bmatrix} \Delta\boldsymbol{\varphi}_e \\ \Delta\boldsymbol{\phi}_e \end{bmatrix} = \begin{bmatrix} \boldsymbol{0} \\ \boldsymbol{0} \end{bmatrix} \tag{110}$$

for the determination of the unknown increments of the element degrees of freedom $\Delta\boldsymbol{\varphi}_e$ and $\Delta\boldsymbol{\phi}_e$. Consequently, the assembly of all elements

$$\boldsymbol{r} := \mathop{\mathsf{A}}_{e=1}^{n_{\mathrm{el}}} \begin{bmatrix} \boldsymbol{r}_e^{\varphi} \\ \boldsymbol{r}_e^{\phi} \end{bmatrix}, \quad \boldsymbol{K} = \mathop{\mathsf{A}}_{e=1}^{n_{\mathrm{el}}} \begin{bmatrix} \boldsymbol{K}_e^{\varphi\varphi} & \boldsymbol{K}_e^{\varphi\phi} \\ \boldsymbol{K}_e^{\phi\varphi} & \boldsymbol{K}_e^{\phi\phi} \end{bmatrix}, \quad \Delta\boldsymbol{d} = \mathop{\mathsf{A}}_{e=1}^{n_{\mathrm{el}}} \begin{bmatrix} \Delta\boldsymbol{\varphi}_e \\ \Delta\boldsymbol{\phi}_e \end{bmatrix},$$

results in the global linearised system of equations in the I-th iteration step

$$\boldsymbol{r}_I + \boldsymbol{K}_I \cdot \Delta\boldsymbol{d} = \boldsymbol{0} \quad \text{with} \quad \Delta\boldsymbol{d} = \boldsymbol{d}_{I+1} - \boldsymbol{d}_I, \tag{111}$$

with $\boldsymbol{K}_I$ being the global tangent stiffness matrix, $\Delta\boldsymbol{d}$ the global incremental vector of degrees of freedom, $\boldsymbol{r}_I$ the global residual vector including the internal and external system loads and the incorporation of Dirichlet boundary conditions not explicitly indicated here.

Remark 4.1. The integrals in Eqs. (96)–(99) and (106)–(109) are typically evaluated numerically at discrete integration points by means of appropriate integration or rather quadrature rules, such as Gaussian quadrature, see Hughes [41]. For two-dimensional problems, Dimitrijević and Hackl [28] employed a full 3×3-quadrature. However, following de Borst and Pamin [21], we use a reduced $2 \times 2 \times 2$ Gaussian quadrature rule, see Fig. 4. As a major benefit, one and the same reduced quadrature rule can conveniently be applied to integrate the expressions related to the tri-quadratic placement field as well as to the tri-linear non-local damage field variable. In this regard, we take advantage of the fact that serendipity elements show no zero-energy modes for reduced quadrature rules if more than one element is used, cf. Hughes [41, pp. 240/241].

5. Numerical examples

In this section, we apply the proposed gradient-enhanced damage model to three representative three-dimensional homogeneous and inhomogeneous deformation problems. We first investigate a homogeneous state under uniaxial tension in order to illustrate the basic constitutive characteristics of the local damage formulation. Secondly, we consider a displacement-driven isotropic and anisotropic plate with a hole in order to emphasise the regularisation properties of the model following the gradient-enhancement strategy. Finally, to show the capabilities of the approach with regard to biomechanics-related problems, we study a force-driven example of an anisotropic artery-like tube subjected to internal pressure.

The proposed gradient-enhanced damage model is incorporated within the commercial finite-element software Abaqus/Standard by means of the user subroutine UEL, which allows the implementation of general multi-field non-linear element-formulations, for details, see Appendix B or the Abaqus 6.11 Documentation [1].

5.1. Test 1 — homogeneous uniaxial tension

As an introductive numerical example to emphasise the properties of the basic constitutive characteristics of the local damage formulation, we next discuss a deformation under isochoric uniaxial tension with

$$\boldsymbol{F} = \lambda_1 \boldsymbol{e}_1 \otimes \boldsymbol{e}_1 + \lambda_1^{-1/2} [\boldsymbol{e}_2 \otimes \boldsymbol{e}_2 + \boldsymbol{e}_3 \otimes \boldsymbol{e}_3]. \tag{112}$$

The frame $\{\boldsymbol{e}_1, \boldsymbol{e}_2, \boldsymbol{e}_3\}$ represents a fixed orthonormal base system. A monotonically increasing load is applied up to an axial stretch of $\lambda_1 = 2.0$. With regard to the structural properties, both families of fibers are oriented with respect to the axial $\boldsymbol{e}_1$-direction, i.e., $\beta_{1,2} = 0.0$ deg where $\beta_{1,2} = \sphericalangle(\boldsymbol{a}_{0\,1,2}, \boldsymbol{e}_1)$. As the dispersion parameter $\varkappa$ is set to zero, transverse isotropy is recovered for every fibre family. The material parameters used for this example are summarised in Table 4 in column 'Test 1'.

For a homogeneous deformation, the gradient-related free energy term (49) is not activated, i.e., $\nabla_{\boldsymbol{X}}\phi = \boldsymbol{0}$. In consequence, the driving force is represented only by the local term $q = q^{\mathrm{loc}}$ and the damage model's behaviour is in accordance with a purely local model. Therefore, only the influence of the local damage parameters, i.e., the threshold κ_{d} and the saturation parameter η_{d}, is studied in Fig. 5, where the left column 5(a,c,e) is associated with values of $\kappa_{\mathrm{d}} = 0.0$ kPa, and where the right column 5(b,d,f) corresponds to values of $\kappa_{\mathrm{d}} = 16.0$ kPa. The stress-stretch response is shown in Fig. 5(a) and (b) where $P_{11} = \lambda_1^{-1} \boldsymbol{e}_1 \cdot \boldsymbol{\sigma} \cdot \boldsymbol{e}_1$. The two solid black curves represent the fully elastic response of two extreme cases: the isotropic neo-Hookean matrix in the lower solid black curve, and the overall elastic response composed of the isotropic neo-Hookean *and* the anisotropic exponential part, in the upper solid black curve. The inelastic damage-related load–displacement curves

Table 4
Set of structural and material parameters used for boundary value problems in Sections 5.1, 5.2, and 5.3.

Type	Symbol	Description	Value			Unit
			Test 1	Test 2	Test 3	
Structural	$\beta_{1,2}$	Fibre orientation angles	0.0	–	0.0	deg
	$\varkappa$	Dispersion parameter	0.0	1/3	0.0	–
Elastic	μ_e	Shear modulus	14.5805	14.5805	14.5805	kPa
	κ_e	Bulk modulus	145.805	729.025	145.805	kPa
	k_1	Elastic constant	7.290	218.708	14.5805	kPa
	k_2	Elastic constant	0.1	150.0	2.1	–
Regularisation	c_d	Degree of regularisation	–	{0, 10, 100, 500, 1000}	1000	$\text{kPa}^{-1}\,\text{mm}^2$
	β_d	Penalty parameter	–	1000	1000	kPa^{-1}
	γ_d	(Non-)local switch	–	1.0	1.0	–
Damage	η_d	Saturation parameter	$\{1, 10^{-1}, 10^{-2}, 10^{-3}\}$	4.0	4.0	kPa^{-1}
	κ_d	Damage threshold	{0.0, 16.0}	0.2	{0.5, 1.0, 2.5}	kPa

can be seen between the two solid black curves. Basically, the material first shows an elastic response according to the exponential constitutive relation. After a certain loading level, the material softens and deviates from the elastic path. Caused by the loss of stiffness, the stress starts to decrease with increasing stretch λ_1 and the curve finally drops towards the black curve which represents the elastic response of the undamaged neo-Hookean ground substance.

It becomes apparent that higher damage saturation values η_d accelerate the damage process. Generally, it is expected that the purely neo-Hookean response is recovered upon complete damage of the fibers. This can be clearly verified for damage saturation values of $\eta_d = \{1, 10^{-1}\}$ kPa^{-1}, whereas for saturation values of $\eta_d = \{10^{-2}, 10^{-3}\}$ kPa^{-1} complete damage of the fibers cannot be obtained within the deformation range considered. Furthermore, we observe that the higher damage threshold of $\kappa_d = 16.0$ kPa leads to a delay of the damage initiation.

The influence of the damage threshold κ_d is illustrated in Fig. 5(c) and (d) where the evolution of the internal damage variable κ is shown. Here, we clearly observe how κ_d controls the onset of damage for $\kappa_d = 0.0$ kPa. Damage starts at the very beginning of the deformation, see Fig. 5(c), and continuously evolves, i.e., $\dot{\kappa} > 0$, according to $\kappa = q^{\text{loc}} = \Psi^{\text{ani}}$. The evolution of $\dot{\kappa} > 0$ continues until the fibre-reinforced material is completely damaged. For $\kappa_d = 16.0$ kPa, see Fig. 5(d), the damage process is delayed and starts once the driving force $q^{\text{loc}} = \Psi^{\text{ani}}$ exceeds the damage threshold value of $\kappa_d = 16.0$ kPa, i.e., $q^{\text{loc}} > \kappa_d$. After initiation of the damage process, the damage evolution as represented by $\dot{\kappa} > 0$ continues, up to complete damage of the fibre-reinforced material.

Fig. 5(e) and (f) highlight the evolution of the damage function f_d, see Eq. (70). By comparing Fig. 5(e) and (f), it becomes apparent how κ_d controls the onset of damage. Furthermore, we clearly observe that damage evolves faster for higher values of η_d.

5.2. Test 2 – isotropic plate with a hole

As a second numerical example, we consider the deformation of an isotropic plate with a hole under Dirichlet boundary conditions. The geometry and its dimensions are depicted in Fig. 6(a). The plate is assumed to be clamped at the bottom while non-vanishing displacements u are imposed in Y-direction on the top—the remaining displacement degrees of freedom at the top are set to zero. Due to the symmetry and the assumed isotropy of the specimen, only one eighth of the structure is discretised, i.e., the upper right front part of the plate. The non-local damage-related field variable ϕ is initialised as the value of the damage threshold κ_d, i.e., $\phi|_{t_0} = \kappa_d$. Full isotropy is ensured by setting the dispersion parameter to $\varkappa = 1/3$ which renders the response to become independent of β_1 and β_2. The material parameters used for this example are summarised in Table 4 in column 'Test 2'. In view of the choice of the penalty parameter β_d, higher values of β_d generally ensure a better fulfilment of the constraint between ϕ and κ which also turned out to improve the convergence of the *local* Newton–Raphson scheme. For very large values of β_d, however, the global system of equations tends to be ill-conditioned—in the context that the eigenvalues of the global tangent operator possess extremely different orders of magnitude—and it therefore may occur that the *global* Newton–Raphson scheme does not converge. In either case, a reasonable choice of β_d depends on the specific boundary value problem and material parameters chosen, so that also smaller values of β_d may result in a good correspondence between ϕ and κ.

For this example, a displacement-controlled cyclic tension test is considered which can be divided in three stages, see Fig. 6(a): In the first stage the plate is loaded up to a prescribed longitudinal displacement of $u = 24$ mm at the top surface. In a second stage the plate is unloaded until the top surface recovers its initial configuration. Finally, in the third stage the plate is once again loaded up to $u = 30$ mm.

The mechanical response of the plate with hole is illustrated by the load–displacement-curve in Fig. 6(b). The force f represents the resultant reaction force in Y-direction related to the whole specimen, i.e., not only to one eighth of the plate which is considered for the discretisation. Once more, the two solid black curves represent the fully elastic response of

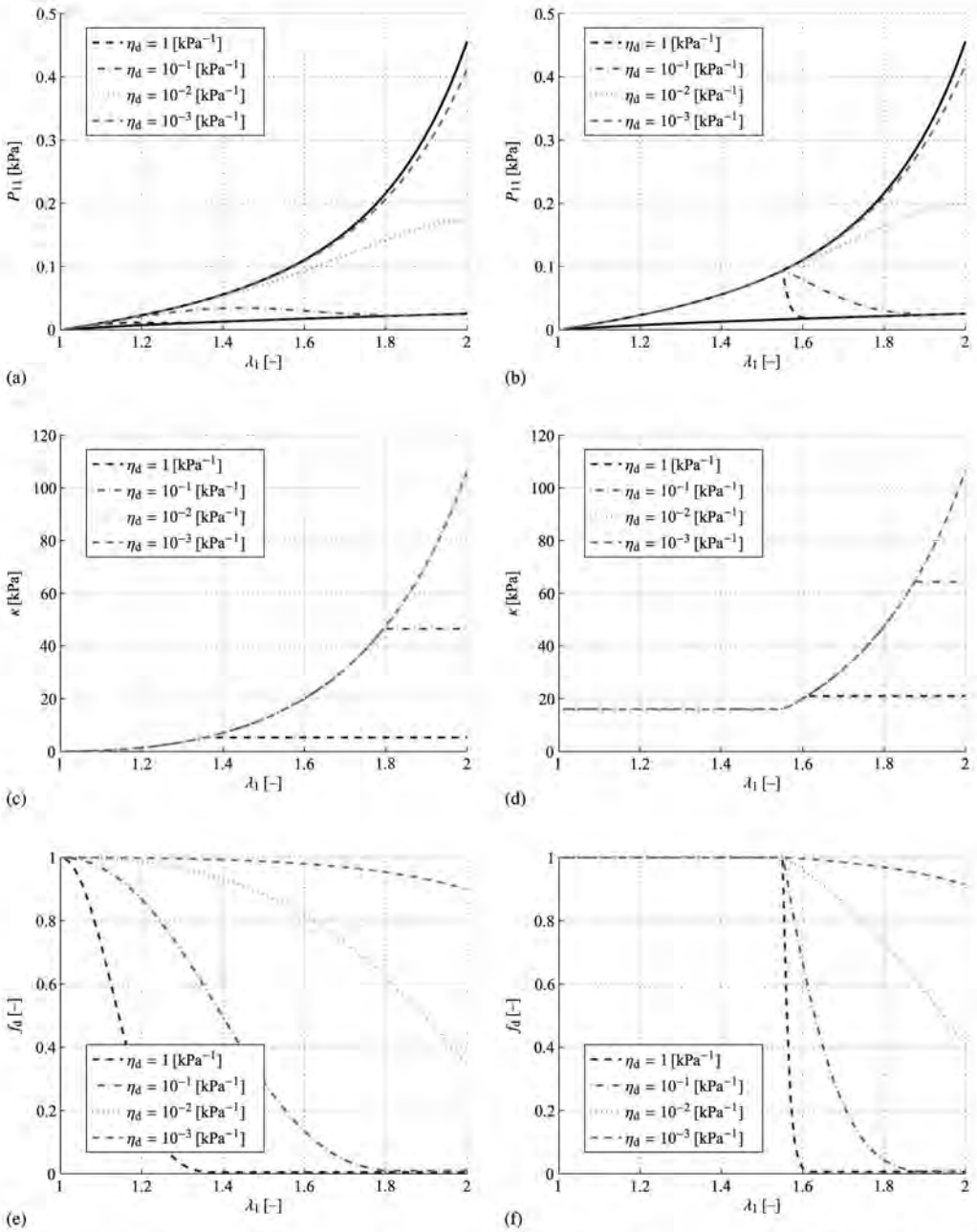

Fig. 5. Uniaxial isochoric tension: Influence of the saturation parameter η_d. Subfigures (a,c,e) are associated with the damage threshold $\kappa_d = 0.0$ kPa. Subfigures (b,d,f) are associated with the damage threshold $\kappa_d = 16.0$ kPa. Subfigures (a,b) show the stress-stretch response. The solid black curves represent the elastic response of the isotropic neo-Hookean matrix (lower solid black curve) and the overall elastic response composed of the isotropic neo-Hookean and the anisotropic exponential model (upper solid black curve). Subfigures (c,d) show the evolution of the internal damage variable κ. Subfigures (e,f) show the evolution of the damage function $f_d(\kappa) \in (0, 1]$.

the isotropic neo-Hookean matrix in the lower solid black curve and the overall elastic response composed of the isotropic neo-Hookean *and* the anisotropic exponential part in the upper solid black curve. We observe that the response of the plate initially follows the elastic load–displacement path, also referred to as primary loading path. Upon a certain loading level of approx. $u = 17$ mm, the response deviates from the elastic path and slightly tends towards the purely neo-Hookean response. Subsequently, the plate is unloaded and completely returns to its unstressed reference state. It becomes apparent that the first loading–unloading cycle is associated with dissipation of energy, represented by the characteristic hysteresis behaviour and the area between the loading and unloading-curves, respectively. When the plate is re-loaded, the

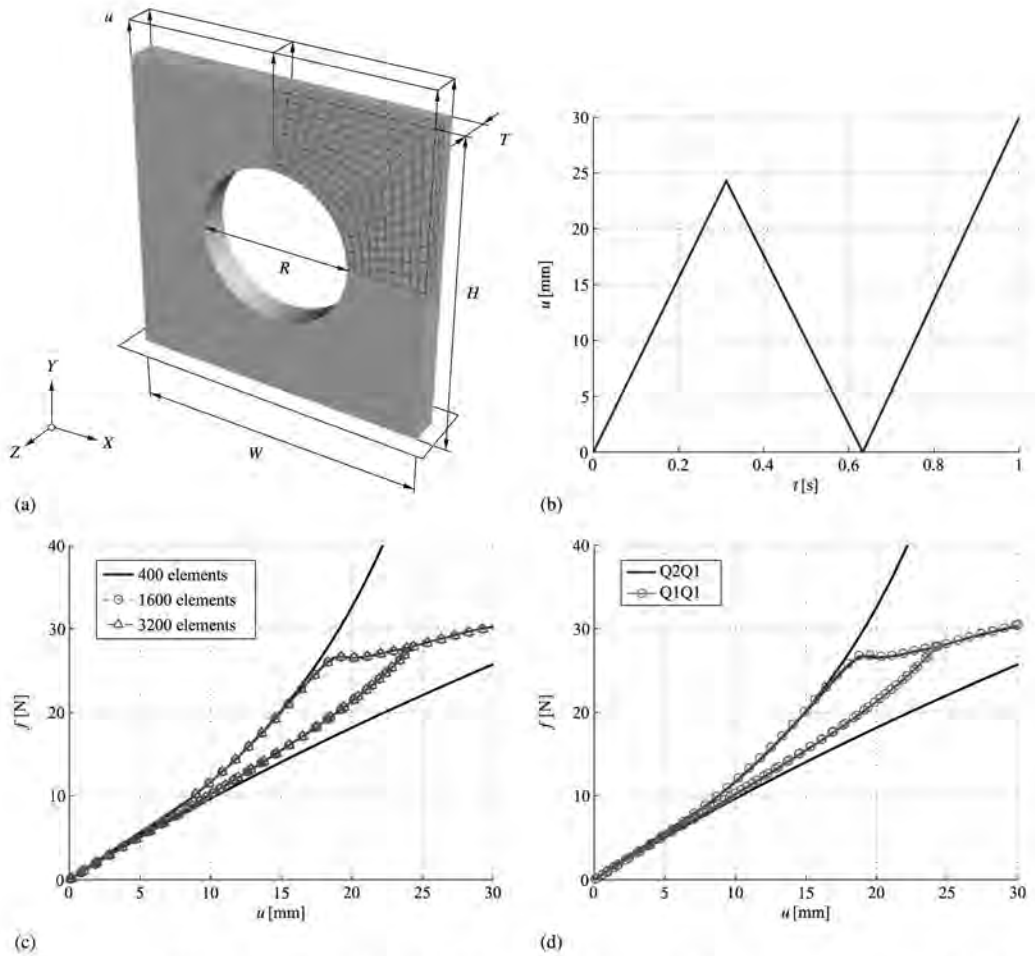

Fig. 6. Isotropic plate with a hole. (a) Dimensions ($R = 100$ mm, $W = H = 200$ mm, $T = 20$ mm) and imposed boundary conditions. Only one eighth of the plate is discretised. (b) Cyclic loading history. (c) Force–displacement response and investigation of mesh-sensitivity. The solid black curves represent the elastic response of the isotropic neo-Hookean matrix (lower solid black curve) and the overall elastic response composed of the isotropic neo-Hookean *and* the anisotropic exponential model (upper solid black curve). (d) Force–displacement response due to cyclic loading for the element types Q2Q1 and Q1Q1 using a 400 element mesh.

load–displacement response first follows the unloading path again, until the continuation of the primary loading path is activated. We note that, in contrast to the homogeneous deformation example discussed above and within the loading levels considered, the curve does not fully drop onto the black curve representing the elastic response of the undamaged neo-Hookean ground substance. Clearly, this is a consequence of the overall inhomogeneous behaviour of the plate with hole, which also involves regions showing less or no damage at all.

One of the major benefits of using a gradient-enhanced damage model lies in the inherent mesh-objectivity of the formulation. In other words, the energy dissipation due to the inelastic processes associated with damage should be independent of the discretisation for sufficiently large values of c_d and sufficiently fine discretisations. In order to illustrate this property, three different discretisations including 400, 1600 and 3200 elements are discussed. The results are presented in Fig. 6(b) where it becomes apparent that the load–displacement responses almost completely coincide. It can therefore be concluded that, for sufficiently large values of c_d, the dissipation is always the same and the structural response is mesh-independent.

The same conclusion can be drawn from Fig. 7, where the contour plots of the damage function $f_d(\kappa)$ for the three different meshes turn out to be practically identical. Furthermore, damage is more prominent around the bottom edge of the specimen, the area with the highest stresses. This is consistent with the energy-driven damage formulation, see Section 3.3.

From Section 3.3, we recall that the gradient parameter c_d controls the quasi-non-local character of the formulation and characterises the degree of gradient regularisation. As a special case, $c_d = 0$ results in a local model. The strong influence of c_d on the mechanical response is illustrated in Figs. 8 and 9 where values of $c_d = \{0, 10, 100, 500, 1000\}$ [kPa^{-1} mm^2] are

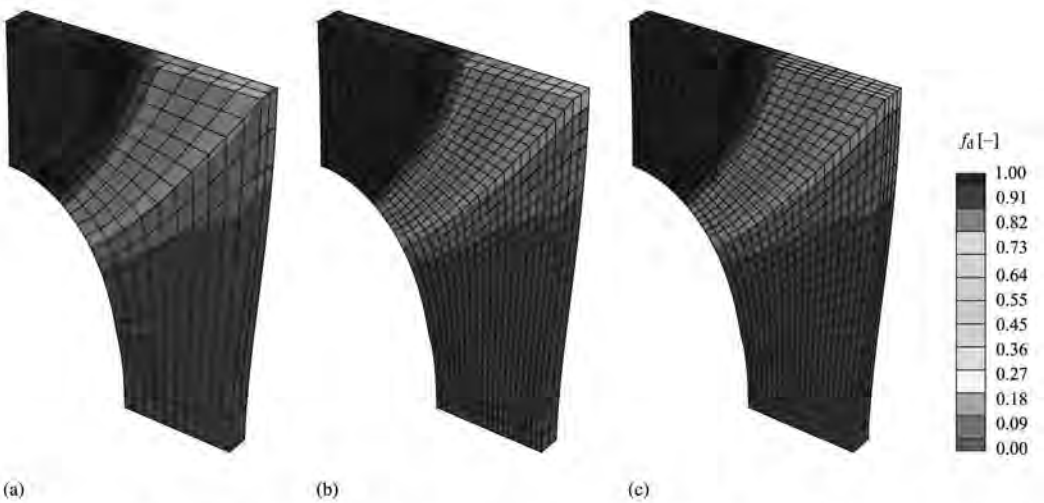

Fig. 7. Isotropic plate with a hole. Contour plots of the damage function $f_d(\kappa) \in \langle 0, 1]$ at $u = 30$ mm for three different discretisations: (a) 400 elements, (b) 1600 elements, (c) 3200 elements.

investigated for a mesh of 400 elements. Generally, higher values of c_d increase the localisation zone. As a consequence, larger values of c_d increase the dissipation-related area under the load displacement curve in Fig. 9. Computationally, small values of the gradient parameter $c_d \to 0$ may lead to numerical instabilities for the solution of the underlying non-linear system of equations, as the local tangent operator might become singular, so that even no global convergence may be obtained. This effect is underlined by Fig. 9, where the calculation for $c_d = 0.0\ \text{kPa}^{-1}\ \text{mm}^2$ cannot be advanced into the softening range but stops at $u = 14.22$ mm. With regard to the contour plots of the damage function $f_d(\kappa)$ shown in Fig. 8, we observe that the deformation patterns are not strongly localised in the form of pronounced narrow damage bands. This is caused by the remaining stiffness of the undamaged isotropic matrix material. A material with a smaller influence of the matrix material would increase the damage evolution on the specimen considerably and, in consequence, would result in a much more pronounced localisation behaviour. This effect is further studied in Section 5.3.2.

Up to now, the number of displacement-nodes and non-local-damage-nodes per element have been chosen as $n_{en}^{\varphi} = 20$ and $n_{en}^{\psi} = 8$, respectively, see Fig. 4. With regard to the degree of the polynomial interpolation function, this implies a tri-quadratic serendipity interpolation of the displacements and a tri-linear interpolation of the non-local damage field variable, the related element type being referred to as Q2Q1-element. In the following, the Q2Q1-element is compared to the Q1Q1-element which is associated with $n_{en}^{\varphi} = n_{en}^{\psi} = 8$ and consequently exhibits the same tri-linear interpolation order for the displacement and the non-local damage variable field.

Fig. 6(d) shows the force–displacement response of the isotropic plate with a hole when using the coarsest discretisation considered of 400 elements for both element types Q2Q1 and Q1Q1. It becomes apparent that the Q1Q1-element is able to almost exactly reproduce the force–displacement-curve associated with the Q2Q1-formulation. Only very small deviations can be observed. The same holds for the finer discretisations, $n_{el} = \{1600, 3200\}$, even though not depicted here. Moreover, the computational speed in terms of the CPU-time T of both formulations is given in Table 5. It turns out that, for this particular example, the Q1Q1-element performs 3 to 4 times faster than the Q2Q1-formulation—a finer discretisation even increases this effect.

In summary, Q1Q1-elements seem to be able to reproduce the results obtained by the Q2Q1-formulation and—at the same time—are much more efficient from the computational point of view. Moreover, Q1Q1-elements are much easier to handle, e.g., with regard to contact problems. To give an example for constant pressure, the equivalent nodal force vectors associated with Q1Q1-elements all coincide. This is not the case for the Q2Q1-elements where the equivalent nodal force vectors at the middle and vertex nodes differ in magnitude and direction. This would considerably complicate the detection of contact conditions in Q2Q1-elements. In the following, however, we continue to use the Q2Q1-element-formulation as it increases the accuracy.

5.3. Test 3 – anisotropic plate with a hole

As a third numerical example, we consider an anisotropic version of the boundary value problem of the plate with a hole as discussed in the previous section. In particular, both families of fibers are oriented with respect to the axial $\boldsymbol{e}_Y$-direction, i.e., $\beta_{1,2} = 0.0$ deg where $\beta_{1,2} = \angle(\boldsymbol{a}_{0\,1,2}, \boldsymbol{e}_Y)$, together with $\boldsymbol{a}_{0\,1,2} \cdot \boldsymbol{e}_Z = 0$, and the dispersion parameter is set to $\varkappa = 0.0$ so that transverse anisotropy is recovered. This trivially ensures that both families of fibers are equally loaded, as the present formulation is restricted to *one* non-local damage variable for both fibre families undergoing identical degradation.

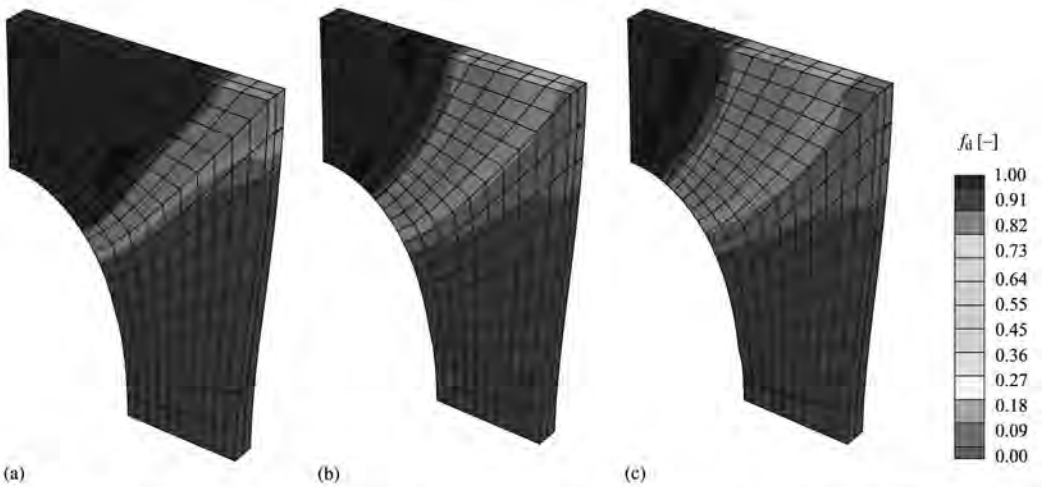

Fig. 8. Isotropic plate with a hole. Contour plots of the damage function $f_d(\kappa) \in (0, 1]$ at $u = 30$ mm and $c_d = 500$ kPa^{-1} for different values of the gradient parameter c_d using a 400 element mesh: (a) $c_d = 100$ kPa^{-1} mm^2, (b) $c_d = 500$ kPa^{-1} mm^2, (c) $c_d = 1000$ kPa^{-1} mm^2.

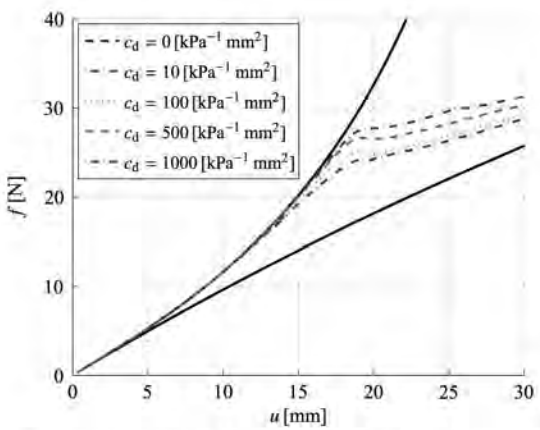

Fig. 9. Isotropic plate with a hole. Force–displacement response under monotonic loading for different values of the gradient parameter c_d using a 400 element mesh. The solid black curves represent the elastic response of the isotropic neo-Hookean matrix (lower solid black curve) and the overall elastic response composed of the isotropic neo-Hookean *and* the anisotropic exponential model (upper solid black curve).

Table 5
Isotropic plate with a hole. Comparison of the CPU times T for the element types Q2Q1 and Q1Q1 and different discretisations $n_{el} = \{400, 1600, 3200\}$.

n_{el}	T_{Q2Q1} (s)	T_{Q1Q1} (s)	T_{Q2Q1}/T_{Q1Q1}
400	811.00	270.31	3.00
1600	4542.20	1232.10	3.69
3200	13405.00	3293.60	4.07

Alternatively, a second non-local damage variable may be included in the formulation. The material parameters used for this example are summarised in Table 4 in column 'Test 3'.

5.3.1. Full isotropic contribution

The effect of the damage threshold κ_d is studied in Fig. 10 for the set of material parameters summarised in Table 4. In accordance with the results of the homogeneous uniaxial tension test presented in Fig. 5, damage initiation is delayed with increasing κ_d.

An even more important aspect with regard to this example is the emergence of the snap-back phenomena in the structural response of the anisotropic plate with a hole. An arc-length method is used to solve this boundary value problem; see

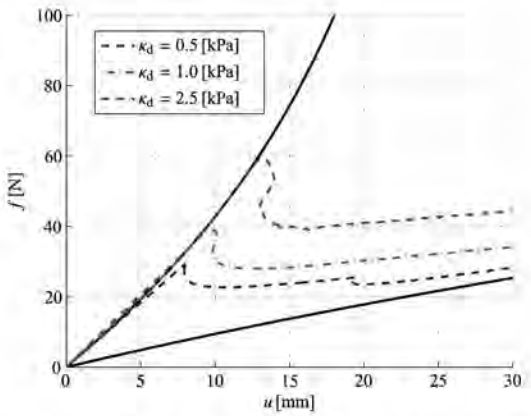

Fig. 10. Anisotropic plate with a hole. Force–displacement response under monotonic loading for different values of the damage threshold parameter κ_d using a 400 element mesh. The solid black curves represent the elastic response of the isotropic neo-Hookean matrix (lower solid black curve) and the overall elastic response composed of the isotropic neo-Hookean *and* the anisotropic exponential model (upper solid black curve).

Appendix D for a brief review of the arc-length method. Snap-back can be briefly described by taking into consideration that the elastic energy stored by the fibres prior to complete damage has to be released by either an inelastic dissipation process or by unloading of the structure. As stated before, the degree of dissipation is controlled by the parameter c_d. While keeping c_d constant, the only possibility to release elastic energy is unloading the structure which illustrates that snap-back is more prominent for higher values of κ_d. For more detailed background information on snap-back phenomena in structures failure, the reader is referred to, e.g., de Borst [20].

In Fig. 11, the contour of the damage function is plotted for different damage threshold values of κ_d. As expected, the damaged area decreases with increasing κ_d.

5.3.2. Reduced isotropic contribution

As indicated in Section 5.2, the contour plots of the damage function $f_d(\kappa)$ in Fig. 8 do not show strongly localised deformation patterns in the form of pronounced narrow damage bands. This is caused by the remaining stiffness of the undamaged isotropic matrix material. In order to show that a material with a smaller influence of the matrix material would considerably increase the effect of the damage evolution on the specimen, we reduce the elastic parameters governing the isotropic matrix material to $\mu_e = 0.1$ kPa and $\kappa_e = 1.0$ kPa, respectively, and furthermore set the damage threshold to $\kappa_d = 0.001$ kPa. The other (material) parameters remain unchanged according to Table 4.

The reduction of the elastic parameters μ_e and κ_e results in an almost negligible influence of the neo-Hookean ground substance and in an overall elastic mechanical response which is predominantly governed by the fibre-related anisotropic stress contribution, cf. the solid black curves in Fig. 12. We observe a strong influence of the regularisation parameter where values of $c_d = \{20, 50, 100, 200, 1000\}$ kPa^{-1} mm^2 are considered. For $c_d = \{20, 50, 100\}$ kPa^{-1} mm^2, we obtain a snap-back effect which necessitates the application of an arc-length solution scheme.

The contour-plots of the damage function $f_d(\kappa)$ in Fig. 13 illustrate the damage profile for $c_d = \{50, 100, 200, 1000\}$ kPa^{-1} mm^2. These are recorded at different stages of deformation marked by ①–④ in Fig. 12. We observe that higher values of c_d increase the localisation zone. In contrast to the previous examples, however, we obtain a much more pronounced localisation behaviour illustrated by the narrow damage bands, especially for $c_d = \{50, 100\}$ kPa^{-1} mm^2. This clearly underlines that a smaller influence of the matrix material considerably increases the effect of the damage localisation on the specimen.

5.4. Anisotropic artery-like tube

As a last example, we apply the gradient-enhanced damage formulation proposed to another three-dimensional inhomogeneous biomechanics-related boundary value problem. In particular, we focus on the finite element simulation of a two-layered fibre-reinforced artery-like tube subjected to internal pressure. This idealised setting is commonly used to assess basic capabilities of particular constitutive models for arteries, see e.g., Holzapfel et al. [37] for an analytical study or Alastrué et al. [9] for a similar finite-element-based investigation. Nevertheless, only very few contributions can be found in the literature which consider a *force-driven* large-deformation problem in connection with a gradient-enhanced damage model.

The particular geometry used in the present context is adopted from Alastrué et al. [9] and essentially reflects the geometry of a healthy coronary artery by means of a perfect cylindrical tube, see Fig. 14. The tube, characterised by the wall thickness $H = H^M + H^A$ and the inner Radius R_i of the segment, basically includes two main load-bearing layers, i.e., the media and adventitia, where we assume a wall-thickness ratio H^M/H^A of 3/2. The intima is not included in the model due to its negligible relevance for the mechanical behaviour of a young and healthy artery. The dimensions chosen for the tube are

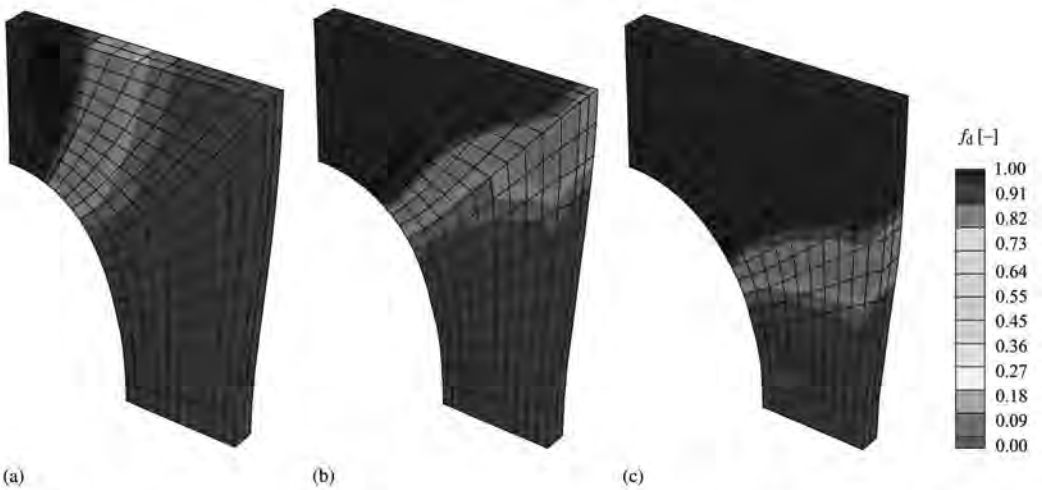

Fig. 11. Anisotropic plate with a hole. Contour plots of the damage function $f_d(\kappa) \in (0, 1]$ at $u = 30$ mm for different values of the damage threshold parameter κ_d using a 400 element mesh: (a) $\kappa_d = 0.5$ kPa, (b) $\kappa_d = 1.0$ kPa, (c) $\kappa_d = 2.5$ kPa.

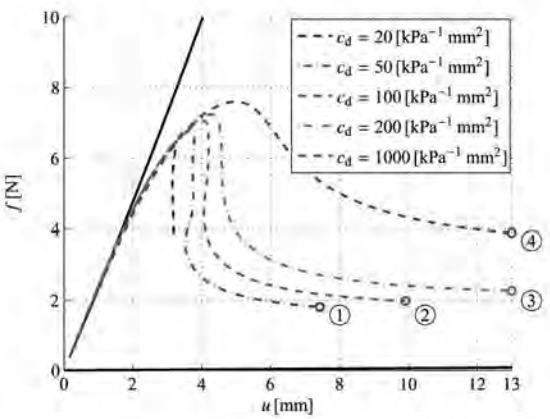

Fig. 12. Anisotropic plate with a hole with *reduced* isotropic contribution. Force–displacement response under monotonic loading for different values of the gradient parameter c_d using a 400 element mesh. The solid black curves represent the *reduced* elastic response of the isotropic neo-Hookean matrix (lower solid black curve) and the overall elastic response composed of the isotropic neo-Hookean and the anisotropic exponential model (upper solid black curve).

summarised in Table 6, whereupon a finite element mesh of 800 hexahedral elements according to Fig. 4, i.e., Q2Q1 elements are used, is created to model a cross-section of an artery-like tube, see Fig. 14(a).

Media and adventitia are characterised by individual material and structural parameters, see Table 6. The material parameters are taken from Holzapfel and Ogden [38, p. 55], where the shear modulus of the (compressible) neo-Hookean ground substance of the media is assumed to be ten times stiffer than the adventitia, i.e., $\mu_e^A = 10\,\mu_e^M$. To enforce nearly-incompressibility, the bulk moduli κ_e^M, κ_e^A are chosen to be 100 times larger than the respective shear moduli, i.e., $\kappa_e^M = 100\,\mu_e^M$ and $\kappa_e^A = 100\,\mu_e^A$. In this regard, we recall that we do not apply a quasi-incompressible neo-Hookean format based on an isochoric-volumetric split.

The structural parameters are taken from Alastrué et al. [9] and summarised in Table 6. The number of mechanically equivalent fibre families per layer is restricted to $N = 2$ and, moreover, their initial orientations are assumed as $\boldsymbol{a}_{01,2}^n = \sin(\beta^n)\,\boldsymbol{e}_Z \pm \cos(\beta^n)\,\boldsymbol{e}_\Theta$ with n = M for the media and n = A for the adventitia. In this regard, the layer-specific mean fibre orientation angles β^M and β^A are specified at the integration point level of each finite element so that a helical fibre distribution is included in the model, see Fig. 14(b). Due to the symmetry of the geometry, the symmetry of the fibre orientations as well as the internal pressure loading, both fibre families are equally loaded, so that $E = E_1 = E_2$. Consequently, both fibre families are exposed to identical degradation. This justifies the use of only *one* non-local damage variable for both fibre families.

Furthermore, small dispersions of the fibres are considered, i.e., $\varkappa^n \neq 0$. In [9], layer-specific values for the related concentration parameter b are provided and can be converted to the dispersion parameter $\varkappa$ as introduced in Eq. (47) by means of

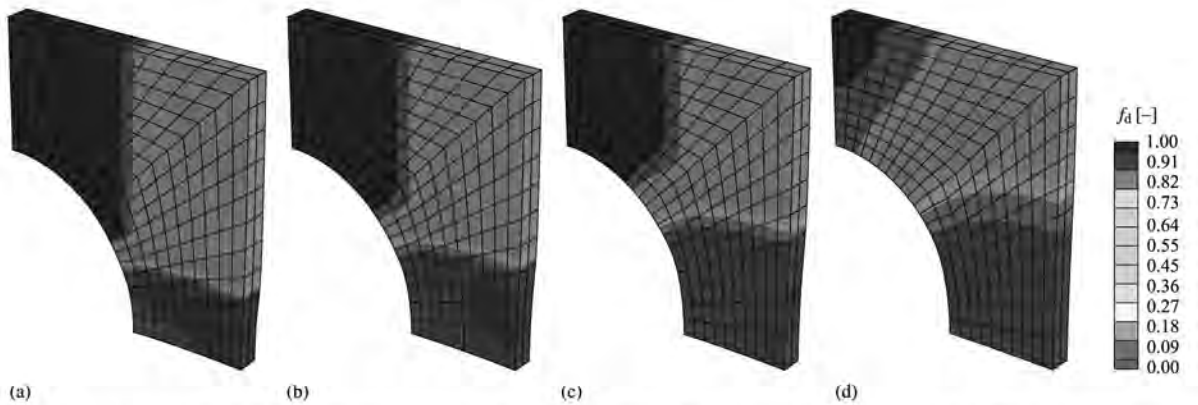

Fig. 13. Anisotropic plate with a hole with *reduced* isotropic contribution. Contour plots of the damage function $f_d(\kappa) \in (0, 1]$ at different deformation stages ①–④, cf. Fig. 12, for different values of the gradient parameter c_d using a 400 element mesh. (a) $c_d = 50\ \text{kPa}^{-1}\,\text{mm}^2$ at ①, (b) $c_d = 100\ \text{kPa}^{-1}\,\text{mm}^2$ at ②, (c) $c_d = 200\ \text{kPa}^{-1}\,\text{mm}^2$ at ③, (d) $c_d = 1000\ \text{kPa}^{-1}\,\text{mm}^2$ at ④.

$$\varkappa^{\mathrm{n}} = \frac{1}{4}\int_0^{\pi} \rho^{\mathrm{n}}(\vartheta^{\mathrm{n}})\sin^3(\vartheta^{\mathrm{n}})\,\mathrm{d}\vartheta^{\mathrm{n}} \tag{113}$$

with the π-periodic normalised von Mises density function

$$\rho^{\mathrm{n}}(\vartheta) = 4\sqrt{\frac{b^{\mathrm{n}}}{2\pi}}\frac{\exp(b^{\mathrm{n}}[\cos(2\,\vartheta^{\mathrm{n}})+1])}{\operatorname{erfi}(\sqrt{2\,b^{\mathrm{n}}})}. \tag{114}$$

Herein, $\vartheta^{\mathrm{n}} \in [0, \pi]$ denotes a 'dispersion angle' characterising the rotational symmetric distribution of a given fibre family with respect to the mean referential preferred fibre direction $\boldsymbol{a}_{0i}^{\mathrm{n}}$. Furthermore, the concentration parameter $b > 0$ represents a measure of the degree of anisotropy and $\operatorname{erfi}(x) = i\operatorname{erf}(x)$ denotes the imaginary error function which, according to Weisstein [98], can conveniently be approximated numerically by a series expansion; see e.g., Alastrué et al. [9] for further details. Relation (113) can be evaluated either by numerical integration, see Gasser et al. [35], or by using a polynomial representation as applied in Menzel et al. [60]. For the media, we obtain $\varkappa^{\mathrm{M}} = 0.19$, which indicates a dispersed character of the fibres. In the adventitia, value $\varkappa^{\mathrm{A}} = 0.036$ is very close to zero, reflecting an almost transversely isotropic state for each fibre family which is in line with the recent experimental results reported by Schriefl et al. [83].

Note, that residual stresses are neglected at this stage, even though they are essential for the mechanical response of arteries, see Holzapfel et al. [37]. However, to emphasise the effects due to the damage, we do not incorporate them in the present work. For cylindrical geometries, residual stretches can directly be included in the finite element setting

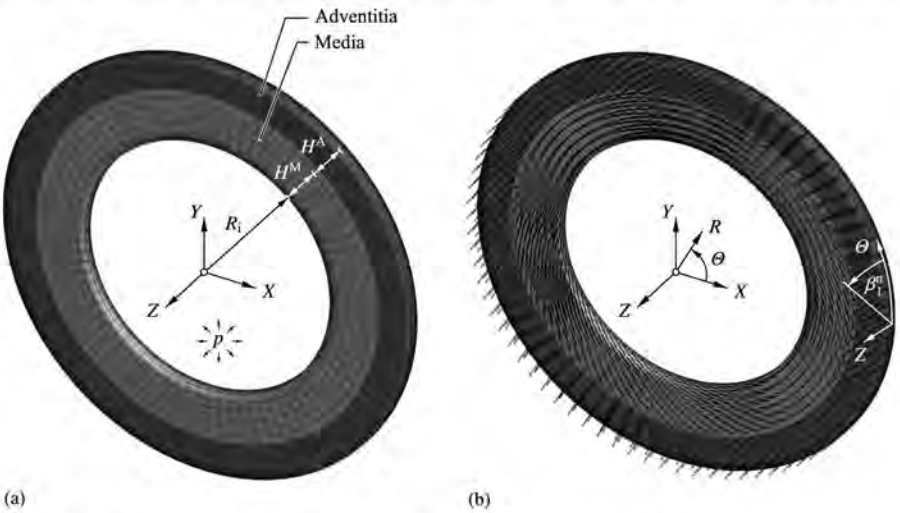

Fig. 14. Geometry of the thick-walled two-layered cylindrical tube. (a) Finite element mesh with applied internal pressure p and fixed displacements in circumferential and longitudinal direction (not displayed) and (b) fibre orientations for the media and adventitia. The fibre orientation angles β^{n} are introduced with respect to the circumferential direction Θ.

Table 6
Set of geometrical, structural and material parameters as used for the artery-like tube (n = M for the media and n = A for the adventitia). The material parameters are subdivided in elastic- and damage-related parameters. The geometrical and structural parameters are adopted from Alastrué et al. [9], the elastic parameters from Holzapfel and Ogden [38].

Type	Symbol	Value		Unit
		Media	Adventitia	
Geometrical	R_i^n	1.35	1.89	mm
	H^n	0.54	0.36	mm
Structural	β^n	21.700	62.260	deg
	$\varkappa^n$	0.19	0.036	-
Elastic	μ_e^n	27.0	2.7	kPa
	κ_e^n	2700.0	270.0	kPa
	k_1^n	0.64	5.1	kPa
	k_2^n	3.54	15.4	-
Regularisation	c_d	0.01		$\text{kPa}^{-1}\,\text{mm}^2$
	β_d	1000.0		kPa^{-1}
	γ_d	1.0		-
Damage	η_d	0.1		kPa^{-1}
	κ_d	3.0		kPa

following, e.g., the strategies proposed by Alastrué et al. [10] or Alastrué et al. [9] which are based on a multiplicative composition of the deformation gradient.

With regard to boundary conditions, the displacements in circumferential and longitudinal direction are prescribed to zero at the front and back face of the arterial segment, i.e., $u_\theta = u_z = 0.0$ at related nodes. The non-local damage-related field variable ϕ is initialised as the value of the damage threshold κ_d, i.e., $\phi|_{t_0} = \kappa_d$. Furthermore, we apply a pressure p at the inner radius of the specimen. This pressure, however, is not prescribed explicitly—typically by a value of $p = 100$ mmHg $= 13.33$ kPa representing the mean physiological blood pressure—but is part of the solution itself, the reason being that an arc-length method is applied which enables tracing of the post-peak branch of the load–displacement curves in the damage regime. This proves to be a very advantageous and robust procedure to obtain static equilibrium states for snap-back response or force-driven degradation as discussed here. As the loading magnitude itself is part of the solution, the arc-length algorithm cannot produce a solution at given load or displacement values directly, as they are treated as unknowns. This complicates a performance of a cyclic force-driven deformation test. Instead, as a termination criterion, the simulation is completed as soon as a prescribed maximum displacement value $u_{\max}$ at a specified degree of freedom is exceeded—here the radial displacement $u_r(r_i)$ at a node located at the inner radius r_i of the tube. In the following, this termination value is set to $u_{\max} = 1.5$ mm. A brief review on the arc-length method in the context of the Abaqus-related UEL-implementation is provided in Appendices B and D.

Fig. 15 depicts the load–displacement-response of the inflated tube where the pressure p is plotted over the displacement $u_r(r_i)$ at the inner radius of the tube. The lower solid black curve represents the purely elastic mechanical behaviour due to the isotropic neo-Hookean ground substance, see Eq. (44). The upper solid black curve shows the overall elastic response based on the isotropic neo-Hookean part (44) as well as the predominant anisotropic exponential contribution (47). Both curves give a good illustration of the highly non-linear material behaviour especially at large strains. The blue curve shows the mechanical response due to the damage of the fibre contributions. We observe that within the physiological pressure range—determined by the diastolic blood pressure $p = 8.0$ kPa and the systolic blood pressure $p = 17.4$ kPa—the material responds according to the elastic load path. However, from a pressure value of approx. $p = 20.0$ kPa upwards, the material softens significantly and increasingly deviates from the elastic path. The maximal pressure $p_{\max} = 48.521$ kPa is obtained at $u_r = 1.305$ mm. After that state—caused by the substantial loss of stiffness—the pressure starts to decrease while the displacement still increases and the curve finally drops towards the elastic response of the undamaged neo-Hookean ground substance. Physically, this can be interpreted as a continuous degradation of the fibres contained in an undamaged matrix material, which consequently is expected to carry the full load after complete loss of fibre stiffness.

It becomes apparent that the damage evolution beyond the physiological range results in an increase of the diameter—here measured by the radial displacement u_r—of the tube at the same (mean) pressure. Consequently, at the expense of a loss in stiffness, these damage effects can be beneficially exploited in order to expand an artery and thereby restore and ensure the blood flow of an atherosclerotic or arteriosclerotic blood vessel for instance. One prominent application example from the surgical point of view, which benefits from these effects, is the *balloon angioplasty* where an elastic balloon is inserted and inflated inside the constricted artery; see e.g., Holzapfel et al. [40], Gasser and Holzapfel [34] or Alastrué et al. [11] for detailed studies including experiments and finite element simulations.

It is important to mention that the assumption of an intact matrix and two equally damaging fibre families can provide only a very simplified description of the real biomechanical effects. As a possible refinement or extension of the model, one

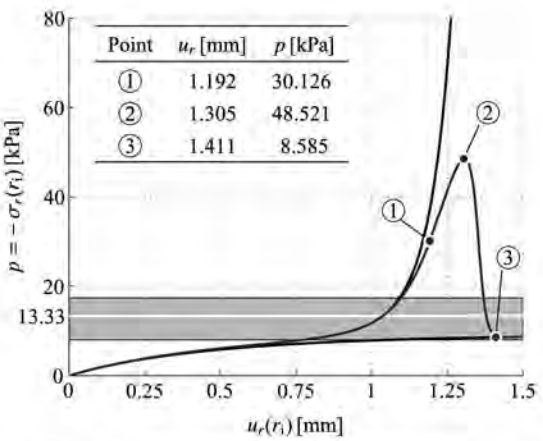

Fig. 15. Load–displacement-response for the inflated tube: pressure p versus displacement $u_r(r_i)$ at the inner radius of the tube. The lower solid black curve represents the elastic isotropic neo-Hookean ground substance, the upper solid black curve shows the elastic anisotropic fibre-related contribution according to Gasser et al. [35], the blue curve shows the mechanical response due to the gradient-enhanced damage. The gray-shaded region represents the physiological pressure range, determined by the diastolic blood pressure $p = 8.0$ kPa (lower black line), the systolic blood pressure $p = 17.4$ kPa (upper black line) and the mean blood pressure $p = 13.33$ kPa (white line).

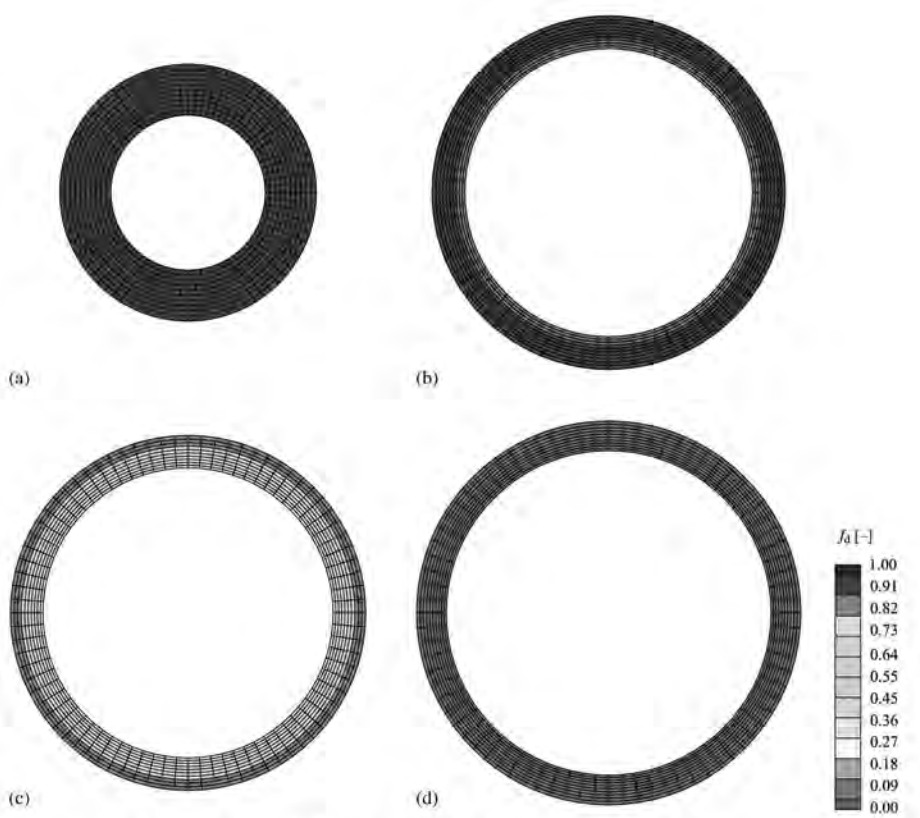

Fig. 16. Artery-like tube subjected to internal pressure. Contour plot of the distribution of the damage function $f_d(\kappa) \in (0,1]$ at (a) the referential (undamaged) state and at (b)–(d) representative (damaged) states ①–③, as specified in Fig. 15, cf. Fig. 17(b) for an alternative representation.

could, for instance, apply two independent damage variables for matrix and fibres, as proposed in Calvo et al. [22] for the purely local case, or even three independent damage variables, including matrix-damage and individual damage for each fibre family. In view of a related finite element implementation, however, this would require three individual non-local damage fields in the latter case, possibly accompanied by an active-set search in order to identify the currently damaged

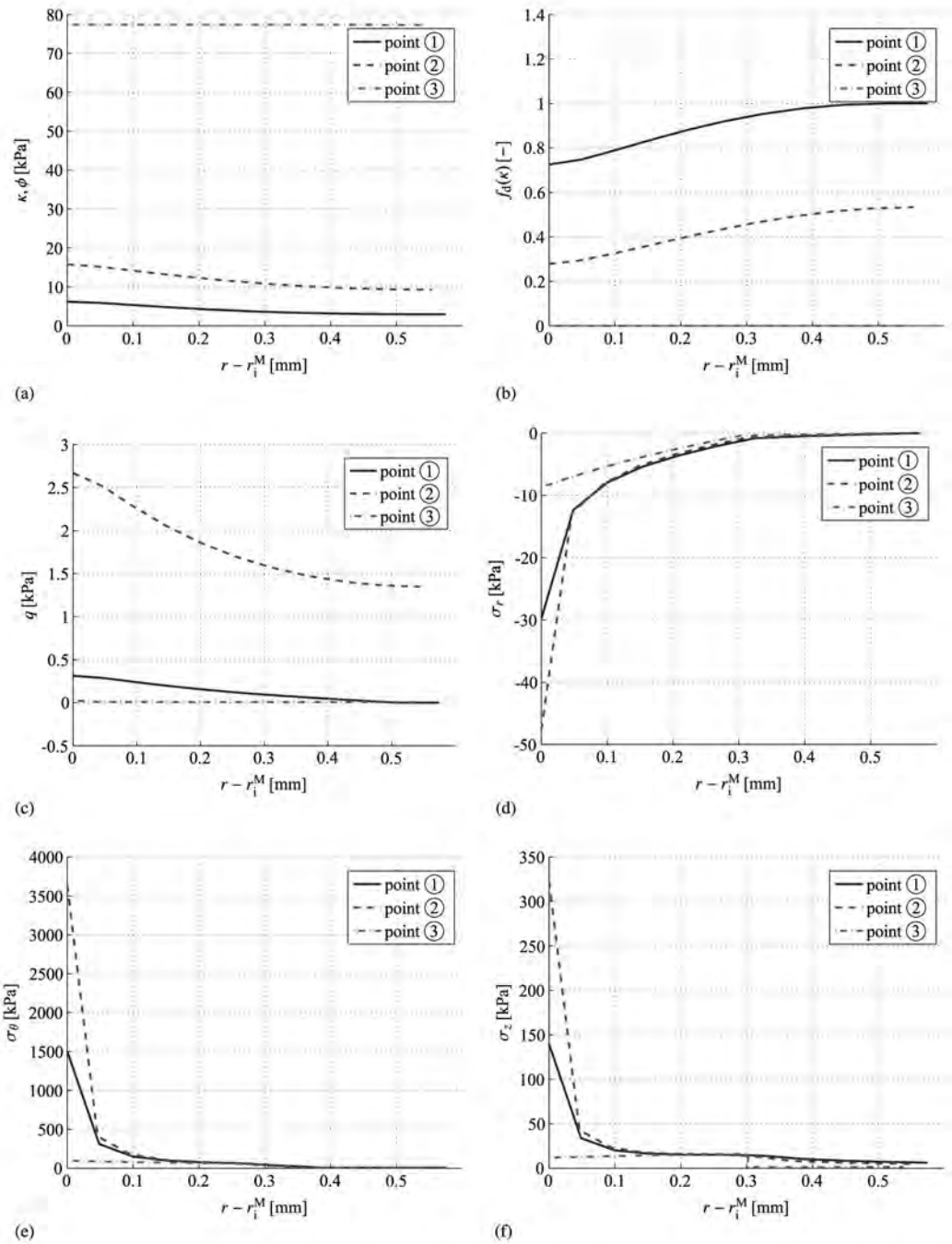

Fig. 17. Artery-like tube. Distribution of damage-related parameters and the principal Cauchy stresses over the current width $r - r_i^M$ of the tube for representative loading points ①–③, as specified in Fig. 15. (a) (Non-)local damage variable κ and ϕ, (b) damage function $f_d(\kappa) \in (0, 1]$, (c) driving force q, (d) radial stress σ_r, (e) circumferential stress σ_θ, (f) axial stress σ_z.

fibre family of the multi-surface damage problem, see Dimitrijević and Hackl [29] for a regularisation framework for multi-surface damage-plasticity models.

Fig. 16 depicts contour-plots of the distribution of the damage function $f_d(\kappa) \in (0, 1]$ at the referential (undamaged) setting $\mathcal{B}_0$ and at three representative loading points ①–③, as specified in Fig. 15. In particular, we consider point ① with $u_r = 1.192$ mm and $p = 30.126$ kPa located close to the state of damage initiation, point ② at the maximal peak pressure $p_{max} = 48.521$ kPa with $u_r = 1.305$ mm and ③ at the fully damaged state in the post-peak branch with $u_r = 1.411$ mm and $p = 8.585$ kPa.

As expected, the distribution of the damage function in the undamaged reference state is homogeneous, with $f_d(\kappa) = 1.0$, and in the fully damaged configuration ③ with $f_d(\kappa) \to 0.0$. At loading points ① and ②, however, we observe a heterogeneous distribution of $f_d(\kappa)$ where higher damage values are obtained at the inner wall of the tube.

Due to the symmetry of the problem and in order to obtain a better quantitative view of the damage profile over the wall-thickness, it turns out to be appropriate to investigate the distribution of damage-related parameters and stresses over the current width $r - r_i^M$ of the tube recorded at the nodes across the wall-thickness. Once more, we consider three representative loading points ①–③, which, in Fig. 17, correspond to the red, green and blue curves, respectively.

Fig. 17 shows the distribution of (a) the damage parameters κ and ϕ, (b) the damage function $f_d(\kappa)$ and (c) the driving force q over the current width $r - r_i^M$ of the tube at the aforementioned representative points of the loading path. From Fig. 17(b), we observe successively increasing damage parameters κ and ϕ for points ①–③, which for ① and ② take their maximum values at the inner wall of the tube and show a decreasing tendency towards the outer radius. For the fully damaged point ③, we obtain an almost constant distribution of the damage variable over the wall-thickness. This corresponds to the curves in Fig. 17(b), which represent the state of damage by means of the damage function $f_d(\kappa)$, see Eq. (70), where $f_d = 1.0$ for the intact and $f_d \to 0.0$ for the fully damaged case. At point ① the inner wall is apparently already damaged, whereas the outer radius of the wall is still intact. At point ②, we obtain a similar damage characteristic, now distributed over the wall-thickness until, finally, at point ③ the fibre contributions over the whole wall are fully damaged. The driving force q is depicted in Fig. 17(c). In agreement with the preceding results, we observe its maximal values at the inner wall of the tube. The maximal overall distribution is obtained at point ② associated with the maximal pressure p_{max}.

Furthermore, Fig. 17 shows the (d) radial, (e) circumferential and (f) axial Cauchy stress distributions over the current width $r - r_i^M$ of the tube at the aforementioned representative points of the loading. We observe that the circumferential stress σ_ϑ is the dominant stress component within the wall, since its magnitude is significantly larger compared to the magnitudes of σ_r and σ_z. Note, that the longitudinal stretch is constrained by the boundary condition chosen so that $\lambda_z = 1$. As expected from the load–displacement curve in Fig. 15, the maximal stresses are obtained for the maximal pressure p_{max} associated with point ②. For all loading points considered, stress peaks typically occur at the inner wall boundary. Due to the damage evolution, these peaks are significantly reduced which is a consequence of the loss of stiffness of the fibres.

6. Summary

A well-known problem related to *local* continuum damage formulations is the loss of well-posedness in the context of local loss of ellipticity of the underlying boundary value problem. As a consequence, finite element-based simulations turn out—if obtained at all—to significantly depend on the particular discretisation. Typically, this is indicated by a narrow localised damage zone, which is only constrained by the mesh resolution.

One possible strategy to overcome this deficiency, i.e., to regularise the problem, would be the use of non-local continuum formulations. In the present contribution, a non-local gradient-enhanced damage model is developed within a geometrically non-linear setting. The implicit regularisation of the problem is achieved by enhancement of the local free energy with gradient contributions of the non-local damage variable. Equivalence between the local and non-local damage field variable is ensured by a penalisation term incorporated within the free energy function. Based on the principle of minimum total potential energy, a coupled system of Euler–Lagrange equations has to be solved in weak form in order to simulate general boundary value problems. The local elastic constitutive response is represented by a hyperelastic format, additively composed of an isotropic and an anisotropic part. The inelastic constitutive response is assumed to be governed by a scalar $[1-d]$-type damage approach, affecting the anisotropic elastic part only.

Apart from discussing the local damage model under homogeneous deformations, we investigate the regularisation capabilities of the formulation by means of a three-dimensional numerical example of an isotropic and anisotropic plate with a hole subjected to displacement-driven loading. With regard to the isotropic plate, the assumption of 'intact matrix' and 'damaged fibres' is underlined by the load–displacement-path which clearly tends towards the purely neo-Hookean response. Furthermore, the dissipative character of the damage formulation is highlighted by the cyclic tension test. Finally, the simulation results clearly illustrate the desired regularisation effect and identify the mesh-objectivity by comparing three different discretisations. Regarding the simulation of the anisotropic plate—enabled by using an arc-length-based solution method—a significant structural *snap-back*-behaviour is obtained. This effect is characteristic for damage-related softening processes and obviously a consequence of the assumption of transverse isotropy within the plate. With regard to the applied element-formulation, Q1Q1-elements turn out to be able to reproduce the results obtained by the Q2Q1-formulation, which is usually used for gradient-enhanced damage models. At the same time the Q1Q1-elements are more efficient from the computational point of view and easier to handle, for instance with regard to contact problems. Both aspects underline the applicability of the proposed approach to more complex boundary value problems, e.g., with regard to patient-specific biomechanical applications.

In this contribution, however, we restrict ourselves to present a biomechanics-related model problem, i.e., the simulation of a thick-walled two-layered artery-like tube subjected to internal pressure. The highly non-linear elastic behaviour of the material is well reflected by the mechanical response of the tube within the physiological pressure range. For higher pressure values the material softens significantly, increasingly deviates from the elastic path and finally drops towards the elastic response of the undamaged neo-Hookean ground substance. Physically, this can be suitably interpreted as a continuous degradation of the fibres contained in an undamaged matrix material. It becomes apparent that the damage evolution

beyond the physiological range results in an increase of the tube's diameter at the same mean pressure. Consequently, at the expense of a loss in stiffness, these damage effects can be beneficially used in medical surgery to expand an artery's diameter and thereby restore and ensure the blood flow of an atherosclerotic or arteriosclerotic blood vessel for example.

It is important to mention that the assumption of an intact matrix and two equally damaging fibre families can provide only a very simplified description of the real (bio)mechanical effects. As a possible extension of the model one could, for instance, apply two independent damage variables for matrix and fibres, as proposed in Calvo et al. [22] for the purely local case, or even three independent damage variables, including matrix-damage and individual damage for each fibre family. In view of a related finite element implementation, however, this would require three individual non-local damage fields in the latter case, possibly accompanied by an active-set search in order to identify the currently damaged fibre family of the multi-surface damage problem, see Dimitrijević and Hackl [29] for a regularisation framework for multi-surface damage-plasticity models.

The present gradient-enhanced damage approach proves to be quite robust, even at stages of pronounced softening, and allows the incorporation of practically any suitable *scalar-valued* damage formulation, provided that the damage function decreases faster than the respective stress measure increases with deformation. Nevertheless, a further extension to corresponding *tensor-valued* damage approaches, with special regard to anisotropic damage formulation, is desirable.

With regard to the non-linear elastic material behaviour, we recall that we do not apply a quasi-incompressible neo-Hookean format based on an isochoric-volumetric split, as it is typically done in related articles, see Holzapfel et al. [37] amongst others. From the computational point of view, a mixed or hybrid element formulation should be considered to account for the incompressibility-constraint; see, e.g., the recent work by Welschinger [99], who proposed an appropriate approach to avoid these problems within a gradient-extended continuum formulation, or Ask et al. [12], where an incompressibility constraint is considered in addition to the underlying coupled problem. In order to avoid numerical inconsistencies such as locking phenomena, an $\bar{\boldsymbol{F}}$-approach could also be adopted for the Q1Q1-element with eight integration points. As a further possibility to reduce the CPU-time, one could establish a Q1Q1-element with one integration point and hourglass control of both global field variables.

As a long-term goal it is desired to apply the proposed formulation to a more realistic or even patient-specific simulation setting, e.g., with regard to surgical activities such as balloon angioplasty. Furthermore, the comparison and identification of simulated failure and damage properties with related experimental data will be of high interest, especially regarding an appropriate calibration of the gradient parameter c_{d} for specific boundary value problems; see Mahnken and Kuhl [56]. In addition, the incorporation of residual stresses for applications based on the gradient-enhanced damage model is of key importance.

Acknowledgements

T.W. would like to thank Björn Kiefer and Ralf Denzer for many helpful discussions. C.P. acknowledges the funding received from the Spanish Ministry of Science and Innovation through the research project DPI-2008-03130/DPI.

Appendix A. Local tangent moduli

The local tangent moduli, contained in the element Jacobians (106)–(109), can conveniently be derived in material description and then transferred to the spatial description as used for the numerical implementation, by means of push-forward operations. In the following, we omit the subscript index $n+1$ associated with time t_{n+1} for the sake of readability.

For the particular model at hand, the contributions to the Piola–Kirchhoff stresses are given as

$$\boldsymbol{S}^{\mathrm{iso}} = \mu_{\mathrm{e}} [\boldsymbol{I} - \boldsymbol{C}^{-1}] + \lambda_{\mathrm{e}} \ln(J) \boldsymbol{C}^{-1}, \tag{A.1}$$

$$\boldsymbol{S}^{\mathrm{ani}} = 2 k_1 \sum_{i=1}^{N} \left[E_i \exp\left(k_2 \langle E_i \rangle^2 \right) \boldsymbol{H}_i \right], \tag{A.2}$$

where the material version of the generalised structural tensor $\boldsymbol{H}_i = \varkappa \boldsymbol{I} + [1 - 3\varkappa] \boldsymbol{a}_{0i} \otimes \boldsymbol{a}_{0i}$ is used. By means of the chain rule together with the definitions $\mathbf{E}^{\mathrm{iso}} := 2 \partial \boldsymbol{S}^{\mathrm{iso}} / \partial \boldsymbol{C}$ and $\mathbf{E}^{\mathrm{ani}} := 2 \partial \boldsymbol{S}^{\mathrm{ani}} / \partial \boldsymbol{C}$, we obtain

$$\mathbf{E} := 2 \frac{\mathrm{d}\boldsymbol{S}}{\mathrm{d}\boldsymbol{C}} = \mathbf{E}^{\mathrm{iso}} + f_{\mathrm{d}} \mathbf{E}^{\mathrm{ani}} + 2 \boldsymbol{S}^{\mathrm{ani}} \otimes \frac{\partial f_{\mathrm{d}}}{\partial \kappa} \frac{\partial \kappa}{\partial \boldsymbol{C}}, \tag{A.3}$$

$$\frac{\mathrm{d}\boldsymbol{S}}{\mathrm{d}\phi} = \frac{\partial f_{\mathrm{d}}}{\partial \kappa} \frac{\partial \kappa}{\partial \phi} \boldsymbol{S}^{\mathrm{ani}}, \tag{A.4}$$

$$2 \frac{\mathrm{d}Y}{\mathrm{d}\boldsymbol{C}} = 2 \frac{\partial Y}{\partial \kappa} \frac{\partial \kappa}{\partial \boldsymbol{C}}; \tag{A.5}$$

$$\frac{\mathrm{d}Y}{\mathrm{d}\phi} = \frac{\partial Y}{\partial \phi} + \frac{\partial Y}{\partial \kappa} \frac{\partial \kappa}{\partial \phi}. \tag{A.6}$$

with

$$\mathbf{E}^{\mathrm{iso}} = \lambda_{\mathrm{e}}\, \boldsymbol{C}^{-1} \otimes \boldsymbol{C}^{-1} + 2\left[\mu_{\mathrm{e}} - \lambda_{\mathrm{e}} \ln(J)\right] \mathbf{I}^{\mathrm{sym}}_{\boldsymbol{C}^{-1}}, \tag{A.7}$$

$$\mathbf{E}^{\mathrm{ani}} = 4 k_1 \sum_{i=1}^{N} \left[\exp\left(k_2 \langle E_i \rangle^2\right)\left[1 + 2 k_2 \langle E_i \rangle^2\right] \boldsymbol{H}_i \otimes \boldsymbol{H}_i\right]. \tag{A.8}$$

Here, the definition of the fourth order tensor $\mathbf{I}^{\mathrm{sym}}_{\boldsymbol{C}^{-1}} := -\partial \boldsymbol{C}^{-1}/\partial \boldsymbol{C} = [\boldsymbol{C}^{-1} \overline{\otimes} \boldsymbol{C}^{-1} + \boldsymbol{C}^{-1} \underline{\otimes} \boldsymbol{C}^{-1}]/2$ is used, with the non-standard dyadic products defined as $[\boldsymbol{T}_1 \overline{\otimes} \boldsymbol{T}_2] : \boldsymbol{T}_3 = \boldsymbol{T}_1 \cdot \boldsymbol{T}_3 \cdot \boldsymbol{T}_2^{\mathrm{t}}$ and $[\boldsymbol{T}_1 \underline{\otimes} \boldsymbol{T}_2] : \boldsymbol{T}_3 = \boldsymbol{T}_1 \cdot \boldsymbol{T}_3^{\mathrm{t}} \cdot \boldsymbol{T}_2^{\mathrm{t}}$ for any second-order tensors $\boldsymbol{T}_{1,2,3}$.

The remaining task is to determine the derivatives, on the right hand sides of Eqs. (A.3)–(A.6) as well as $\mathrm{d}\boldsymbol{Y}/\mathrm{d}\nabla_{\boldsymbol{x}}\phi$. We subsequently specify these expressions consecutively according to their appearance in the above mentioned equations.

Recalling that $\Phi_{\mathrm{d}}(q, \kappa) = 0$ for damage evolution, the tensorial derivative $\partial\kappa/\partial\boldsymbol{C}$ and $\partial\kappa/\partial\phi$ are deduced by means of the implicit function theorem as

$$2\,\frac{\partial \kappa}{\partial \boldsymbol{C}} = -2\,\frac{\partial \Phi_{\mathrm{d}}/\partial \boldsymbol{C}}{\partial \Phi_{\mathrm{d}}/\partial \kappa} = -\vartheta_{\mathrm{d}}\, \boldsymbol{S}^{\mathrm{ani}}, \tag{A.9}$$

$$\frac{\partial \kappa}{\partial \phi} = -\frac{\partial \Phi_{\mathrm{d}}/\partial \phi}{\partial \Phi_{\mathrm{d}}/\partial \kappa} = -\vartheta_{\mathrm{d}}\, \frac{\beta_{\mathrm{d}}\, \gamma_{\mathrm{d}}}{\eta_{\mathrm{d}} f_{\mathrm{d}}}, \tag{A.10}$$

where the abbreviation

$$\vartheta_{\mathrm{d}} := \left[\frac{\partial \Phi_{\mathrm{d}}}{\partial \kappa}\right]^{-1} = -1 - \frac{\eta_{\mathrm{d}} f_{\mathrm{d}}}{\beta_{\mathrm{d}}\, \gamma_{\mathrm{d}}\left[\gamma_{\mathrm{d}}[1 + \eta_{\mathrm{d}}\, \kappa] - \eta_{\mathrm{d}}\, \phi\right]} \tag{A.11}$$

is introduced. Taking into account that $\partial_\kappa f_{\mathrm{d}} = -\eta_{\mathrm{d}} f_{\mathrm{d}}$ and $\partial_\kappa Y = -\beta_{\mathrm{d}}\, \gamma_{\mathrm{d}}$ as well as $\partial_\phi Y = \beta_{\mathrm{d}}$, we obtain the material tangent moduli as

$$\mathbf{E} = \mathbf{E}^{\mathrm{iso}} + f_{\mathrm{d}}\, \mathbf{E}^{\mathrm{ani}} + \eta_{\mathrm{d}} f_{\mathrm{d}}\, \vartheta_{\mathrm{d}}\, \boldsymbol{S}^{\mathrm{ani}} \otimes \boldsymbol{S}^{\mathrm{ani}}, \tag{A.12}$$

$$\frac{\mathrm{d}\boldsymbol{S}}{\mathrm{d}\phi} = \beta_{\mathrm{d}}\, \gamma_{\mathrm{d}}\, \vartheta_{\mathrm{d}}\, \boldsymbol{S}^{\mathrm{ani}}, \tag{A.13}$$

$$2\,\frac{\mathrm{d}Y}{\mathrm{d}\boldsymbol{C}} = \beta_{\mathrm{d}}\, \gamma_{\mathrm{d}}\, \vartheta_{\mathrm{d}}\, \boldsymbol{S}^{\mathrm{ani}}, \tag{A.14}$$

$$\frac{\mathrm{d}Y}{\mathrm{d}\phi} = \beta_{\mathrm{d}} + [\beta_{\mathrm{d}}\, \gamma_{\mathrm{d}}]^2 [\eta_{\mathrm{d}} f_{\mathrm{d}}]^{-1} \vartheta_{\mathrm{d}}, \tag{A.15}$$

$$\frac{\mathrm{d}Y}{\mathrm{d}\nabla_{\boldsymbol{x}}\phi} = \mathrm{c}_{\mathrm{d}}\, \boldsymbol{C}^{-1}. \tag{A.16}$$

For a purely elastic loading step, the tangent moduli can be reduced to $\mathbf{E} = \mathbf{E}^{\mathrm{iso}} + f_{\mathrm{d}}\, \mathbf{E}^{\mathrm{ani}}$ and $\mathrm{d}\boldsymbol{S}/\mathrm{d}\phi = 2\,\mathrm{d}Y/\mathrm{d}\boldsymbol{C} = \boldsymbol{0}$ as well as $\mathrm{d}Y/\mathrm{d}\phi = \beta_{\mathrm{d}}$.

Applying push-forward operations to Eqs. (A.12)–(A.16), we finally obtain the Cauchy-stress-related spatial tangent moduli as

$$\mathbf{e} = 2\,\frac{\mathrm{d}\boldsymbol{\sigma}}{\mathrm{d}\mathbf{g}} = \mathbf{e}^{\mathrm{iso}} + f_{\mathrm{d}}\, \mathbf{e}^{\mathrm{ani}} + \eta_{\mathrm{d}} f_{\mathrm{d}}\, \vartheta_{\mathrm{d}} J\, \boldsymbol{\sigma}^{\mathrm{ani}} \otimes \boldsymbol{\sigma}^{\mathrm{ani}}, \tag{A.17}$$

$$\frac{\mathrm{d}\boldsymbol{\sigma}}{\mathrm{d}\phi} = \beta_{\mathrm{d}}\, \gamma_{\mathrm{d}}\, \vartheta_{\mathrm{d}}\, \boldsymbol{\sigma}^{\mathrm{ani}}, \tag{A.18}$$

$$2\,\frac{\mathrm{d}\mathrm{y}}{\mathrm{d}\mathbf{g}} = \beta_{\mathrm{d}}\, \gamma_{\mathrm{d}}\, \vartheta_{\mathrm{d}}\, \boldsymbol{\sigma}^{\mathrm{ani}}, \tag{A.19}$$

$$\frac{\mathrm{d}\mathrm{y}}{\mathrm{d}\phi} = J^{-1} \beta_{\mathrm{d}} \left[1 + \beta_{\mathrm{d}}\, \gamma_{\mathrm{d}}^2 [\eta_{\mathrm{d}} f_{\mathrm{d}}]^{-1} \vartheta_{\mathrm{d}}\right], \tag{A.20}$$

$$\frac{\mathrm{d}\boldsymbol{y}}{\mathrm{d}\nabla_{\boldsymbol{x}}\phi} = J^{-1}\, \mathrm{c}_{\mathrm{d}}\, \boldsymbol{I}. \tag{A.21}$$

Note the relation $\partial_{\boldsymbol{g}}(\bullet) := \boldsymbol{F} \cdot \partial_{\boldsymbol{C}}(\bullet) \cdot \boldsymbol{F}^{\mathrm{t}}$; for detailed background on the formulation of anisotropic finite elasticity and inelasticity in terms of spatial arguments, the reader is referred to Menzel and Steinmann [62,63]. The isotropic and anisotropic elasticity tensors in spatial description can be expressed as

$$\mathbf{e}^{\mathrm{iso}} = \lambda_e J^{-1} \boldsymbol{I} \otimes \boldsymbol{I} + 2J^{-1}[\mu_e - \lambda_e \ln(J)]\,\mathbf{I}^{\mathrm{sym}}, \tag{A.22}$$

$$\mathbf{e}^{\mathrm{ani}} = 4k_1 J^{-1} \sum_{i=1}^{N} \left[\exp\left(k_2 \langle E_i \rangle^2\right) \left[1 + 2k_2 \langle E_i \rangle^2\right] \boldsymbol{h}_i \otimes \boldsymbol{h}_i \right], \tag{A.23}$$

where the definition of the fourth order symmetric identity tensor $\mathbf{I}^{\mathrm{sym}} = [\boldsymbol{I} \overline{\otimes} \boldsymbol{I} + \boldsymbol{I} \underline{\otimes} \boldsymbol{I}]/2$ is used.

Appendix B. Implementation of element-formulations using the Abaqus subroutine UEL

The non-linear coupled finite-element-formulation outlined in Section 4 can be implemented in the commercial finite-element-software Abaqus via so-called *user subroutines*, for a general overview, see Abaqus Analysis User's Manual [2, ch. 17.1.1]. This section is intended to provide a brief review on aspects of implementation in the context of the Abaqus internal user subroutine UEL.

B.1. UEL-implementation in Abaqus

Abaqus provides a programming-interface that allows the implementation of element-formulations via the UEL-subroutine, see the Abaqus User Subroutines Reference Manual [5, ch. 1.1.27] or the Abaqus Analysis User's Manual [2, ch. 31.15.1]. The UEL-interface makes it possible to include any element of almost arbitrary complexity such as higher-order elements for coupled problems. A general user element can be used conveniently with the Abaqus-internal solution procedures as, for instance, incremental-iterative Newton-Raphson schemes with adaptive incrementation or arc-length methods such as the modified Riks-algorithm, as discussed in Appendix D. Furthermore, user elements can also be applied in the context of contact problems, even though restricted to the definition of only slave surfaces in such an analysis. As a minor disadvantage, plotting and visualisation of results associated with the application of user elements are not directly supported by the Abaqus Viewer. However, these can be performed by using the subroutines UEXTERNALDB and URDFIL in connection with the Abaqus scripting interface to create binary or ASCII-based output files which, in turn, can be read by the Abaqus Viewer or any other FE-postprocessing software; for details we refer to Appendix B.3. In the following, we outline particular implementation-issues with regard to the Abaqus user subroutine UEL.

The current estimates of the basic solution variables—placements $\boldsymbol{\varphi}$ and non-local damage variable ϕ—at the element-nodes enter the UEL subroutine at the beginning of the iteration and are stored in the vector $\mathtt{U} := \boldsymbol{d}_e$ which is arranged according to

$$\boldsymbol{d}_e := \begin{bmatrix} \boldsymbol{u}_1 & \phi_1 & \dots & \boldsymbol{u}_{n_{\mathrm{en}}^{\varphi}} & \phi_{n_{\mathrm{en}}^{\phi}} \end{bmatrix}^{\mathrm{t}}, \tag{B.1}$$

with the nodal displacements $\mathbf{u}_I = \boldsymbol{\varphi}_I - \boldsymbol{X}_I$. Furthermore, the referential coordinates $\boldsymbol{X}_e$ are stored in the array $\mathtt{COORDS} := \boldsymbol{X}_e$ and arranged according to

$$\boldsymbol{X}_e = \begin{bmatrix} X_1 & \dots & X_{n_{\mathrm{en}}^{\varphi}} \\ Y_1 & \dots & Y_{n_{\mathrm{en}}^{\varphi}} \\ Z_1 & \dots & Z_{n_{\mathrm{en}}^{\varphi}} \end{bmatrix}. \tag{B.2}$$

The essential quantities to be specified within the UEL-subroutine are the element residual vector RHS, the element-based Jacobian or stiffness-matrix AMATRX, and the internal solution-dependent state variables SVARS. In summary,

$$\mathtt{RHS}(:,1) := \boldsymbol{r}_e, \tag{B.3}$$

$$\mathtt{AMATRX} := \boldsymbol{K}_e, \tag{B.4}$$

$$\mathtt{SVARS} := \mathcal{I}_e, \tag{B.5}$$

cf. the system of Eqs. (110). It is important to note that, when the classic Newton–Raphson-based solution scheme is used, RHS consists of NRHS = 1 column—in contrast to the arc-length method discussed in Appendix D.2 where NRHS = 2. Definition (B.3) requires that the external force loads $\boldsymbol{f}_{\mathrm{ext}\,e}$ must be passed into the UEL by means of distributed load definitions. Coding the subroutine UEL requires the distribution of the loads into consistent equivalent nodal forces and accounting for them in the calculation of the RHS array.

B.2. UEL-interface in Abaqus

With regard to the input-file, which basically defines an analysis in Abaqus, a general user-element is introduced by the keyword *USER ELEMENT, see the Abaqus Keywords Reference Manual [3], and is fully defined by the sequence.

```
* USER ELEMENT, TYPE = Un, NODES = 20, COORDINATES = 3, PROPERTIES = n, VARIABLES = n
  Data line(s) defining the active degrees of freedom as
  DOF1, DOF2, ...
  ENOD, DOF1, DOF2, ..., e.g.
  1, 2, 3, 11
  9, 1, 2, 3
* ELEMENT, TYPE = Un, ELSET = ⟨element-set-label⟩
  Data line(s) defining the connectivity list
* UEL PROPERTY, ELSET = ⟨element-set-label⟩
  Data line(s) specifying material/algorithmic parameters
```

Two parameters, the TYPE and the NODES, are *required* for a general user-element. The TYPE-parameter defines the 'name' of the element and is set by the format U*n*, where $1 \leqslant n < 10000$ is an integer. In order to use this particular element type, TYPE = U*n* must be assigned to the *ELEMENT keyword. The NODES-parameter defines the number of nodes associated with an element of this type which for the present case result in NODES = 20, cf. Fig. 4.

Furthermore, several *optional* parameters can be set to define the general user-element. Here, we use the COORDINATES, the PROPERTIES, and the VARIABLES-parameter. Several other parameters exist, but can be omitted for the present problem. The COORDINATES-parameter defines the maximum number of coordinates needed in the user subroutine UEL at any node point of the element and is set to 3 representing the three-dimensional Cartesian frame x, y, z. The PROPERTIES-parameter specifies the number of material or algorithmic parameters, etc., needed in the user subroutine UEL. Finally, the VARIABLES-parameter defines the number of internal variables to be stored within the element and is typically set equal to the number of integration points multiplied by the number of internal variables per integration point.

Subsequently, two data lines define the *active degrees of freedom* (DOFs) associated with the element, cf. Fig. 4. According to the Abaqus Analysis User's Manual [2, ch. 31.15.1], the active DOFs are generally specified at each node of the element. If the DOFs are identical at all of the element-nodes, the list of DOFs is specified only once, DOF1 being the first DOF active at the node, DOF2 the second, etc. Each time the DOFs at a node change compared to the previous node, a new list of DOFs must be specified, ENOD representing the (local) element-node number, wherefrom the new list becomes valid. Thereby, different element-nodes can have different DOFs which is especially beneficial when dealing with coupled field problems as in the present context. The order of DOFs to be maintained for a user element are defined according to the conventions in the Abaqus Analysis User's Manual [2, ch. 1.2.2] and are particularly important for convergence controls in non-linear analyses.

For the applications considered in this paper, nodes 1–8 exhibit displacement and non-local damage DOFs. This is defined by the first data line where 1, 2, 3 represent the displacements in x-, y- and z-direction, and where 11 represents the non-local damage variable ϕ taking the interpretation of a (scalar) temperature-like quantity. The second data line states that, from node 9 on, only displacement DOFs 1, 2 and 3 are active. This results in an arrangement of the element variables in so far as all of the DOFs at the first node appear first, followed by the DOFs at the second node, etc., see also Eq. (B.1).

Finally, the values of material or algorithmic parameters associated with the user element are specified by the *UEL PROPERTY option. These property values are assigned on an element set basis (ELSET) which conveniently enables the use of the same UEL subroutine for user elements with different properties.

B.3. Postprocessing for the UEL-subroutine in Abaqus

As mentioned above, plotting and visualisation of results associated with the application of user elements is not directly supported by the Abaqus Viewer. However, this can be resolved using particular Fortran and C++ subroutines in connection with the Abaqus scripting interface in order to create appropriate binary output files which, in turn, can be read by the Abaqus Viewer. In the following, we briefly outline an Abaqus-internal procedure to create an appropriate output-file which can be read by the Abaqus Viewer.

Applying a general user element in Abaqus, results may be stored in the binary .fil-file via, for instance, the input sequence.

```
* NODE FILE, NSET = ⟨node-set-label ⟩
  U, NT, COORD, CF, RF
```

Table B.7
Flowchart of the postprocessing stage when using a user defined element in Abaqus.

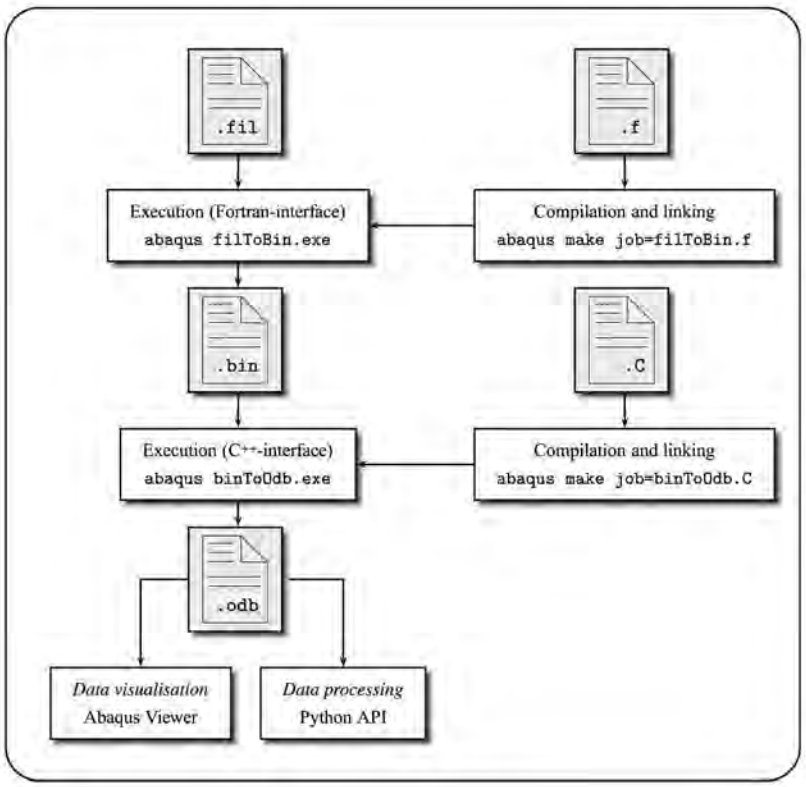

which defines a request for nodal output data for a prescribed node-set. The second line specifies the identifying 'keys' or rather 'output variable identifiers' for the variables to be written to the results file. For this case, we store the displacements `U`, temperature-like quantities `NT`—in the present context represented by the non-local damage variable ϕ—referential nodal coordinates `COORD`, concentrated forces `CF` and reaction forces `RF`. The second input sequence

```
*EL FILE, ELSET = ⟨element-set-label⟩, POSITION = INTEGRATION POINTS
SDV
```

defines a request for element output data at the integration points. For a user defined element, the integration point data can only be stored in the identifier for the solution-dependent state variables `SDV`, making it necessary to prescribe an explicit request for this key.

The Abaqus documentation makes no reference to the binary structure of the `.fil`-file containing the results which, consequently, must be read by means of an Abaqus Fortran-interface by using the subroutines INITPF, DBRNU and DBFILE. To the authors' knowledge, however, there is no Fortran-interface available allowing for the creation of an output database `.odb`-file. Therefore, reading from the `.fil`-file and writing to an `.odb`-file cannot be performed simultaneously. Alternatively, the information can be read from the `.fil`-file and stored in a binary `.bin`-file. The structure of this auxiliary `.bin`-file is defined by the user. Note, that the particular choice of a binary format is by no means mandatory, but turns out to be far more efficient than an ASCII-based format, especially when dealing with large FE-models. Afterwards, the C++-interface can be used to read the information from the `.bin`-file and to create a new `.odb`-file. According to this procedure, it will be possible to visualise the data contained in the final `.odb`-file by means of the Abaqus Viewer and/or to use the Python API to read the output data and analyse the obtained results. A flow-chart of the complete procedure is depicted in Table B.7. For details on the use of the subroutines INITPF, DBRNU and DBFILE and the use of the C++-interface, we refer the reader to the Abaqus 6.11 Documentation [1].

A typical Fortran-interface used to read the results from the `.fil`-file may not contain a `program`-statement. Instead, the main body of the subroutine is contained within the `ABQmain` subroutine. This subroutine has no input argument and no return values. Similarly, a typical C++-interface used to create a new `.odb`-file may not contain a `main`-function. Instead, the main body of the subroutine is contained within the `ABQmain`-function, where the function's name is case sensitive. It should be noted that, unlike the Fortran-interface, the C++-subroutine allows the use of input arguments for the `main`-function by means of the `argv`-pointer.

Compiling, linking and executing a postprocessing subroutine is a two-step procedure. Let the Fortran-subroutine be referred to as `fromFilToBin.f` and let the C++-subroutine be denoted as `fromBinToOdb.C`. In the first step, compilation and linking of the aforementioned subroutines is achieved using the `abaqus make` procedure. In the second step, the compilation and linking produces two executable files, i.e., `fromFilToBin.exe` and `fromBinToOdb.exe`. Once the executables have been generated, they may be called by means of the standard `abaqus` command. This procedure is illustrated in Table B.7.

Appendix C. Implementation of constitutive models using the Abaqus subroutine UMAT

The implementation of constitutive models into an incremental-iterative finite-element framework requires the computation of a stress tensor as well as the corresponding consistent tangent moduli. In the context of the commercial finite-element-software Abaqus, these can be included in the so-called user subroutine UMAT. The particular choice of stress tensor and tangent moduli is prescribed by Abaqus.

C.1. Consistent tangent moduli based on Jaumann stress rates

Starting from the Kirchhoff stress $\boldsymbol{\tau} = \boldsymbol{P} \cdot \boldsymbol{F}^{t} = \boldsymbol{F} \cdot \boldsymbol{S} \cdot \boldsymbol{F}^{t}$, the related spatial rate-constitutive equations in form of the *Lie derivative of the Kirchhoff stress* read

$$\mathcal{L}_v \boldsymbol{\tau} = \boldsymbol{F} \cdot \dot{\boldsymbol{S}} \cdot \boldsymbol{F}^{t} = \boldsymbol{e}^{\tau} : \boldsymbol{d}. \tag{C.1}$$

where $\boldsymbol{e}^{\tau}$ is the spatial elasticity tensor and $\boldsymbol{d} = \frac{1}{2}[\boldsymbol{l} + \boldsymbol{l}^{t}] = \boldsymbol{d}^{t}$ is the symmetric part of the velocity gradient $\boldsymbol{l} = \dot{\boldsymbol{F}} \cdot \boldsymbol{F}^{-1}$ which is commonly denoted as the *rate of deformation tensor*. Eq. (C.1) can be formulated in terms of the Jaumann stress rate $\overset{\circ}{\boldsymbol{\tau}} = \dot{\boldsymbol{\tau}} - \boldsymbol{w} \cdot \boldsymbol{\tau} - \boldsymbol{\tau} \cdot \boldsymbol{w}^{t}$, with the *spin tensor* $\boldsymbol{w} = \frac{1}{2}[\boldsymbol{l} - \boldsymbol{l}^{t}] = -\boldsymbol{w}^{t}$, which results in

$$\begin{aligned} \mathcal{L}_v \boldsymbol{\tau} &= \dot{\boldsymbol{\tau}} - \boldsymbol{l} \cdot \boldsymbol{\tau} - \boldsymbol{\tau} \cdot \boldsymbol{l}^{t} \\ &= \dot{\boldsymbol{\tau}} - [\boldsymbol{d} + \boldsymbol{w}] \cdot \boldsymbol{\tau} - \boldsymbol{\tau} \cdot [\boldsymbol{d} + \boldsymbol{w}]^{t} \\ &= \dot{\boldsymbol{\tau}} - \boldsymbol{w} \cdot \boldsymbol{\tau} + \boldsymbol{\tau} \cdot \boldsymbol{w} - \boldsymbol{d} \cdot \boldsymbol{\tau} - \boldsymbol{\tau} \cdot \boldsymbol{d} \\ &= \overset{\circ}{\boldsymbol{\tau}} - \boldsymbol{d} \cdot \boldsymbol{\tau} - \boldsymbol{\tau} \cdot \boldsymbol{d}, \end{aligned} \tag{C.2}$$

cf. Marsden and Hughes [57] or Miehe [65,66] amongst others. Relation (C.3) together with (C.1), results in

$$\overset{\circ}{\boldsymbol{\tau}} = \overset{\circ}{\boldsymbol{e}} : \boldsymbol{d} \quad \text{with } \overset{\circ}{\boldsymbol{e}} := \boldsymbol{e}^{\tau} + \boldsymbol{I} \,\overline{\otimes}\, \boldsymbol{\tau} + \boldsymbol{\tau} \,\overline{\otimes}\, \boldsymbol{I}. \tag{C.3}$$

The corresponding tangent moduli $\tilde{\boldsymbol{e}} = J^{-1}\, \overset{\circ}{\boldsymbol{e}}$ conjugate to the Cauchy stresses $\boldsymbol{\sigma} = J^{-1}\boldsymbol{\tau}$ read

$$\tilde{\boldsymbol{e}} := \boldsymbol{e} + \boldsymbol{I} \,\overline{\otimes}\, \boldsymbol{\sigma} + \boldsymbol{\sigma} \,\overline{\otimes}\, \boldsymbol{I}. \tag{C.4}$$

This fourth order tensor does generally not possess minor symmetry, i.e., $\tilde{\boldsymbol{e}}_{ijkl} \neq \tilde{\boldsymbol{e}}_{jikl} \neq \tilde{\boldsymbol{e}}_{ijlk}$, so that only its fully symmetric part

$$\tilde{\boldsymbol{e}}^{\text{sym}} := \boldsymbol{e} + \frac{1}{2}[\boldsymbol{I} \,\overline{\otimes}\, \boldsymbol{\sigma} + \boldsymbol{\sigma} \,\overline{\otimes}\, \boldsymbol{I} + \boldsymbol{I} \,\underline{\otimes}\, \boldsymbol{\sigma} + \boldsymbol{\sigma} \,\underline{\otimes}\, \boldsymbol{I}] \tag{C.5}$$

is taken into account, cf. Stein and Sagar [89].

C.2. UMAT-implementation in Abaqus

Abaqus provides a programming-interface that allows the implementation of general constitutive relations via the user subroutine UMAT, see the Abaqus User Subroutines Reference Manual [5, ch. 1.1.40] or the Abaqus Analysis User's Manual [2, ch. 25.7.1]. A user material can be used along with the robust and versatile Abaqus-internal solution procedures for (quasi-) static and dynamic analyses. Almost any element type can be chosen in connection with complex loading, contact and friction conditions. Furthermore, powerful plotting- and visualisation-capabilities of the results associated with the application of the user material are conveniently supported by Abaqus. In the following, we give an outline on particular implementation-issues with regard to the Abaqus user subroutine UMAT.

Three essential variables are required to be updated within the UMAT subroutine. In particular, the Cauchy stresses `STRESS` $:= \boldsymbol{\sigma}$, the internal variables `STATEV` $:= \mathcal{I}$, and the tangent moduli `DDSDDE` $:= \tilde{\boldsymbol{e}}$ enter the UMAT at the beginning of the increment and must be updated in this routine at the end of the increment. Due to the non-standard format of `DDSDDE` $:= \tilde{\boldsymbol{e}}$, which is not explicitly given in the Abaqus 6.11 Documentation [1], we briefly review some issues related to the `DDSDDE`-variable.

According to the Abaqus Theory Manual [4, ch. 1.5.3], the objective stress rates used in Abaqus/Standard in connection with solid continuum elements are based on the *Jaumann objective stress rate* for all built-in and user-defined materials. Accordingly, Stein and Sagar [89] report that *tangent moduli related to the Jaumann rate of Kirchhoff stress* are required to obtain quadratic convergence in the underlying Newton–Raphson-scheme. In this regard, we refer to the Abaqus User Subroutines Reference Manual [5, ch. 1.1.40] and the Abaqus Theory Manual [4, ch. 1.5.3] where the format of the required consistent tangent moduli $\texttt{DDSDDE} := \tilde{\boldsymbol{e}}$ is specified for *total-form constitutive relations* through the Jaumann stress rate $\overset{\circ}{\boldsymbol{\tau}} = \dot{\boldsymbol{\tau}} - \boldsymbol{w} \cdot \boldsymbol{\tau} - \boldsymbol{\tau} \cdot \boldsymbol{w}^{\mathrm{t}}$.

The tangent moduli as given in Eqs. (C.5) and (C.6), respectively, essentially reflect the consistent format required for DDSDDE, i.e., $\texttt{DDSDDE} := \tilde{\boldsymbol{e}}$. Practically, the non-symmetric format (C.5) can be used, since—unless the unsymmetric equation solution capability for the user-defined material is invoked—Abaqus automatically uses only the symmetric part of DDSDDE.

C.3. UMAT-interface in Abaqus

With regard to the input-file, a user-material is introduced by the keyword *USER MATERIAL, see the Abaqus Keywords Reference Manual [3]. The following input lines act as the interface to a UMAT:

```
* MATERIAL, NAME = ⟨name⟩
* USER MATERIAL, CONSTANTS=n_sdv
  Data line(s) specifying the material parameters
* DEPVAR
  n_sdv
* SOLID SECTION, ELSET = ALLELEM, MATERIAL = ⟨name⟩
* INITIAL CONDITIONS, TYPE = SOLUTION, USER
```

Here, the *MATERIAL keyword specifies the 'name' of the user material. This name is used to refer to the user-material in the element property options by means of the *SOLID SECTION keyword which assigns the user-material defined by the UMAT and its corresponding properties to a particular element set (ELSET) of solid continuum elements. As a crucial point, the *USER MATERIAL keyword is required to specify material constants for the UMAT. The *DEPVAR keyword is needed only for material models containing internal variables and is necessary for the allocation of space for n_{sdv} internal variables at each integration point. In this regard, the *INITIAL CONDITIONS, TYPE = SOLUTION, USER option is used to initialise non-zero internal variables via user subroutine SDVINI.

Appendix D. Arc-length methods

In this section, we briefly summarise some basics of arc-length-controlled solution procedures where we restrict ourselves to uncoupled purely mechanical problems. Moreover, we relate and specify the equations with regard to the arc-length algorithm implemented in Abaqus, emphasise issues of implementation in UEL-subroutines and comment on specific control parameters to be specified by the user.

For a general survey of arc-length methods, we refer to the monographs by Crisfield [23,24] and references cited therein.

D.1. Basic equations

According to general arc-length schemes, the loading parameter λ_{n+1} at time t_{n+1}, introduced to incrementally increase the load-magnitude, is allowed to vary during the iteration process. The particular value of the loading parameter is governed by a non-linear scalar constraint equation of the form $f(\boldsymbol{\varphi}_{n+1}, \lambda_{n+1}) = 0$ in terms of the current displacements $\boldsymbol{\varphi}_{n+1}$ and the current loading parameter λ_{n+1}. For the sake of clarity, we restrict the following description to uncoupled purely mechanical problems; the extension to coupled problems is straightforward. Consequently, the residual format of the non-linear balance of momentum enhanced by the constraint equation reads

$$\boldsymbol{r}^{\varphi}(\boldsymbol{\varphi}, \lambda) = \boldsymbol{f}^{\varphi}_{\mathrm{int}}(\boldsymbol{\varphi}) - \lambda \boldsymbol{f}^{\varphi}_{\mathrm{ext}} = \boldsymbol{0}, \tag{D.1}$$

$$f(\boldsymbol{\varphi}, \lambda) = 0, \tag{D.2}$$

where here and in the following, we often omit the subscript index $n+1$ associated with time t_{n+1} as well as the dependencies on $\boldsymbol{\varphi}$ and λ for the sake of readability. A Taylor series expansion around the solution at the current iteration step l—terms of quadratic and higher order being neglected—gives

$$\mathbf{r}^{\varphi}_{l+1} = \mathbf{r}^{\varphi}_{l} + \Delta\mathbf{r}^{\varphi} = \mathbf{0}, \tag{D.3}$$

$$f_{l+1} = f_l + \Delta f = 0, \tag{D.4}$$

with the increments of the residuals

$$\Delta\mathbf{r}^{\varphi} = \frac{\mathrm{d}\mathbf{r}^{\varphi}}{\mathrm{d}\boldsymbol{\varphi}} \cdot \Delta\boldsymbol{\varphi} + \frac{\mathrm{d}\mathbf{r}^{\varphi}}{\mathrm{d}\lambda}\Delta\lambda, \tag{D.5}$$

$$\Delta f = \frac{\mathrm{d}f}{\mathrm{d}\boldsymbol{\varphi}} \cdot \Delta\boldsymbol{\varphi} + \frac{\mathrm{d}f}{\mathrm{d}\lambda}\Delta\lambda. \tag{D.6}$$

Herein, the increments $\Delta\boldsymbol{\varphi} = \boldsymbol{\varphi}_{l+1} - \boldsymbol{\varphi}_l$ and $\Delta\lambda = \lambda_{l+1} - \lambda_l$ represent the difference between the values at iteration-step $l+1$ and l, while the derivatives are abbreviated by

$$\boldsymbol{K}^{\varphi\varphi} := \frac{\mathrm{d}\mathbf{r}^{\varphi}}{\mathrm{d}\boldsymbol{\varphi}}, \quad \mathbf{r}_{,\lambda} := \frac{\mathrm{d}\mathbf{r}^{\varphi}}{\mathrm{d}\lambda} = -\boldsymbol{f}^{\varphi}_{\mathrm{ext}}, \tag{D.7}$$

$$f_{,\boldsymbol{\varphi}} := \frac{\mathrm{d}f}{\mathrm{d}\boldsymbol{\varphi}}, \quad f_{,\lambda} := \frac{\mathrm{d}f}{\mathrm{d}\lambda}. \tag{D.8}$$

This results in the following linearised system of equations on element level

$$\begin{bmatrix} \boldsymbol{K}^{\varphi\varphi} & -\boldsymbol{f}^{\varphi}_{\mathrm{ext}} \\ f^{\mathrm{t}}_{,\boldsymbol{\varphi}} & f_{,\lambda} \end{bmatrix} \cdot \begin{bmatrix} \Delta\boldsymbol{\varphi} \\ \Delta\lambda \end{bmatrix} = \begin{bmatrix} \lambda\boldsymbol{f}^{\varphi}_{\mathrm{ext}} - \boldsymbol{f}^{\varphi}_{\mathrm{int}} \\ -f \end{bmatrix}, \tag{D.9}$$

which is neither symmetric nor banded. According to Batoz and Dhatt [15], the solution of this system of equations can be obtained by means of so-called block-solutions

$$\Delta\boldsymbol{\varphi}_r = \boldsymbol{K}^{\varphi\varphi\,-1} \cdot [\lambda\boldsymbol{f}^{\varphi}_{\mathrm{ext}} - \boldsymbol{f}^{\varphi}_{\mathrm{int}}], \tag{D.10}$$

$$\Delta\boldsymbol{\varphi}_{\lambda} = \boldsymbol{K}^{\varphi\varphi\,-1} \cdot \boldsymbol{f}^{\varphi}_{\mathrm{ext}}, \tag{D.11}$$

which enable us to give an explicit representation for the increment of the loading factor

$$\Delta\lambda = -\frac{f + f_{,\boldsymbol{\varphi}} \cdot \Delta\boldsymbol{\varphi}_r}{f_{,\boldsymbol{\varphi}} \cdot \Delta\boldsymbol{\varphi}_{\lambda} + f_{,\lambda}}. \tag{D.12}$$

Based on this, the increment in placement is calculated as

$$\Delta\boldsymbol{\varphi} = \Delta\boldsymbol{\varphi}_r + \Delta\lambda\,\Delta\boldsymbol{\varphi}_{\lambda} \tag{D.13}$$

and the updates of displacements and loading-parameter then read $\boldsymbol{\varphi}_{l+1} = \boldsymbol{\varphi}_l + \Delta\boldsymbol{\varphi}$ and $\lambda_{l+1} = \lambda_l + \Delta\lambda$. Note, that within the predictor step at t_0, constraint condition (D.4) is not determined. As a remedy, the loading parameter λ_n is increased by 1 providing the placement increment based on the last equilibrium state $\{\boldsymbol{\varphi}_n, \lambda_n\}$ reads as

$$\Delta\boldsymbol{\varphi}_{\lambda} = \boldsymbol{K}^{\varphi\varphi\,-1} \cdot \boldsymbol{f}^{\varphi}_{\mathrm{ext}} \tag{D.14}$$

and the distance to the last equilibrium point reads as

$$s_0 = \sqrt{\Delta\boldsymbol{\varphi}_{\lambda} \cdot \Delta\boldsymbol{\varphi}_{\lambda} + 1}. \tag{D.15}$$

Comparing the distance s_0 and the prescribed arc-length s, the increments of the loading parameter and the placement can be scaled by $\Delta\lambda = s/s_0$ and $\Delta\boldsymbol{\varphi} = [s/s_0]\,\Delta\boldsymbol{\varphi}_{\lambda}$. The updates of the displacements $\boldsymbol{\varphi}_{l+1}$ and the loading-parameter λ_{l+1} can then be calculated for $l = 0$.

What remains is the specification of the constraint equation (D.2). Different solution strategies are suggested in the literature as summarised, for instance, in the monographs by Wagner [96] and Reitinger [78] or in the textbooks by Crisfield [23,24]. One prominent example is the *iteration on the current normal plane* according to Ramm [76,77], which in Crisfield [23] is denoted as *Ramm's method*. Following this approach, which is illustrated in Fig. D.18(a), the equation

$$f = [\boldsymbol{\varphi}_l - \boldsymbol{\varphi}_n] \cdot [\boldsymbol{\varphi}_{l+1} - \boldsymbol{\varphi}_l] + [\lambda_l - \lambda_n][\lambda_{l+1} - \lambda_l] = 0 \tag{D.16}$$

constrains the solution to the normal plane with respect to the current iteration step. According to Eq. (D.12), the related increment can be specified as

$$\Delta\lambda = -\frac{[\boldsymbol{\varphi}_l - \boldsymbol{\varphi}_n] \cdot \boldsymbol{\varphi}_r}{[\boldsymbol{\varphi}_l - \boldsymbol{\varphi}_n] \cdot \boldsymbol{\varphi}_{\lambda} + \lambda_l - \lambda_n}. \tag{D.17}$$

Within this approach, the increment size is limited by moving a given distance along the tangent of the current solution point. Equilibrium is then sought in the plane that passes through the point thus obtained and that is normal to the same tangent. Moreover, the constraint (D.16) ensures that the iterative change is always normal to the secant change, which

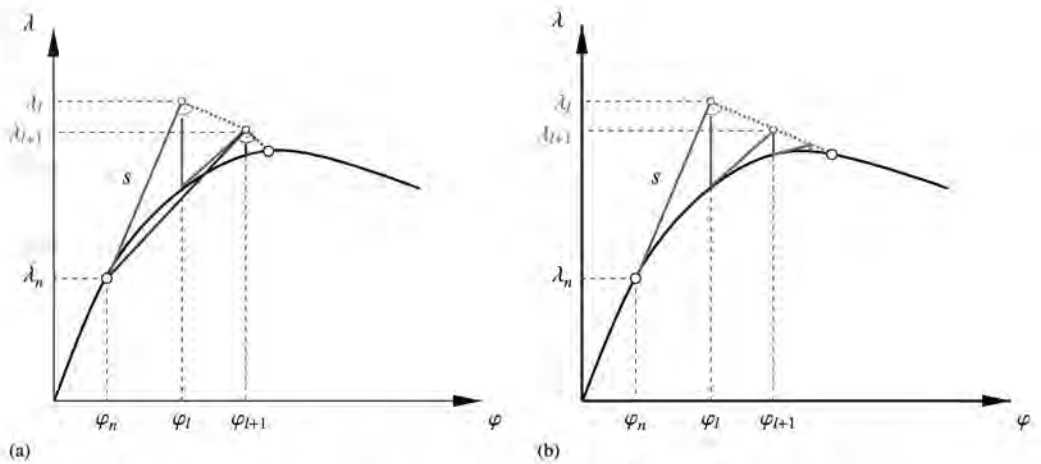

Fig. D.18. Illustration of arc-length methods according to Crisfield [23]. (a) Iteration on the current normal plane (Ramm's method), (b) Iteration on the initial normal plane (Riks-Wemper method). Quantities without subscript n are associated with t_{n+1}.

causes the equilibrium-search to be normal to the tangent of the previous iteration step, rather than to the tangent at the beginning of the increment. This method can be considered as an extension of the *iteration on the initial normal plane* according to the original work by Riks [79,80] and Wempner [100] which, following Crisfield [23], is accordingly denoted as *Riks-Wemper method*; see Fig. D.18(b) for an illustration.

D.2. Application within general user-elements via Abaqus subroutine UEL

Along with the UEL-subroutine, Abaqus is capable of using self-implemented element-formulations in combination with the Abaqus-internal arc-length procedure, referred to as the *modified Riks algorithm*, see the Abaqus Analysis User's Manual [2, ch. 6.2.4] for general usage aspects. According to the Abaqus Theory Manual [4, ch. 2.3.2], the *modified Riks algorithm* is a version of the aforementioned *iteration on the current normal plane* established by Ramm [76,77], see also [25] or [75].

In order to be able to use the Abaqus-internal modified Riks algorithm in combination with a UEL-subroutine, we have to meet the following requirements. As described above, the essential quantities to be specified within the UEL-subroutine are the element residual vector `RHS`, the element Jacobian- or stiffness-matrix `AMATRX`, and the internal-solution dependent state variables `SVARS`. Regarding `AMATRX` and `SVARS`, no modifications due to the Riks method have to be provided. However, in contrast to the purely Newton–Raphson-based solution scheme, `RHS` now consists of `NRHS = 2` columns. The first column `RHS(:,1)` is still associated with the residual vector. The additional second column `RHS(:,2)` contains the increments of external loads of the respective element, also referred to as the *incremental load vector*. In summary,

$$\texttt{AMATRX} := \boldsymbol{K}_e^{\varphi\varphi}, \tag{D.18}$$

$$\texttt{RHS}(:,1) := \lambda \boldsymbol{f}_{\text{ext}\,e}^{\varphi} - \boldsymbol{f}_{\text{int}\,e}^{\varphi}, \tag{D.19}$$

$$\texttt{RHS}(:,2) := \Delta\lambda \boldsymbol{f}_{\text{ext}\,e}^{\varphi}, \tag{D.20}$$

cf. the system of Eqs. (D.9). Here, definitions (D.18)–(D.20) require that all (external) force loads $\boldsymbol{f}_{\text{ext}}^{\varphi}$ must be passed into UEL by means of distributed load definitions so that the force loads are available for the definition of incremental load vectors; the load key `Un` must be used consistently, as discussed in the Abaqus Analysis User's Manual [2, ch. 31.15.1]. The coding in subroutine UEL must distribute the loads into consistent equivalent nodal forces and account for them in the calculation of the RHS array, see Appendix E for a consistent incorporation of surface traction forces in a finite-element-setting using Abaqus.

Furthermore, the UEL-subroutine provides the two variables `ADLMAG` and `DDLMAG`, where `ADLMAG` contains the total load magnitudes of the distributed loads at the end of the current increment and where `DDLMAG` represents the increments in the magnitudes of the distributed loads currently active on this element. With regard to relations (D.19) and (D.20), we consequently note that

$$\texttt{ADLMAG} := \lambda \quad \text{and} \quad \texttt{DDLMAG} := \Delta\lambda. \tag{D.21}$$

The input-file-setting is identical compared to a conventional modified Riks static analysis without any user-coding, i.e., introduced by `*STATIC, RIKS` followed by eight partially optional parameters which are summarised in Table D.8.

Table D.8
Control parameters to be used within the input-file accompanied by the keyword `*STATIC, RIKS` for the modified Riks method as implemented in Abaqus. The initial load proportionality factor (LPF) is computed as $\Delta\lambda_{\text{in}} = \Delta l_{\text{in}}/l_{\text{period}}$. Abaqus Analysis User's Manual [2, ch. 6.2.4] and Abaqus Keywords Reference Manual [3].

Symbol	Description
Δl_{in}	Initial arc-length increment
l_{period}	Total arc-length scale factor
Δl_{min}	Minimum arc-length increment
Δl_{max}	Maximum arc-length increment
λ_{end}	Maximum load proportionality factor (LPF) to end increment
nod_{mon}	Monitored node number
dof_{mon}	Monitored degree of freedom (DOF)
u_{end}	Maximum displacement at node and DOF to end increment

Appendix E. Deformation-dependent loads

The variational form of equilibrium includes the external virtual work (29) composed of contributions due to body forces $\bar{\boldsymbol{b}}$ and surface tractions $\bar{\boldsymbol{t}}$. This section addresses the incorporation of the latter, i.e., pressure-dependent surface traction forces which are clearly *deformation-dependent*. In this regard, we specify the related equilibrium expression and briefly outline the essential relations for a corresponding finite-element implementation. A detailed discussion on deformation, or rather configuration-dependent loads is provided in the early work of Sewell [85], while their algorithmic treatment and discretisation with regard to finite elements can be found in Schweizerhof and Ramm [84] which forms the basis for related treatises in finite-element textbooks, as, e.g., Bonet and Wood [19] and Wriggers [101] amongst others.

In the following, we restrict ourselves to the important case of *uniform normal pressure* which, for instance, is adopted for the numerical example of the arterial tube in Section 5.3.

E.1. Variational form

Let a uniform pressure p act on a surface a characterised by the normal $\boldsymbol{n}$. The traction force vector can then be specified as $\bar{\boldsymbol{t}} = p\boldsymbol{n}$ and the corresponding variational form is represented by

$$\delta_{\boldsymbol{\varphi}} \Pi_{\text{ext}}^{\text{sur}} = \int_{\partial \mathcal{B}_t} p\, \delta\boldsymbol{\varphi} \cdot \boldsymbol{n}\, \mathrm{d}a. \tag{E.1}$$

where the orientation of the normal $\boldsymbol{n}$ and the magnitude of the area element $\mathrm{d}a$ are both displacement-dependent. A convenient parameterisation of the normal and the area element in terms of the surface-coordinates ξ and η can be obtained by means of the tangent vectors $\boldsymbol{\varphi}_{,\xi} := \partial_\xi \boldsymbol{\varphi}$ and $\boldsymbol{\varphi}_{,\eta} := \partial_\eta \boldsymbol{\varphi}$ as

$$\boldsymbol{n} = \frac{\boldsymbol{\varphi}_{,\xi} \times \boldsymbol{\varphi}_{,\eta}}{\|\boldsymbol{\varphi}_{,\xi} \times \boldsymbol{\varphi}_{,\eta}\|} \quad \text{and} \quad \mathrm{d}a = \|\boldsymbol{\varphi}_{,\xi} \times \boldsymbol{\varphi}_{,\eta}\|\, \mathrm{d}\xi\, \mathrm{d}\eta, \tag{E.2}$$

enabling us to express the relation (E.1) as

$$\delta_{\boldsymbol{\varphi}} \Pi_{\text{ext}}^{\text{sur}} = \int_{\partial \mathcal{B}_t} p\, \delta\boldsymbol{\varphi} \cdot [\boldsymbol{\varphi}_{,\xi} \times \boldsymbol{\varphi}_{,\eta}]\, \mathrm{d}\xi\, \mathrm{d}\eta, \tag{E.3}$$

E.2. Discretisation

The finite element discretisation of (E.3) is performed using isoparametric shape functions N_I^{φ} together with their derivatives with respect to ξ resulting in

$$\boldsymbol{\varphi} \approx \boldsymbol{\varphi}^{\text{h}} = \sum_{I=1}^{n_{\text{sen}}^{\varphi}} N_I^{\varphi}(\xi)\, \boldsymbol{\varphi}_I, \quad \nabla_\xi \boldsymbol{\varphi} \approx \nabla_\xi \boldsymbol{\varphi}^{\text{h}} = \sum_{I=1}^{n_{\text{sen}}^{\varphi}} \nabla_\xi N_I^{\varphi}\, \boldsymbol{\varphi}_I, \tag{E.4}$$

where n_{sen}^{φ} is the number of nodes per surface-element. The placements $\boldsymbol{\varphi}$ are transformed to a quadrilateral reference element with surface-coordinates $\boldsymbol{\xi} := \{\xi, \eta\} \in \partial\bar{\mathcal{B}}$, where $\partial\bar{\mathcal{B}} := \{\boldsymbol{\xi} \in \mathbb{R}^2 \,|\, -1 \leqslant \chi \leqslant +1;\ \chi = \xi, \eta\}$ denotes the reference domain. According to (97), the element-specific variational form can be expressed by

$$\delta_{\boldsymbol{\varphi}} \Pi_{\text{ext}}^{\text{sur}\,e} = \sum_{I=1}^{n_{\text{sen}}^{\varphi}} \delta\boldsymbol{\varphi}_I \cdot \boldsymbol{f}_{\text{sur}\,I}^{\varphi} \quad \text{with} \quad \boldsymbol{f}_{\text{sur}\,I}^{\varphi} = \int_{\partial\bar{\mathcal{B}}} N_I^{\varphi}\, p\, \bar{\boldsymbol{n}}\, \mathrm{d}\xi\, \mathrm{d}\eta \tag{E.5}$$

where $\bar{\boldsymbol{n}}$ is specified by means of the vector-product in (E.3) as

$$\bar{\boldsymbol{n}} := \nabla_\xi \boldsymbol{\varphi}^{\mathrm{h}} \times \nabla_\eta \boldsymbol{\varphi}^{\mathrm{h}} = \begin{bmatrix} \varphi_{2,\xi}\,\varphi_{3,\eta} - \varphi_{3,\xi}\,\varphi_{2,\eta} \\ \varphi_{3,\xi}\,\varphi_{1,\eta} - \varphi_{1,\xi}\,\varphi_{3,\eta} \\ \varphi_{1,\xi}\,\varphi_{2,\eta} - \varphi_{2,\xi}\,\varphi_{1,\eta} \end{bmatrix}. \tag{E.6}$$

For the integration over surfaces in three-dimensional space and resulting properties of equivalent nodal forces for a 20-node hexahedral element, see Dhondt [26, ch. 2.3.4].

E.3. Linearisation

Linearisation is performed following the arguments in Section 4.2. The derivative $\mathrm{d}\boldsymbol{r}_I^{\varphi}/\mathrm{d}\boldsymbol{\varphi}_J$ exhibits an additional contribution due to the presence of the deformation-dependent term $\boldsymbol{f}_{\mathrm{sur}\,I}^{\varphi}$. This results in

$$\boldsymbol{K}_{IJ}^{\varphi\varphi} = \frac{\mathrm{d}\boldsymbol{r}_I^{\varphi}}{\mathrm{d}\boldsymbol{\varphi}_J} = \boldsymbol{K}_{IJ}^{\varphi\varphi\,\mathrm{mat}} + \boldsymbol{K}_{IJ}^{\varphi\varphi\,\mathrm{geo}} - \boldsymbol{K}_{IJ}^{\varphi\varphi\,\mathrm{def}}, \tag{E.7}$$

see Eq. (106). The external force contribution takes the representation

$$\boldsymbol{K}_{IJ}^{\varphi\varphi\,\mathrm{def}} := \int_{\partial\mathcal{B}} p\, N_I^{\varphi}\, [N_{J,\xi}^{\varphi}\, \boldsymbol{N}_{,\eta}^{\varphi} - N_{J,\eta}^{\varphi}\, \boldsymbol{N}_{,\xi}^{\varphi}]\, \mathrm{d}\xi\, \mathrm{d}\eta \tag{E.8}$$

in which a skew-symmetric matrix

$$\boldsymbol{N}_{,\alpha}^{\varphi} = \begin{bmatrix} 0 & \varphi_{3,\alpha} & -\varphi_{2,\alpha} \\ -\varphi_{3,\alpha} & 0 & \varphi_{1,\alpha} \\ \varphi_{2,\alpha} & -\varphi_{1,\alpha} & 0 \end{bmatrix}, \quad \alpha = \xi, \eta \tag{E.9}$$

is introduced, see, e.g., Wriggers [101]. It becomes apparent that the external force contribution $\boldsymbol{K}_{IJ}^{\varphi\varphi\,\mathrm{def}}$ and hence the global tangent stiffness matrix $\boldsymbol{K}$ may become non-symmetric for pressure loading. This means that, generally, no potential can be associated with an arbitrary pressure load. However, special boundary conditions provided, the total assembled stiffness matrix can be symmetric, and a potential consequently exists, see, for instance, Waffenschmidt and Menzel [95] where a double-layered thick-walled cylindrical tube subjected to internal pressure is analysed on the basis of a total potential.

The surface integrals in Eqs. (E.5) and (E.8) are typically evaluated numerically at discrete integration points by means of appropriate quadrature rules, see Zienkiewicz and Taylor [102], Hughes [41] and Bathe [14].

E.4. Implementation via Abaqus subroutine UEL

Along with the UEL-subroutine defining a general user-element, Abaqus is capable of applying *concentrated* point loads or moments without any additional considerations within the UEL-subroutine, see Abaqus Analysis User's Manual [2, ch. 32.4.2]. Furthermore, *distributed* and possibly deformation-dependent loads according to Appendix E.1 can also be defined for a general user-defined element. This, however, requires additional implementation efforts by means of the Abaqus user subroutine UEL.

Following the Abaqus Analysis User's Manual [2, ch. 31.15.1], general distributed loads—in connection with a general user-element—are invoked by the following input-sequence.

```
* DLOAD
⟨element-set-label⟩, Un, p
```

where the `*DLOAD` keyword is used to attribute the distributed loading to the element-set associated with the load. Furthermore, a load type key `Un` and a reference pressure-type load magnitude p must be prescribed. The form of the load type key reads `Un` for uniform loads, where $n :=$ `JDLTYP(1,1)` denotes an integer and characterises the particular element-face subjected to the load, see Table E.9.

For each active load of type `Un`, the subroutine UEL provides the current magnitude `ADLMAG` $:= \lambda_{n+1}$ and the current increment in magnitude `DDLMAG` $:= \Delta\lambda$ of the load, cf. also Eq. (D.21). The coding in subroutine UEL must distribute the loads into consistent equivalent nodal forces (E.5) and provide their contribution to the Jacobian matrix by means of the load stiffness matrix (E.8).

Due to the possibly non-symmetric global tangent stiffness matrix $\boldsymbol{K}$ in the case of deformation-dependent loading, a related step definition in Abaqus according to

```
* STEP, NLGEOM, INC = n, UNSYMM = YES
```

Table E.9
List of element-face-numbers and associated node-numbering corresponding to the hexahedral finite element depicted in Fig. 4.

Face no. n	Node no.							
1	1	2	3	4	9	10	11	12
2	5	8	7	6	16	15	14	13
3	1	5	6	2	17	13	18	9
4	2	6	7	3	18	14	19	10
5	3	7	8	4	19	15	20	11
6	4	8	5	1	20	16	17	12

should enable the unsymmetric matrix storage and solution by setting `UNSYMM = YES`. Note, that a non-symmetric equation solution may be four times as expensive as the corresponding symmetric system, see the Abaqus Analysis User's Manual [2, ch. 6.1.1] for details.

References

Abaqus 6.11 Documentation, Dassault Systèmes Simulia Corp., 2011
Abaqus Analysis User's Manual, Abaqus 6.11 Documentation. Dassault Systèmes Simulia Corp., 2011
Abaqus Keywords Reference Manual, Abaqus 6.11 Documentation. Dassault Systèmes Simulia Corp., 2011
Abaqus Theory Manual, Abaqus 6.11 Documentation. Dassault Systèmes Simulia Corp., 2011
Abaqus User Subroutines Reference Manual, Abaqus 6.11 Documentation. Dassault Systèmes Simulia Corp., 2011
R. Abu Al-Rub, G. Voyiadjis, A finite strain plastic-damage model for high velocity impact using combined viscosity and gradient localization limiters: Part I – theoretical formulation, International Journal of Damage Mechanics 15 (2006) 293–334.
E. Aifantis, On the role of gradients in the localization of deformation and fracture, International Journal of Engineering Science 30 (1992) 1279–1299.
E. Aifantis, On the gradient approach – Relation to Eringen's nonlocal theory, International Journal of Engineering Science 49 (2011) 1367–1377.
V. Alastrué, M. Martínez, M. Doblaré, A. Menzel, Anisotropic micro-sphere-based finite elasticity applied to blood vessel modelling, Journal of the Mechanics and Physics of Solids 57 (2009) 178–203.
V. Alastrué, E. Peña, M. Martínez, M. Doblaré, Assessing the use of the Opening Angle Method to enforce residual stresses in patient-specific arteries, Annals of Biomedical Engineering 35 (2007) 1821–1837.
V. Alastrué, J. Rodríguez, B. Calvo, M. Doblaré, Structural damage models for fibrous biological soft tissues, International Journal of Solids and Structures 44 (2007) 5894–5911.
A. Ask, R. Denzer, A. Menzel, M. Ristinmaa, Inverse-motion-based form finding for quasi-incompressible finite electroelasticity, International Journal for Numerical Methods in Engineering 94 (2013) 554–572.
D. Balzani, S. Brinkhues, G. Holzapfel, Constitutive framework for the modeling of damage in collagenous soft tissues with application to arterial walls, Computer Methods in Applied Mechanics and Engineering 213–216 (2012) 139–151.
K.J. Bathe, Finite Element Procedures, Prentice Hall, 1996.
J.L. Batoz, G. Dhatt, Incremental displacement algorithms for nonlinear problems, International Journal for Numerical Methods in Engineering 14 (1979) 1262–1267.
Z. Bažant, Why continuum damage is nonlocal: Micromechanics arguments, Journal of Engineering Mechanics 117 (1991) 1070–1087.
Z. Bažant, G. Di Luzio, Nonlocal microplane model with strain-softening yield limits, International Journal of Solids and Structures 41 (2004) 7209–7240.
Z. Bažant, J. Ožbolt, Nonlocal microplane model for fracture, damage, and size effect in structures, Journal of Engineering Mechanics 116 (1990) 2485–2505.
J. Bonet, R.D. Wood, Nonlinear Continuum Mechanics for Finite Element Analysis, Cambridge University Press, 2008.
R. de Borst, Computation of post-bifurcation and post-failure behavior of strain-softening solids, Computers & Structures 25 (1987) 211–224.
R. de Borst, J. Pamin, Some novel developments in finite element procedures for gradient-dependent plasticity, International Journal for Numerical Methods in Engineering 39 (1996) 2477–2505.
B. Calvo, E. Peña, M. Martínez, M. Doblaré, An uncoupled directional damage model for fibred biological soft tissues. Formulation and computational aspects, International Journal for Numerical Methods in Engineering 69 (2007) 2036–2057.
M. Crisfield, Non-Linear Finite Element Analysis of Solids and Structures, Vol. 1 – Essentials, Wiley, 1997
M. Crisfield, Non-Linear Finite Element Analysis of Solids and Structures, Volume 2 – Advanced Topics, Wiley, 1997.
M.A. Crisfield, A fast incremental/iteration solution procedure that handles 'snap-through', Computers and Structures 13 (1981) 55–62.
G. Dhondt, The Finite Element Method for Three-Dimensional Thermomechanical Applications, Wiley, 2004.
B. Dimitrijević, On a regularization framework for inelastic material models via gradient enhancement of the free energy function, Ph.D. thesis, Fakultät für Bauingenieurwesen, Ruhr-Universität Bochum, 2010.
B.J. Dimitrijević, K. Hackl, A method for gradient enhancement of continuum damage models, Technische Mechanik 28 (2008) 43–52.
B.J. Dimitrijević, K. Hackl, A regularization framework for damage-plasticity models via gradient enhancement of the free energy, International Journal for Numerical Methods in Biomedical Engineering 27 (2011) 1199–1210.
A. Eringen (Ed.), Continuum Physics, Volume IV – Polar and Nonlocal Field Theories, Academic Press, 1976.
A. Eringen, Nonlocal Continuum Field Theories, Springer, 2002.
S. Forest, Micromorphic approach for gradient elasticity, viscoplasticity, and damage, Journal of Engineering Mechanics 135 (2009) 117–131.
M. Frémond, B. Nedjar, Damage, gradient of damage and principle of virtual power, International Journal of Solids and Structures 33 (1996) 1083–1103.
T. Gasser, G. Holzapfel, Finite element modeling of balloon angioplasty by considering overstretch of remnant non-diseased tissues in lesions, Computational Mechanics 40 (2007) 47–60.
T. Gasser, R. Ogden, G. Holzapfel, Hyperelastic modelling of arterial layers with distributed collagen fibre orientations, Journal of the Royal Society Interface 3 (2006) 15–35.
M. Gurtin, E. Francis, Simple rate-independent model for damage, AIAA Journal of Spacecraft 18 (1981) 285–288.
G. Holzapfel, T. Gasser, R. Ogden, A new constitutive framework for arterial wall mechanics and a comparative study of material models, Journal of Elasticity 61 (2000) 1–48.
G. Holzapfel, R. Ogden (Eds.), Biomechanics of Soft Tissue in Cardiovascular Systems. Number 441 in, CISM Courses and Lectures, Springer, 2003.
G. Holzapfel, R. Ogden, Constitutive modelling of arteries. Proceedings of the Royal Society A, Mathematical, Physical and Engineering Sciences 466 (2010) 1551–1597.

G. Holzapfel, M. Stadler, C. Schulze-Bauer, A layer-specific three-dimensional model for the simulation of balloon angioplasty using magnetic resonance imaging and mechanical testing, Annals of Biomedical Engineering 30 (2002) 753–767.
T. Hughes, The Finite Element Method, Dover, 2000.
M. Jirásek, Nonlocal models for damage and fracture: Comparison of approaches, International Journal of Solids and Structures 35 (1998) 4133–4145.
L. Kachanov, Time of the rupture process under creep conditions, in: Izvestija Akademii Nauk Sojuza Sovetskich Socialisticeskich Respubliki (SSSR) Otdelenie Techniceskich Nauk (Moskra), vol. 8, 1958, pp. 26–31.
L. Kachanov, Introduction to Continuum Damage Mechanics, Martinus Nijhoff Publishers, Dordrecht, The Netherlands, 1986.
D. Krajcinovic, Damage Mechanics, North-Holland, Amsterdam, 1996.
D. Krajcinovic, J. Lemaitre, Continuum Damage Mechanics, Number 295 in, CISM Courses and Lectures, Springer, 1987.
E. Kuhl, E. Ramm, Simulation of strain localization with gradient enhanced damage models, Computational Materials Science 16 (1999) 176–185.
E. Kuhl, E. Ramm, R. de Borst, An anisotropic gradient damage model for quasi-brittle materials, Computer Methods in Applied Mechanics and Engineering 183 (2000) 87–103.
D. Lasry, T. Belytschko, Localization limiters in transient problems, International Journal of Solids and Structures 24 (1988) 581–597.
J. Lemaitre, A Course on Damage Mechanics, second ed., Springer.
J. Lemaitre, J.L. Chaboche, Mechanics of Solid Materials, Cambridge University Press, Cambridge, 1990.
M. Leukart, E. Ramm, A comparison of damage models formulated on different material scales, Computational Materials Science 28 (2003) 749–762.
T. Liebe, A. Menzel, P. Steinmann, Theory and numerics of a thermodynamically consistent framework for geometrically non-linear gradient plasticity, International Journal of Engineering Science 41 (2003) 1603–1629.
T. Liebe, P. Steinmann, Two strategies towards geometrically non-linear isotropic gradient damage, Journal of the Mechanical Behavior of Materials 13 (2002) 175–194.
T. Liebe, P. Steinmann, A. Benallal, Theoretical and computational aspects of a thermodynamically constistent framework for geometrically linear gradient damage, Computer Methods in Applied Mechanics and Engineering 190 (2001) 6555–6576.
R. Mahnken, E. Kuhl, Parameter identification of gradient enhanced damage models with the finite element method, European Journal of Mechanics – A/Solids 18 (1999) 819–835.
J. Marsden, T. Hughes, Mathematical Foundations of Elasticity, Dover, 1994.
P. Martins, E. Peña, R.N. Jorge, A. Santos, L. Santos, T. Mascarenhas, B. Calvo, Mechanical characterization and constitutive modelling of the damage process in rectus sheath, Journal of the Mechanical Behavior of Biomedical Materials 8 (2012) 111–122.
A. Menzel, M. Ekh, P. Steinmann, K. Runesson, Anisotropic damage coupled to plasticity: modelling based on the effective configuration concept, International Journal for Numerical Methods in Engineering 54 (2002) 1409–1430.
A. Menzel, M. Harrysson, M. Ristinmaa, Towards an orientation-distribution-based multi-scale approach for remodelling biological tissues, Computer Methods in Biomechanics and Biomedical Engineering 11 (2008) 505–524.
A. Menzel, P. Steinmann, A theoretical and computational framework for anisotropic continuum damage mechanics at large strains, International Journal of Solids and Structures 38 (2001) 9505–9523.
A. Menzel, P. Steinmann, A view on anisotropic finite hyper-elasticity, European Journal of Mechanics A/Solids 22 (2003) 71–87.
A. Menzel, P. Steinmann, On the spatial formulation of anisotropic multiplicative elasto-plasticity, Computer Methods in Applied Mechanics and Engineering 192 (2003) 3431–3470.
H.B. Mühlhaus, E. Aifantis, A variational principle for gradient plasticity, International Journal of Solids and Structures 28 (1991) 845–857.
C. Miehe, Aspects of the formulation and finite element implementation of large strain isotropic elasticity, International Journal for Numerical Methods in Engineering 37 (1994) 1981–2004.
C. Miehe, Discontinuous and continuous damage evolution in Ogden-type large-strain elastic materials, European Journal of Mechanics A/Solids 14 (1995) 697–720.
C. Miehe, A multi-field incremental variational framework for gradient-extended standard dissipative solids, Journal of the Mechanics and Physics of Solids 59 (2011) 898–923.
B. Nedjar, A theoretical and computational setting for a geometrically nonlinear gradient damage modelling framework, Computational Mechanics 30 (2002) 65–80.
J. Pamin, Gradient plasticity and damage models: a short comparison, Computational Materials Science 32 (2005) 472–479.
R.H.J. Peerlings, R. de Borst, W.A.M. Brekelmans, M.G.D. Geers, Gradient-enhanced damage modelling of concrete fracture, Mechanics of Cohesive-frictional Materials 3 (1998) 323–342.
R.H.J. Peerlings, R. de Borst, W.A.M. Brekelmans, J.H.P. de Vree, Gradient enhanced damage for quasi-brittle materials, International Journal for Numerical Methods in Engineering 39 (1996) 3391–3403.
E. Peña, V. Alastrué, A. Laborda, M. Martínez, M. Doblaré, A constitutive formulation of vascular tissue mechanics including viscoelasticity and softening behaviour, Journal of Biomechanics 43 (2010) 984–989.
G. Pijaudier-Cabot, Z. Bažant, Nonlocal damage theory, Journal of Engineering Mechanics 113 (1987) 1512–1533.
C. Polizzotto, G. Borino, P. Fuschi, A thermodynamically consistent formulation of nonlocal and gradient plasticity, Mechanics Research Communications 25 (1998) 75–82.
G. Powell, J. Simons, Improved iterative strategy for nonlinear structures, International Journal for Numerical Methods in Engineering 17 (1981) 1455–1467.
E. Ramm, Strategies for tracing the nonlinear response near limit points, in: W. Wunderlich, E. Stein, K.J. Bathe (Eds.), Nonlinear Finite Element Analysis in Structural Mechanics, Springer, Berlin Heidelberg, 1981, pp. 63–89.
E. Ramm, The Riks/Wempner approach – an extension of the displacement control method in non-linear analysis, in: E. Hinton (Ed.), Non-Linear Computational Mechanics, Pineridge, Swansea, 1982, pp. 63–86.
R. Reitinger, StabilitSt und Optimierung imperfektionsempfindlicher Tragwerke. Ph.D. thesis. Universität Stuttgart, Institut für Baustatik, Bericht-Nr. 17, 1994.
E. Riks, The application of Newton's method to the problem of elastic stability, Transactions of the ASME Journal of Applied Mechanics 39 (1972) 1060–1066.
E. Riks, An incremental approach to the solution of snapping and buckling problems, International Journal of Solids and Structures 15 (1979) 529–551.
D. Rogula (Ed.), Nonlocal Theory of Material Media. Number 268 in, CISM Courses and Lectures, Springer, 1982.
P. Sáez, V. Alastrué, E. Peña, M. Doblaré, M. Martínez, Anisotropic microsphere-based approach to damage in soft fibered tissue, Biomechanics and Modeling in Mechanobiology 11 (2011) 595–608.
A. Schriefl, G. Zeindlinger, D. Pierce, P. Regitnig, G. Holzapfel, Determination of the layer-specific distributed collagen fibre orientations in human thoracic and abdominal aortas and common iliac arteries, Journal of the Royal Society Interface 9 (2012) 1275–1286.
K. Schweizerhof, E. Ramm, Displacement dependent pressure loads in nonlinear finite element analyses, Computers and Structures 18 (1984) 1099–1114.
M. Sewell, On configuration-dependent loading, Archive for Rational Mechanics and Analysis 23 (1967) 327–351.
J. Simo, On a fully three-dimensional finite-strain viscoelastic damage model: Formulation and computational aspects, Computer Methods in Applied Mechanics and Engineering 60 (1987) 153–173.
J. Simo, T. Hughes, Computational Inelasticity, in: Interdisciplinary Applied Mathematics, vol. 7, Springer, 1998.
A. Simone, H. Askes, R. Peerlings, L. Sluys, Interpolation requirements for implicit gradient-enhanced continuum damage models, Communications in Numerical Methods in Engineering 19 (2003) 563–572.

E. Stein, G. Sagar, Convergence behavior of 3D finite elements for Neo-Hookean material, Engineering Computations 25 (2008) 220–232.
P. Steinmann, Formulation and computation of geometrically non-linear gradient damage, International Journal for Numerical Methods in Engineering 46 (1999) 757–779.
T. Svedberg, K. Runesson, A thermodynamically consistent theory of gradient-regularized plasticity coupled to damage, International Journal of Plasticity 13 (1997) 669–696.
K. Volokh, Hyperelasticity with softening for modeling materials failure, Journal of the Mechanics and Physics of Solids 55 (2007) 2237–2264.
G. Voyiadjis, R. Abu Al-Rub, A finite strain plastic-damage model for high velocity impact using combined viscosity and gradient localization limiters: Part II – Numerical Aspects and Simulations, International Journal of Damage Mechanics 15 (2006) 335–373.
J. de Vree, W. Brekelmans, M. van Gils, Comparison of nonlocal approaches in continuum damage mechanics, Computers & Structures 55 (1995) 581–588.
T. Waffenschmidt, A. Menzel, Extremal states of energy of a double-layered thick-walled tube – application to residually stressed arteries, Journal of the Mechanical Behavior of Biomedical Materials (2013), http://dx.doi.org/10.1016/j.jmbbm.2013.05.023. available online.
W. Wagner, Zur Behandlung von Stabilitätsproblemen der Elastostatik mit der Methode der Finiten Elemente. Forschungs- und Seminarberichte aus dem Bereich der Mechanik der Universität Hannover. Bericht-Nr. F 91/1, 1991.
B. Wcisło, J. Pamin, K. Kowalczyk-Gajewska, Gradient-enhanced damage model for large deformations of elastic-plastic materials, Archives of Mechanics 65 (2013) 407–428.
E.W. Weisstein, Erfi. From MathWorld – A Wolfram Web Resource, 2013. <http://mathworld.wolfram.com/Erfi.html>.
F. Welschinger, A Variational Framework for Gradient-Extended Dissipative Continua. Application to Damage Mechanics, Fracture, and Plasticity. Ph.D. thesis. Universität Stuttgart, Institut für Mechanik (Bauwesen), Lehrstuhl I, Bericht Nr. I-24, 2011.
G. Wempner, Discrete approximations related to nonlinear theories of solids, International Journal of Solids and Structures 7 (1971) 1581–1599.
P. Wriggers, Nonlinear Finite Element Methods, Springer, 2008.
O. Zienkiewicz, R. Taylor, The Finite Element Method for Solid and Structural Mechanics, Elsevier, 2000.